

COMPARISON OF THE EFFECTS OF REALISTIC FLUX SURFACE
MODELS ON CALCULATIONS OF PLASMA ASYMMETRIES IN DIII-D

A Thesis
Presented to
The Academic Faculty

by

Timothy Gerard Collart

In Partial Fulfillment
of the Requirements for the Degree
Masters of Science in the
Nuclear and Radiological Engineering Program
School of Mechanical Engineering

Georgia Institute of Technology

December 2015

Copyright © Timothy Collart 2015

COMPARISON OF THE EFFECTS OF REALISTIC FLUX SURFACE
MODELS ON CALCULATIONS OF PLASMA ASYMMETRIES IN DIII-D

Approved by:

Dr. Weston Stacey – Advisor
Nuclear and Radiological Engineering Program
School of Mechanical Engineering
Georgia Institute of Technology

Dr. Bojan Petrovic
Nuclear and Radiological Engineering Program
School of Mechanical Engineering
Georgia Institute of Technology

Dr. Dingkaung Zhang
Nuclear and Radiological Engineering Program
School of Mechanical Engineering
Georgia Institute of Technology

Date Approved: 19 August 2015

ACKNOWLEDGEMENTS

I wish to thank my wife for her support throughout this process, and Dr. Stacey for his extensive guidance throughout my time at Georgia Tech. Special thanks to Dr. Grierson for supplying the velocity measurements used in this analysis, and for helping me to navigate the DIII-D computer systems. Finally, thanks to Theresa Wilks and Max Hill for the countless helpful discussions, which have aided me in developing the theory and codes necessary to complete this task.

Ad majorem Dei gloriam

TABLE OF CONTENTS

	Page
ACKNOWLEDGEMENTS	iii
LIST OF TABLES	vii
LIST OF FIGURES	viii
LIST OF SYMBOLS	xii
LIST OF ABBREVIATIONS	xvi
SUMMARY	xvii
<u>CHAPTER</u>	
1. INTRODUCTION	1
2. BASIC PLASMA THEORY	3
2.1. Continuity and Momentum Balance	3
2.2. Collision Frequencies	5
2.3. Viscosity Formalism	6
2.4. Electromagnetic, Friction, and External Source Effects	8
3. DEFINITION AND ORTHOGONALIZATION OF A GENERAL CURVILINEAR COORDINATE SYSTEM	10
3.1. Defining Flux Surfaces Using the Plasma Flux Function (ψ).	10
3.2. Representation of Magnetic Fields in Semi-Cartesian and Curvilinear Coordinate Systems	13
3.3. General Flux-surface Aligned (<i>GFA</i>) Curvilinear Coordinate System	18
3.4. Orthogonalized Flux-surface Aligned (<i>OFA</i>) coordinate system	23
3.5. Calculation of parameters dependent on magnetic field configuration	26
4. ANALYTIC MODELS FOR REPRESENTING FLUX-SURFACES	29
4.1. Curvilinear Spline (CS) fitting method for comparison of flux-surface fitting models	29
Using Spline fits to relate EFIT flux surfaces and OFA basis vectors to curvilinear variables ρ and θ	30

Curvilinear poloidal magnetic field error	31
General flux-surface fitting techniques	34
4.2. Circular Model for General and Orthogonalized Flux-surface Aligned Coordinates (C-GFA and C-OFA)	35
4.3. Single Fourier Expansion model (SF) for minor radius (r)	42
4.4. Double Fourier Expansion model (DF) for R and Z	48
4.5. Symmetric and Asymmetric Miller models (SM and AM)	51
4.6. Summary of analytic curvilinear coordinate models	60
5. FORMULATING CONTINUITY AND MOMENTUM BALANCE EQUATIONS IN CURVILINEAR COORDINATE SYSTEM	64
5.1. Equations formulated for curvilinear coordinates	64
5.2. Relating unknown poloidal variations in plasma properties to asymmetries in density, velocity, and electric potential.	67
5.3. Determining radially dependent plasma properties from experimental measurements	69
6. CALCULATION METHODOLOGY AND RESULTS	72
6.2. Mathematica automated-derivation of a system of fourteen plasma asymmetry equations	74
6.3. Fortran 90 solution code to calculate plasma asymmetries	76
6.4. Results, and analysis of the effects of modifications to the geometry model	78
7. CONCLUSIONS	87

Appendix A	Inertial Terms and elements of the Viscosity Tensor	89
A.1	Expansion of Continuity Streaming Term in OFA Geometry	89
A.2	Expansion of Momentum and Torque Inertial Terms in OFA Geometry	89
A.3	Elements of the Viscosity Tensor in OFA Geometry	89
A.4	Expansion of Momentum and Torque Viscous Terms in OFA Geometry	91
Appendix B	Simplification of the Pfirsch-Schluter Viscosity Interpolation Function for low collisionality plasma	93
Appendix C	Figures	95
C.1	Curvilinear Model Basis Vector Orientations	95
C.2	Effects of Asymmetries on Radial Velocities and Electric Potential Calculations	96
C.3	Calculations of 2D distributions of plasma properties, using the Orthogonalized Asymmetric Miller geometry model	96
References		99

LIST OF TABLES

	Page
Table 1: Curvilinear Spline (CS) model field errors [Eq. (4.2)] (%) in three inner plasma sectors (left columns), and averaged over the full inner and edge plasma regions [Figure 12]	34
Table 2: FC dimensions and positional errors. $\nabla_{EFFI} = 15.962$.	38
Table 3: Circular model field errors [Eq. (4.2)] (%) in three inner plasma sectors (left columns), and averaged over the full inner and edge plasma regions [Figure 12].	41
Table 4: Positional Errors (%) and number of fitting coefficients per. flux surface of three expansion orders of the Single Fourier (SF) model.	44
Table 5: Comparison of Single Fourier Magnetic field errors [Eq. (4.2)] (%) in three inner plasma sectors (left columns), and averaged over the full inner and edge plasma regions [Figure 12].	47
Table 6: Averaged flux-surface positional error (%) number of expansion coefficients per. flux surface for two Double Fourier (DF) models.	49
Table 7: Comparison of Double Fourier Magnetic field errors [Eq. (4.2)] (%) in three inner plasma sectors (left columns), and averaged over the full inner and edge plasma regions [Figure 12].	51
Table 8: Positional Errors (%) and number of fitting coefficients per. flux surface for the Symmetric Miller (SM) and the Asymmetric Miller (AM) models.	55
Table 9: Comparison of Miller poloidal magnetic field errors [Eq. (4.2)] (%) in three inner plasma sectors (left columns), and averaged over the full inner and edge plasma regions [Figure 12].	59
Table 10: Comparison of sector dependent field errors, number of fitting coefficients per flux surface, and both inner and outer performance parameters for the most effective geometry models of each class considered in this analysis.	62
Table 11: Comparison of Monte-Carlo calculated plasma volumes with volumes obtained by integrating differential volume elements over the full variable phase space.	80
Table 12: Elements of the Viscosity Tensor, with $f_p = \left \frac{B_\theta}{B} \right $, $f_t = \left \frac{B_\phi}{B} \right \approx 1$, $\eta_2 = 4\eta_1$, and $\eta_4 = 2\eta_3$.	91

LIST OF FIGURES

	Page
Figure 1: Interspecies and self-collision frequencies for DIII-D Shot # 149468, 1905ms.	6
Figure 2: Locations of the S_θ and S_ϕ surfaces used to define poloidal and toroidal magnetic flux.	11
Figure 3: Sample flux surfaces of $\psi = \text{const.}$ for DIII-D Shot# 149468, 1905ms. The coordinates (R, Z) can be transformed to curvilinear coordinates (ρ, θ) related to position on flux-surfaces.	12
Figure 4: Three sets of normalized basis vectors. Cartesian $(\hat{e}_x, \hat{e}_y, \hat{e}_z)$ [left], semi-Cartesian $(\hat{e}_R, \hat{e}_Z, \hat{e}_\phi)$ [center], and Orthogonalized Flux-surface Aligned (OFA) $(\hat{e}_\rho, \hat{e}_\theta, \hat{e}_\phi)$ [right].	13
Figure 5: Flux function distribution $(\psi[R, Z])$, with flux-surfaces determined by contours of $\psi = \text{constant}$ (left), DIII-D Shot # 149468, 1905ms. The same flux-function distribution plotted in curvilinear coordinates $(\psi[\rho, \theta])$ (right). ($\circ \rightarrow$ LCFS, $\Delta \rightarrow$ plasma center, $\square \rightarrow$ OBMP)	15
Figure 6: Poloidal magnetic field distribution B_θ (left), calculated using a Semi-cartesian Spline fit (SS fit) to determine gradients in Eq. (3.14). Toroidal magnetic field distribution B_ϕ (right), calculated from Eq. (3.11). DIII-D Shot # 149468, 1905ms.	17
Figure 7: Radial and Poloidal GFA covariant unit vectors (\hat{e}_ζ) , scaled covariant basis vector $(\bar{e}_\zeta d\zeta)$, contravariant unit vectors (\hat{e}^ζ) , and vectors in contravariant directions scaled by contravariant scale factors $(\hat{e}^\zeta h^\zeta d\zeta)$ at flux-surface location (ρ, θ) .	22
Figure 8: Coordinate axes of the General Flux-surface Aligned (GFA) and Orthogonalized Flux-surface Aligned (OFA) local basis, determined by a Curvilinear Spline (CS) fitting method [Section 4.1]. Figure on right is an expanded view of the inset, showing coordinate axes orientations from the divertor region in greater detail.	25
Figure 9: Safety factors calculated by EFIT (red dash) and those calculated using an Asymmetric Miller (AM) model [Section 4.4] to set scale factors and fields for Eq. (3.38) (black).	27
Figure 10: Distributions of major radius $R[\rho, \theta]$ (left) and vertical position $Z[\rho, \theta]$ (right) relative to the flux-surface curvilinear coordinates (ρ, θ) .	30

- Figure 11: The field error \mathcal{E}_{field} between CS and SS predictions of $B\theta$, normalized by flux-surface constant values of Semi-Cartesian Spline (SS) $\langle B_\theta \rangle$, calculated by applying the FSA operation [Eq. (3.41)] to a field calculated using Eq. (3.14). 32
- Figure 12: Plasma sectors for error calculations. Upper right (upR), upper left (upL), and lower (low) regions. Inner and edge regions are separated by the $q=2$, $\rho \cong 0.7$ flux surface. 33
- Figure 13: Comparison of EFIT SS/CS flux-surfaces (RED) and Flux-equivalent Circular (FC) predictions of flux-surfaces (BLACK) [Eq. (4.3)], for Shot# 149468, 1905ms. 38
- Figure 14: The directions of FC-OFA and FC-GFA basis vectors are identical [Eq. (4.7)]. Magnification of inset shown on right. 40
- Figure 15: Distribution of poloidal magnetic field error \mathcal{E}_{field} (%) for the FC-OFA model [Eq. (4.2) and (4.8)] 42
- Figure 16: Comparison of the shapes of CS flux surfaces from EFIT (red dashed contours) with three orders of Single Fourier (SF) model flux surfaces (solid bold black contours). 45
- Figure 17: Field error \mathcal{E}_{field} for B_θ predictions using scale factors for an O(4) SF-OFA coordinate system [Eqs. (3.35), (3.20), (3.31), and (4.19)]. 47
- Figure 18: Comparison of EFIT flux surfaces (red dashes) with flux surface predictions for two orders of DF expansions [Eq. (4.18)] fitted to EFIT contours (circles, bold line). 49
- Figure 19: Field error \mathcal{E}_{field} for B_θ predictions using O[2] DF-OFA scale factors [Eqs. (3.35), (3.20), (3.31), and (4.19)]. 51
- Figure 20: Geometric relationship of R , Z , and θ with Miller parameters R_0 , a , x_δ , κ , ξ , and θ_m . 53
- Figure 21: Radial dependence of Miller plasma elongation κ (left axes) and modified triangularity x_δ (right axes), for Symmetric Miller (solid line) and Asymmetric Miller upper and lower (dotted and dashed) hemispheres of Shot# 149468, 1905ms. 55
- Figure 22: Symmetric Miller (left, black) and Asymmetric Miller (right, black) predictions for flux surfaces Eq. (4.21), compared to EFIT SS flux surfaces (red dashed). 56
- Figure 23: Comparison of AM-GFA basis vectors (narrow arrows) with AM-OFA basis vectors (bold arrows) [Eq. (4.26)] on sample AM flux surfaces. Magnification of inset shown on right. 58
- Figure 24: Field error \mathcal{E}_{field} for B_θ predictions using AM-OFA scale factors [Eq. (4.27)]. 59

Figure 25: Flux surface averages of positional error $\langle \mathcal{E}_{position} \rangle$ [red, Eq. (4.1)] and poloidal field error $\langle \mathcal{E}_{field} \rangle$ [black, Eq. (4.2)] for CS, FC, AM, DF, and SF coordinate system models.	61
Figure 26: Measurements of Toroidal Velocities (left) and Poloidal Velocities (right) for Deuterium (red) and Carbon (black) in Shot 149468 at 1905 ms.	70
Figure 27: Density measurements for Deuterium, Carbon, and Electrons (left) and ONETWO calculations of external particle and momentum sources for Deuterium (right). Black profiles plotted against left axes, red profiles plotted against right axes.	70
Figure 28: The system of sixteen plasma equations is converged at each radial location within the $q = 2$ flux surface ($\rho = 0.7$) until all normalized residuals are less than 0.01%	78
Figure 29: Flux-surface volume ($\nabla_{\rho} d\rho$) comparisons between plasma models. [Eq. (3.40)]	79
Figure 30: Electric Potential (left) and Radial Velocity (right) profiles, calculated using four separate geometric models. Default AM-OFA profiles shown as solid black lines.	81
Figure 31: Electric Potential Φ Asymmetries, Cosine (LEFT) and Sine (RIGHT), calculated using four separate geometric models. Default AM-OFA profiles shown as solid black lines.	81
Figure 32: Density n Asymmetries, Cosine (LEFT) and Sine (RIGHT), for Deuterium (TOP) and Carbon (BOTTOM), calculated using four separate geometric models. Default AM-OFA profiles shown as solid black lines.	82
Figure 33: Poloidal velocity (V_{θ}) asymmetries, cosine (left) and sine (right), for Deuterium (top) and Carbon (bottom), calculated using four separate geometric models. Default AM-OFA profiles shown as solid black lines.	83
Figure 34: Toroidal velocity (v_{ϕ}) asymmetries, cosine (left) and sine (right), for Deuterium (top) and Carbon (bottom), calculated using four separate geometric models. Default AM-OFA profiles shown as solid black lines.	84
Figure 35: Predicted Deuterium and Carbon density distributions using the AM-OFA geometry model.	85
Figure 36: Predicted Carbon Poloidal (left) and Toroidal (right) Velocity distributions, using the AM-OFA geometry model.	85
Figure 37: Normalized collision frequencies ($\hat{\nu}$) for Shot# 149468 at 1905 ms.	94
Figure 38: Basis vectors determined by analytic expressions for gradients of a position vector with poloidal variations in both major radius R and vertical displacement Z represented using 2 nd order Fourier expansions. Requires nine coefficients to be fitted from the Semi-Cartesian ψ distribution	95

Figure 39: Basis vectors determined by analytic expressions for gradients of a position vector with poloidal variations in minor radius r represented using a 4 th order Fourier expansion. Requires ten coefficients to be fitted from the Semi-Cartesian ψ distribution	95
Figure 40: Percent difference in Φ and V_r profiles calculated while neglecting asymmetries in Eq.(5.19) and Eq.(5.21), as compared to calculations which include asymmetries.	96
Figure 41: Poloidal (left) and Toroidal (right) Components of the Magnetic Field $(\vec{B} = B_\theta \hat{e}_\theta + B_\phi \hat{e}_\phi)$	96
Figure 42: Sources of Deuterium particles (left) and toroidal momentum (right), from neutral beam injection.	97
Figure 43: Distributions for Electric Potential (Φ) (left) and radial component of the Electric Field $(E_r = \frac{1}{h_\rho} \frac{\partial \Phi}{\partial \rho})$ (right)	97
Figure 44: Poloidal (left) and toroidal (right) components of the velocity vector $\vec{V} = V_r \hat{e}_r + V_\theta \hat{e}_\theta + V_\phi \hat{e}_\phi$	98

LIST OF SYMBOLS

ψ	Magnetic flux function
θ	Poloidal angle about the plasma center, relative to the outboard midplane
r	Minor radius
r_0	Minor radius at the last closed flux surface
a	Minor radius at the outboard midplane, on the last closed flux-surface
ρ	Normalized minor radius at outboard midplane $\left(\frac{r_0}{a}\right)$
R	Major radius of a plasma location relative to the tokamak central axis
Z	Vertical position of a plasma location relative to the plasma midplane
R_0	Major radius to the center of a plasma flux surface
ϵ	Ratio of plasma minor radius (a) to major radius (R_0)
ε	Ratio of flux surface last closed flux surface minor radius (r_0) to major radius (R_0)
n_i	Density of species i
\vec{V}_i	Velocity of species i
T_i	Temperature of species i
p_i	Isotropic pressure on species i
$\vec{\Pi}_i$	Pressure tensor for species i
Φ	Electric potential
\vec{E}	Electric field
\vec{A}	Magnetic vector potential
\vec{B}	Magnetic field

S_i^0	Particle source for species i
\vec{S}_i^1	Net momentum source for species i
\vec{F}_i	Net frictional force on species i
m_i	Mass of a particle of species i
e_i	Charge of a particle of species i
\vec{J}	Plasma current
$\nu_{i,j}$	Collision frequency for a distribution of species i incident on a stationary distribution of species j
$\tau_{i,j}$	Confinement time for species i incident on j , calculated by the inverse of collision frequency ($\nu_{i,j}^{-1}$)
$\mu_{i,j}$	Reduced mass of species i and j
$V_{th,i}$	Most-probable thermal velocity for species i ($\sqrt{\frac{2T_i}{m_i}}$)
η_m	Viscosity coefficient, where $m = 0 \rightarrow$ parallel, $m = 1,2 \rightarrow$ perpendicular, and $m = 3,4 \rightarrow$ gyroviscous
Ω_i	Gyrofrequency for species i
q	Plasma safety factor
f_i	Viscosity interpolation function for species i
F	Toroidal magnetic flux function (RB_ϕ)
S_ζ	Surfaces of constant poloidal ($\zeta = \theta$) or toroidal ($\zeta = \phi$) angle
Φ_ζ	Magnetic flux through poloidal ($\zeta = \theta$) or toroidal ($\zeta = \phi$) surfaces S_α
\hat{e}_ζ	Unit vector in ζ direction, [$\zeta = (\rho, \theta, \phi)$, $\zeta = (R, Z, \phi)$, or $\zeta = (x, y, z)$]
\vec{e}_ζ	Basis vector in k direction, [$\zeta = (\rho, \theta, \phi)$, $\zeta = (R, Z, \phi)$, or $\zeta = (x, y, z)$]

\vec{s}	Position vector used to relate curvilinear coordinate systems to absolute (x, y, z) coordinates
h_ζ	Scale factors for the ζ direction of a curvilinear coordinate system
\mathcal{H}	Area scale factor
\vec{G}	Metric tensor
$g_{k,l}$	Element of the metric tensor in k^{th} row, l^{th} column.
\mathcal{J}	Jacobian determinant of the covariant metric tensor
dl_ζ	Differential length element in the ζ direction
$d\mathbb{A}$	Differential area element in a plasma cross-section
$d\mathbb{V}$	Plasma differential volume element
\mathcal{E}	Error, in minor radius (subscript “position”) or poloidal magnetic field (subscript “field”)
κ	Plasma elongation
δ	Plasma triangularity
x_δ	Modified plasma triangularity ($x_\delta = \text{Sin}^{-1}\delta$)
θ_m	Poloidal angle of a triangle with length of vertical edge equal to Z
ξ	Poloidal angle of a triangle with length of horizontal edge equal to $R - R_0$
N_θ	Number of points used to approximate the poloidal shape of a flux surface
\perp	[Superscript] orthogonalized
$-$	[Overscript] mean radially-dependent value
\wedge	[Overscript] normalized, or a unit vector
\rightarrow	[Overscript] vector quantity

\sim	[Overscript] poloidal asymmetry used in a Fourier expansion to represent quantity
(α, β)	[Subscripts] used together to indicate indexes of a 2D matrix quantity
$(s; c)$	[Superscripts] used separately to indicate a Sine or Cosine asymmetry
$\langle \dots \rangle$	Flux surface average

LIST OF ABBREVIATIONS

BTE	Boltzmann Transport Equation
LCFS	Last Closed Flux Surface
OBMP	Outboard Midplane
FSA	Flux Surface Average
SS	<i>Semi-cartesian Spline</i> model
CS	<i>Curvilinear Spline</i> model
EC	<i>Edge flux-surface equivalent Circular</i> model
FC	<i>Flux-surface equivalent Circular</i> model
SM	<i>Symmetric Miller</i> model
AM	<i>Asymmetric Miller</i> model
SF	<i>Single Fourier</i> expansion model
DF	<i>Double Fourier</i> expansion model
GFA	<i>General Flux-surface Aligned</i> curvilinear coordinates
OFA	<i>Orthogonal Flux-surface Aligned</i> curvilinear coordinates

SUMMARY

Several methods are presented for improving upon the traditional analytic “circular” method for constructing a flux-surface aligned curvilinear coordinate system representation of equilibrium plasma geometry and magnetic fields, and the most accurate Asymmetric Miller method is applied to calculations of poloidal asymmetries in plasma density, velocity, and electric potential. Techniques for developing an orthogonalized coordinate system from a general curvilinear representation of plasma flux surfaces and for representing the poloidal component of the magnetic field in the orthogonalized curvilinear system are developed generally, in order to be applied to four plasma flux-surface models. The formalism for approximating flux surfaces originally presented by Miller [1] is extended to include poloidal asymmetries between the upper and lower plasma hemispheres, and is subsequently shown to be more accurate at fitting the shapes of flux surfaces calculated using EFIT than both the traditional “circular” model and two alternative curvilinear models of comparable complexity based on Fourier expansions of major radius, vertical position, and minor radius. Applying the coordinate system orthogonalization technique to these four models allows for calculations of the poloidal magnetic field which, upon comparison to a calculation of the poloidal field performed in a Cartesian system using the experimentally based EFIT prediction for the Grad-Shafranov equilibrium, demonstrates that the asymmetric “Miller” model is also superior to other methods at representing the poloidal magnetic field. A system of equations developed by representing the poloidal variations of velocity, density, and electric potential using $O(1)$ Fourier expansions in the flux-surface averaged neoclassical plasma continuity and momentum balances is solved using several variations of both the “Miller” and “circular” curvilinear models to set geometric scale factors, illustrating the effects that these improvements in geometric modeling have on tokamak fluid theory calculations.

CHAPTER 1

INTRODUCTION

This work was initially motivated by the recognition that the agreement of neoclassical fluid plasma rotation theory with experimental observations of fluid rotation velocities depended on how well the geometry of the computational model corresponded with the magnetic geometry of the experiment [2], [3], in particular as regards the representation of poloidal asymmetries in the magnetic geometry of the model and the capability of the calculation model to predict poloidal asymmetries in densities, rotation velocities, etc. However, the resulting investigation has broader implications for fluid transport and rotation models for tokamak plasmas.

The theoretical basis for tokamak plasma computations is the solution, in some approximation, of the Boltzmann transport equation for the distribution in space and velocity of one or more ion species and the electrons in the presence of electric and magnetic fields, which fields can be determined by solving the Maxwell electromagnetic equations in the presence of these distributions of plasma ions and electrons plus currents flowing in external magnets plus any externally produced electromagnetic fields. By taking velocity moments of the Boltzmann equations for the distribution functions, these equation can be replaced by a set of velocity-independent equations for moments (density, mass velocity, energy, etc.) with "transport" coefficients that must be evaluated by making approximate solutions of the Boltzmann equations. The resulting moment equations are the "fluid" equations involving generalized spatial gradient operators that depend on the choice of geometric model.

It can be shown, e.g. [4], that the leading order force balance requires that the magnetic fields and currents in the plasma lie on isobaric "flux surfaces" and that the largest mass flows are parallel to the magnetic field lines, that the next largest mass flows are perpendicular to the magnetic field lines but within the flux surfaces, and that the smallest mass flows are normal to the isobaric flux surfaces. In order to exploit these differences of magnitudes of mass velocities and of variations in other quantities in the

subsequent development, it is convenient to use the parallel and perpendicular directions within the flux surface and the normal direction to the flux surface to define a flux-surface aligned computational geometry for the fluid equations. Because the magnetic field lines do not cross the flux surfaces, these surfaces can be defined by the value of the flux function ψ representing the magnetic flux contained within the surfaces. The flux surface coordinates can be related to Cartesian coordinates by equating the force balance equations written in both systems to obtain the Grad-Shafranov equation.

The generalized spatial gradient operators for the flux-surface aligned curvilinear coordinates are determined by the way that flux surface shape and position vary with (ρ, θ) , the plasma parameters used to define the flux-surface. Setting this variation by directly fitting the Grad-Shafranov solutions for ψ using splines allows for a direct calculation of poloidal magnetic field, and gives the most accurate forms for the plasma moment equations. The complexity of this calculation leads to the development of simpler models to approximate the dependence of flux surface shape on (ρ, θ) , where $\rho[\psi]$ is the normalized radius. Considered in this thesis are the “circular”, “Miller”, double and single Fourier expansion models, which will be used to approximate the geometry of the upper single-null divertor plasma of DIII-D shot # 149468, at 1905ms. Differences among these curvilinear models for the plasma geometry influence the directions in which the components of the velocity moment equation are evaluated throughout the plasma, and affect the flux-surface average of plasma parameters. When the relationships developed from the first two velocity moments of the Boltzmann equation are used to develop a method for predicting plasma asymmetries in potential, density, and rotation velocities, the curvilinear coordinate models affect the resulting calculations, indicating that application of simple yet accurate models for the plasma shape has potential to improve a broad range of calculations based on neoclassical fluid theory.

CHAPTER 2

BASIC PLASMA THEORY

The velocity moments of the Boltzmann Transport Equation (BTE) for a Maxwellian plasma species under the influence of external magnetic and electric fields are the "fluid" equations; the first two moments describe conservation of particles and conservation of momentum in the three coordinate directions [5]. The components of these equations can be related to measurable plasma quantities such as densities, electric potential, rotation velocities, etc.; these relationships involve approximate kinetic theory calculations for collision frequencies, interspecies frictional forces, viscosity coefficients, and approximations for the effects of external sources of particles and momentum.

2.1. Continuity and Momentum Balance

The first two moments of the BTE

Continuity

$$\frac{\partial n}{\partial t} + \nabla \cdot (n\vec{V}) = S^0 \quad (2.1)$$

Momentum Balance

$$\frac{\partial}{\partial t} [mn\vec{V}] + \nabla \cdot \vec{M} = ne \left(\vec{E} + \vec{V} \times \vec{B} \right) + \vec{F} + \vec{S}^1 \quad (2.2)$$

involve generalized spatial gradient operators that depend on the choice of geometric model. In the momentum balance, \vec{F} is friction, and \vec{S}^1 is any external source of momentum.

In a steady-state system, the left of the continuity equation describes the divergence of the particle flux streaming through a volume, and can be expanded to represent the effects of spatial gradients in density and velocity separately. The term on the right is determined by any external or ionization particle sources.

In the momentum balance vector equation, the momentum stress tensor \vec{M} can be decomposed into kinetic terms dependent on the bulk motion of the plasma and thermodynamic terms represented by the pressure tensor (\vec{P}) [5].

$$\vec{M} = nm\vec{V}\vec{V} + \vec{P} \quad (2.3)$$

The divergence of the first term on the right of Eq. (2.3) is known as the convective derivative, and accounts for the inertial effects due to the rotation of the plasma at a mean velocity \vec{V} . It can be separated into a term dependent on the streaming from the continuity equation, and a term dependent on the divergence of the velocity.

$$\nabla \cdot (mn\vec{V}\vec{V}) = m\vec{V} \left(\nabla \cdot (n\vec{V}) \right) + mn \left((\vec{V} \cdot \nabla) \vec{V} \right) \quad (2.4)$$

The gradient of the pressure tensor can be written in terms of the anisotropic shear tensor ($\vec{\Pi}$) and the isotropic pressure (p). [5]

$$\nabla \cdot \vec{P} = \nabla \cdot \vec{\Pi} + \nabla p \quad (2.5)$$

Applying Eq. (2.5) to the momentum balance Eq. (2.2) in steady state yields the general form of the vector momentum balance equation used in this analysis.

$$\nabla \cdot (mn\vec{V}\vec{V}) + \nabla \cdot \vec{\Pi} + \nabla p = ne \left(\vec{E} + \vec{V} \times \vec{B} \right) + \vec{F} + \vec{S} \quad (2.6)$$

The first term of Eq. (2.6) accounts for the inertial effects present in a rotating plasma, and the second term represents the plasma viscous stress tensor, determined by the anisotropic pieces of the pressure tensor. The third term accounts for the forces due to the spatial gradient of isotropic pressure. The final three pieces describe body forces on a differential fluid volume: electromagnetic, frictional, and external momentum source effects, respectively. The above equations can be developed for the main deuterium ion species, the secondary carbon ion species, and for electrons.

2.2. Collision Frequencies

The interspecies collision frequencies between separate plasma species and self-collision frequencies between particles of the same species are necessary for calculations of the frictional effects and the parallel viscosity coefficients, respectively. For collisions between distributions of different species at the same temperature, the interspecies collision frequency for a moving distribution of species i incident on a distribution of species j can be computed from Fokker-Planck collision theory [6].

$$\nu_{i,j} = \frac{1}{6\sqrt{2}\pi^{3/2}\epsilon_0^2} \frac{n_j e_i^2 e_j^2 \sqrt{\mu_{i,j}} \ln[\Lambda_{i,j}]}{m_i T^{3/2}} \quad (2.7)$$

The Coloumb logarithm ($\ln[\Lambda]$) is given by: [7]

$$\ln[\Lambda_i] = \ln\left[\frac{x_{\max}}{x_{\min}}\right] = \ln\left[12\pi\sqrt{\frac{\epsilon_0^3 T^3}{n_j e_i^2 e_j^4}}\right] \quad (2.8)$$

Where $x_{\max} = \left(\frac{\epsilon_0 T_j}{n_j e_j^2}\right)$ is the Debye length, and $x_{\min} = \frac{|e_i e_j|}{4\pi\epsilon_0\mu_{i,j}V_{th}^2}$ is the 90° impact parameter.

Equation (2.7) can also be used to calculate the self-collision frequencies, if both species i and j are the same. In the plasma considered in this analysis, collision frequencies are generally $\sim 10^2 - 10^3 s^{-1}$ [Figure 1].

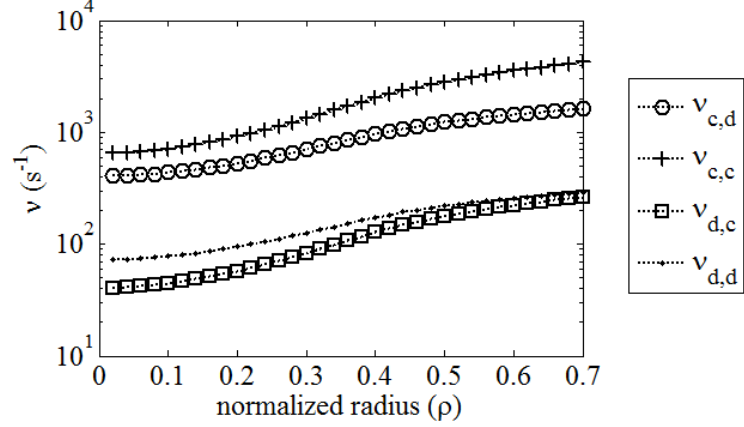


Figure 1: Interspecies and self-collision frequencies for DIII-D Shot # 149468, 1905ms.

In this analysis, the deuterium and carbon ion species are assumed to be in thermal equilibrium, allowing their interspecies collision frequencies to be calculated using Eq. (2.7). The electron and ion species temperature profiles are typically not equal, which implies that a more advanced form of Eq. (2.7) which differentiates between particle species is necessary to calculate ion-electron interspecies collision frequencies. However, because the ion-electron reduced mass ($\mu_{i,e}$) can be approximated as the electron mass, the electron-ion interspecies collisions can be neglected relative to the deuterium-carbon interspecies collisions in the frictional component of the momentum balance equation, making calculations of $\nu_{i,e}$ unnecessary.

2.3. Viscosity Formalism

The viscous drag forces due to anisotropies in the pressure tensor significantly influence the plasma flows. The form of the anisotropic shear tensor used in this analysis was first derived by Braginskii in Cartesian coordinates [6]. This shear tensor was later generalized to orthogonal curvilinear flux-surface coordinates in a toroidally axisymmetric plasma [8]. An updated form of this generalized shear tensor is used in this analysis to calculate the viscous contributions to the poloidal and toroidal components of the momentum balance equation [Appendix A.3].

In Braginskii's original formulation, the magnitude of the viscous forces in a collisional plasma parallel to the field lines, perpendicular to the field lines, and

associated with the cyclotron gyration about the field lines were represented by parallel, perpendicular, and gyroviscous viscosity coefficients [9].

$$\begin{aligned}\eta_0 &= 0.96nT\tau \\ \eta_1 &= \frac{3}{10} \frac{nT}{\Omega^2\tau}, \quad \eta_2 = 4\eta_1 \\ \eta_3 &= \frac{1}{2} \frac{nT}{\Omega}, \quad \eta_4 = 2\eta_3\end{aligned}\tag{2.9}$$

In general, these viscosity coefficients differ in magnitude by factors of the product of the ion self-collision time $\left(\tau = \frac{1}{\nu}\right)$ and gyrofrequency (Ω). Their product is order $\Omega\tau \cong 10^5 - 10^6$ in the central plasma of the shot considered in this analysis, so that the viscosity coefficients can be ordered as $\eta_0 \gg \eta_{3,4} \simeq \eta_0/\Omega\tau \gg \eta_{1,2} \simeq \eta_0/(\Omega\tau)^2$.

It has been shown that this original formalism for a collisional plasma can be extended to the strong rotation, collisionless plasma case [10]. This extension is implemented in this analysis by replacing the collisional parallel viscosity coefficient η_0 from Eq. (2.9) with a form valid in the Pfirsch-Schluter and banana-plateau regions, dependent on a collisionality interpolation function (f_i).

$$\eta_{0,i} = \frac{n_i m_i V_{th,i} q R_0 \varepsilon^{-3/2} \hat{v}_{i,i}}{(1 + \varepsilon^{-3/2} \hat{v}_{i,i})(1 + \hat{v}_{i,i})} = 2 \frac{n_i T_i}{v_{i,i}} f_i\tag{2.10}$$

$$f_i = \frac{\hat{v}_{i,i}^2}{(\varepsilon^{3/2} + \hat{v}_{i,i})(1 + \hat{v}_{i,i})}, \quad \hat{v}_{i,i} = v_{i,i} \frac{q R_0}{V_{th,i}}\tag{2.11}$$

This form approximates the variation in parallel viscosity from the collisional regime through the plateau region into the collisionless regime for species i . It is dependent on the ion self-collision frequency ($v_{i,i}$) [Eq. (2.7)], the safety factor (q) [Eq. (3.39)], the ratio of minor to major radius ($\varepsilon = \frac{r_0}{R_0}$), and the most probable thermal velocity ($V_{th,i} = \sqrt{2T_i/m_i}$). The forms of the viscosity coefficient and collisionality interpolation function have been modified from those used in prior analyses [2] in order to isolate the poloidal dependence into the interpolation function f_i . The ion self-

collision frequency can be computed from Fokker-Planck collision theory using Eq. (2.7); both q and ε are dependent on the magnetic field and plasma flux-surface structure.

Braginskii's form for the gyroviscous viscosity coefficient is independent of the plasma collisionality, allowing it to be applied in its unmodified form in all collision regimes.

$$\eta_{3,i} = \frac{1}{2} \frac{n_i T_i}{\Omega_i}, \quad \eta_{4,i} = \frac{n_i T_i}{\Omega_i} \quad (2.12)$$

The components of the pressure tensor dependent on η_0 typically dominate the viscosity calculation because of the $O(10^{-6})$ difference between η_0 and $\eta_{3,4}$. However, the gyroviscosity becomes significant in damping toroidal rotation in toroidally axisymmetric plasmas, where the parallel component of the toroidal viscous stress vanishes identically when the flux-surface averaging operation is applied to the toroidal angular momentum balance [8]. The perpendicular viscosity is negligibly small in comparison to both the parallel and gyroviscous viscosity, and will be neglected.

2.4. Electromagnetic, Friction, and External Source Effects

The external forces on the right of the momentum balance equation (2.6) are due to electromagnetic effects, frictional forces between plasma ion species, and external sources of particles and momentum.

The general expression for the electric field in terms of the electric potential distribution (Φ) and the magnetic vector potential (\vec{A}) is

$$\vec{E} = -\vec{\nabla}\Phi - \frac{\partial \vec{A}}{\partial t} \quad (2.13)$$

Because of the toroidal axisymmetry of a tokamak, the toroidal electric field is determined entirely by the inductive electric field $E_\phi^A = \frac{\partial A_\phi}{\partial t}$. Because the magnetic vector potential can be approximated by the plasma current $\vec{A} \cong \vec{J} \cong J \hat{e}_\phi$, the inductive contribution to the electric field is negligible in directions other than the toroidal. The field in these directions is determined only by the spatial gradient of the electric potential.

Deuterium is the primary ion species present in DIII-D shots ($n_d \cong 10^{19} m^{-3}$), with densities two orders of magnitude larger than the carbon impurities from wall sputtering ($n_c \cong 10^{17} m^{-3}$) [Figure 27]. In this analysis, carbon and deuterium are modeled as separate ion species, and the frictional force between them is predicted by a simple Lorentz friction model dependent on the interspecies collision frequency ($\nu_{i,j}$), calculated using Eq. (2.7).

$$F_{i,j} = -n_i m_i \nu_{i,j} (V_i - V_j) \quad (2.14)$$

Because $m_e \cong \mu_{i,e} \ll m_i$, the contributions of ion-electron collisions to friction calculations using Eq.(2.14) are negligibly small in comparison to the ion-ion interspecies collisions.

The electron density can be related to the ion charge density by requiring plasma charge neutrality, ($n_e e_e = n_c e_c + n_d e_d$). The net frictional contribution to the total momentum balance for the plasma, calculated by adding Eq. (2.14) for both species, vanishes, as it must.

External momentum is added to the DIII-D core plasma through neutral beam injection, which makes significant momentum contributions only in the toroidal direction.

CHAPTER 3

DEFINITION AND ORTHOGONALIZATION OF A GENERAL CURVILINEAR COORDINATE SYSTEM

In an axisymmetric plasma, the Grad-Shafranov equation can be applied to determine the relationship between the steady-state magnetic flux function ψ , plasma pressure $p[\psi]$, and the flux-surface constant quantity ($F[\psi] = R B_\phi$) in a poloidal plasma cross-section. Spatial gradients of the resulting ψ distribution are used to define the magnetic field distribution, and can be used to develop a flux-surface aligned orthogonal curvilinear coordinate system, which simplifies calculations of the components of the continuity and momentum balance equation [Eqs. (2.1) and (2.6)].

3.1. Defining Flux Surfaces Using the Plasma Flux Function (ψ).

The poloidal and toroidal magnetic fluxes can be defined in terms of the magnetic field \vec{B} and surfaces of constant poloidal angle (S_θ) and constant toroidal angle (S_ϕ) [11].

$$\begin{aligned}\Phi_\theta &\equiv \int_{S_\theta} \vec{B} \cdot d\vec{S}_\theta = 2\pi\psi \\ \Phi_\phi &\equiv \int_{S_\phi} \vec{B} \cdot d\vec{S}_\phi\end{aligned}\tag{3.1}$$

Flux surfaces are defined by toroidally-symmetric surfaces enclosing constant values of poloidal magnetic flux, which is often written in terms of the magnetic flux function (ψ) [Eq. (3.1)]. A surface at constant toroidal angle (S_ϕ) will correspond to a poloidal cross-section of the flux surface, and is normal to all flux surfaces. The surfaces (S_θ) used to define poloidal magnetic flux are enclosed entirely within the flux-surface containing a fixed value of ψ , and encircle the tokamak toroidally. Because of axisymmetry, the S_θ surface is also perpendicular to the S_ϕ surface.

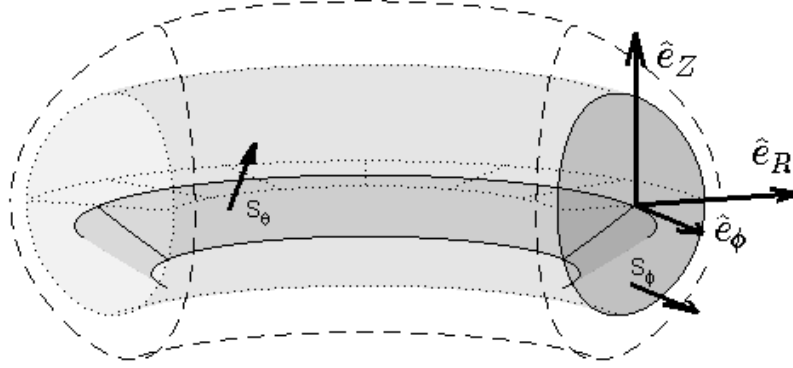


Figure 2: Locations of the S_θ and S_ϕ surfaces used to define poloidal and toroidal magnetic flux.

The Grad-Shafranov equation can be used to determine the distribution of ψ in a poloidal cross-section of the plasma (surface S_ϕ). It can be derived from:

Force Balance

$$\vec{J} \times \vec{B} = \nabla p \quad (3.2)$$

Ampere's Law

$$\nabla \times \vec{B} = \mu_0 \vec{J} \quad (3.3)$$

Solenoidal Law

$$\nabla \cdot \vec{B} = 0 \quad (3.4)$$

Equation (3.2) is a simplified version of the composite plasma momentum balance for all plasma species, where (\vec{J}) is the plasma current, (\vec{B}) is the magnetic field, and (p) is the plasma pressure [4]. Equations (3.3)-(3.4) are two of Maxwell's equations. The resulting Grad-Shafranov equation takes the form [12]

$$R^2 \nabla \cdot \left(\frac{\nabla \psi}{R^2} \right) = -\mu_0 R^2 \frac{dp}{d\psi} - F \frac{dF}{d\psi} \quad (3.5)$$

where \vec{B} and \vec{J} can be expressed in terms of the flux function $\psi[R, Z]$ and $F[\psi] = RB_\phi$ by:

$$\vec{B} = \frac{1}{R} \nabla \psi \times \hat{e}_\phi + \frac{F}{R} \hat{e}_\phi \quad (3.6)$$

$$\mu_0 \vec{J} = \frac{1}{R} \frac{dF}{d\psi} \nabla \psi \times \hat{e}_\phi - R \nabla \cdot \left(\frac{\nabla \psi}{R^2} \right) \hat{e}_\phi \quad (3.7)$$

The DIII-D EFIT code is used to solve the system of differential equations Eq. (3.5) – Eq. (3.7), and return a 2D distributions of ψ for a poloidal plasma slice of Shot 149468 at 1905ms, in terms of major radius R and vertical displacement Z [13].

Contours of $\psi = \text{constant}$ in the poloidal plane (surface S_ϕ) can be used to determine the locations of flux surfaces within the last closed flux surface (LCFS). These flux surface contours can be used to define a transformation from (R, Z) coordinate space to a set of coordinate variables describing the value of the flux-function (ψ) contour and the poloidal angle from the flux-surface center (θ). In this analysis, the normalized outboard-midplane (OMP) minor radius ($\rho[\psi] = \frac{r_0[\psi]}{a}$) will be used to parameterize flux surfaces, and can be directly related to the value of the flux-function ψ used to define the flux-surface contour. The variable a will be used for the OBMP minor radius at the LCFS. Distributions of F , p , and ψ are functions of normalized minor radius (ρ).

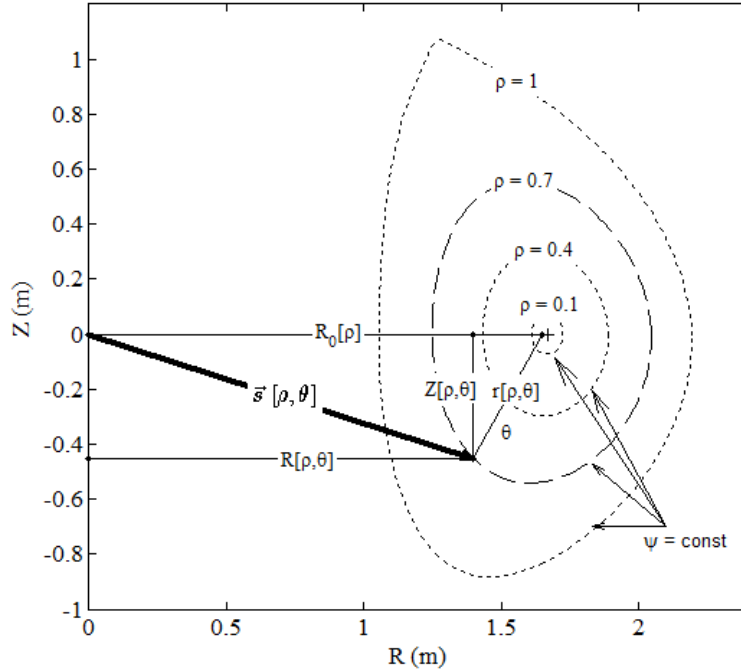


Figure 3: Sample flux surfaces of $\psi = \text{const.}$ for DIII-D Shot# 149468, 1905ms. The coordinates (R, Z) can be transformed to curvilinear coordinates (ρ, θ) related to position on flux-surfaces.

3.2. Representation of Magnetic Fields in Semi-Cartesian and Curvilinear Coordinate Systems

Equation (3.6), which is the differential form of the definition for the flux function [Eq. (3.1)], can be applied in any coordinate system to calculate the magnitude and direction of the magnetic field from the magnetic flux-function (ψ) distribution. Because the ψ distribution is returned by EFIT as a function of R and Z , it is straightforward to represent the components of the magnetic field in a semi-Cartesian coordinate system with orthogonal unit vectors ($\hat{e}_R, \hat{e}_Z, \hat{e}_\phi$) [Figure 4, center] using gradients of ψ with respect to both coordinate variables. However, if the ψ distribution is first mapped to a flux-surface aligned curvilinear coordinate system with orthogonalized unit vectors ($\hat{e}_\rho, \hat{e}_\theta, \hat{e}_\phi$), [Figure 4, right] the poloidal magnetic field can be defined using only radial gradients of ψ .

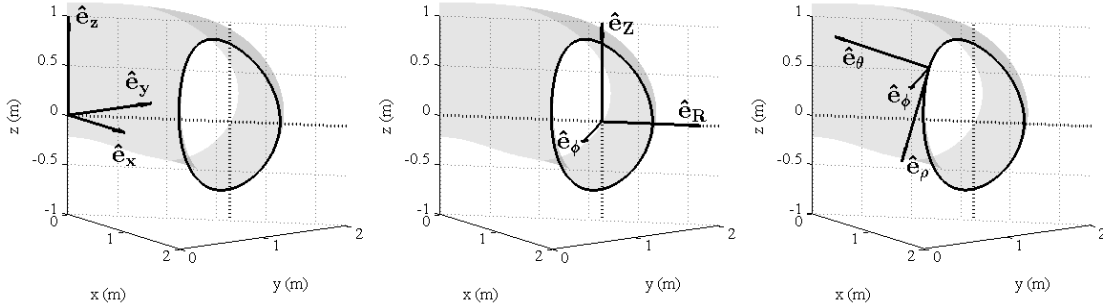


Figure 4: Three sets of normalized basis vectors. Cartesian ($\hat{e}_x, \hat{e}_y, \hat{e}_z$) [left], semi-Cartesian ($\hat{e}_R, \hat{e}_Z, \hat{e}_\phi$) [center], and Orthogonalized Flux-surface Aligned (OFA) ($\hat{e}_\rho, \hat{e}_\theta, \hat{e}_\phi$) [right].

For a flux surface in an axisymmetric plasma, a semi-Cartesian set of coordinate axes ($\hat{e}_R, \hat{e}_Z, \hat{e}_\phi$) can be defined so that the (\hat{e}_R, \hat{e}_Z) directions are fixed and orthogonal throughout any poloidal plasma cross-section. In order to develop this set of coordinate axes, the position vector \vec{s} in the global ($\hat{e}_x, \hat{e}_y, \hat{e}_z$) bases [Figure 4, left] can be written in terms of major radius (R), vertical displacement (Z), and negative toroidal angle ($-\phi$).

$$\vec{s}[R, Z, \phi] = R \cos[-\phi] \hat{e}_x + R \sin[-\phi] \hat{e}_y + Z \hat{e}_z \quad (3.8)$$

From this position vector, the semi-Cartesian basis vectors can be developed by taking gradients of Eq. (3.8) with respect to ($R, Z, -\phi$).

$$\begin{aligned}
\vec{e}_R &= \frac{\partial \vec{s}}{\partial R} = \hat{e}_x \cos \phi - \hat{e}_y \sin \phi = \hat{e}_R \\
\vec{e}_Z &= \frac{\partial \vec{s}}{\partial Z} = \hat{e}_z = \hat{e}_Z \\
\vec{e}_\phi &= \frac{\partial \vec{s}}{\partial \phi} = -R(\hat{e}_x \sin \phi + \hat{e}_y \cos \phi) = h_\phi \hat{e}_\phi
\end{aligned} \tag{3.9}$$

The radial \vec{e}_R and vertical \vec{e}_Z basis vectors form a set of orthogonal unit vectors, invariant within each poloidal cross-section of constant ϕ , equivalent to a two-dimensional Cartesian coordinate system. The \vec{e}_R basis vector is always directed towards increasing major radius R , perpendicular to the tokamak central axis. The \vec{e}_Z basis vector is always parallel to the central axis, in direction of increasing Z , and aligned with the global unit vector \hat{e}_z . The toroidal basis vector \vec{e}_ϕ is perpendicular to the other two, and directed opposite to the direction of increasing toroidal angle ϕ in order to form a right-handed coordinate system; it is related to the toroidal unit vector \hat{e}_ϕ by the toroidal scale factor $h_\phi = R$.

Using the basis vectors from Eq. (3.9), the position vector \vec{s} from Eq. (3.8) can be rewritten in terms of R and Z as:

$$\vec{s} = R \hat{e}_R[\phi] + Z \hat{e}_Z \tag{3.10}$$

The distribution of ψ calculated by EFIT as a solution to the Grad Shafranov equation is in terms of R and Z . Interpolating on this distribution to select contours of $\psi = \text{constant}$ reveals the locations of flux surfaces [Figure 5, left]. Once these flux-surfaces are identified, any distribution in (R, Z) coordinates can be mapped to the flux-surface curvilinear coordinates (ρ, θ) ; for the ψ distribution, a plot in terms of the curvilinear coordinates clearly shows the relationship between ψ and ρ , and that ψ is independent of θ [Figure 5, right].

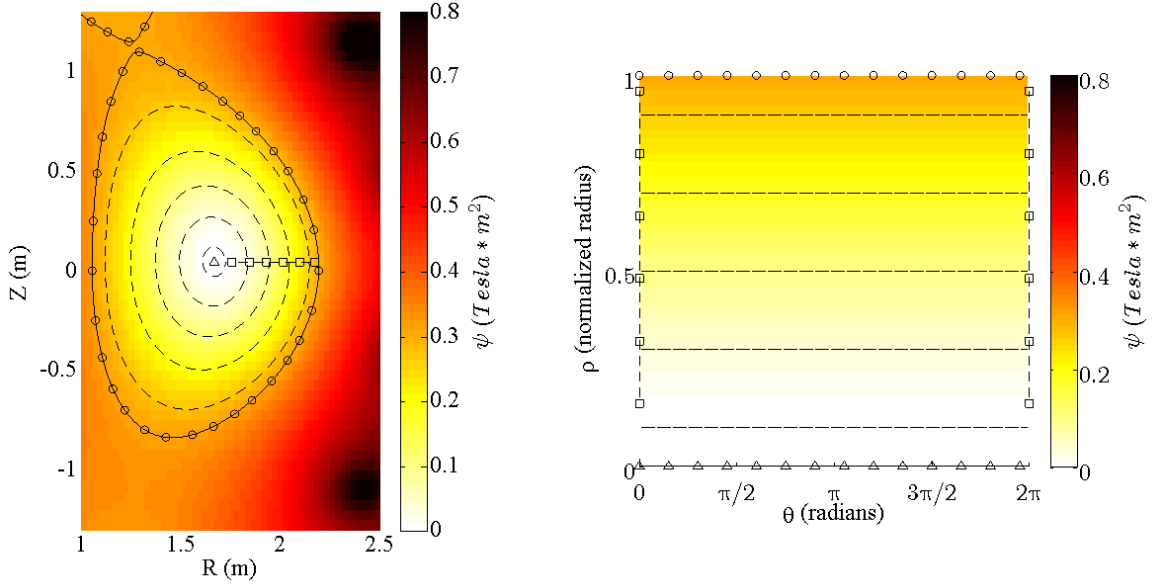


Figure 5: Flux function distribution ($\psi[R, Z]$), with flux-surfaces determined by contours of $\psi = \text{constant}$ (left), DIII-D Shot # 149468, 1905ms. The same flux-function distribution plotted in curvilinear coordinates ($\psi[\rho, \theta]$) (right). ($\circ \rightarrow$ LCFS, $\Delta \rightarrow$ plasma center, $\square \rightarrow$ OBMP)

Unlike the system of semi-Cartesian basis vectors from Eq. (3.9) which only vary with toroidal angle ϕ , the coordinate axes in curvilinear $(\rho, \theta, -\phi)$ coordinates are also dependent on the flux surfaces ρ and poloidal angle θ . These coordinate axes can be constructed so that the poloidal basis direction remains parallel to flux-surface contours in a poloidal cross-section, and so that the radial basis direction remains perpendicular to flux-surface contours. This will be referred to as a curvilinear Orthogonalized Flux-surface Aligned (OFA) coordinate system with unit vectors $(\hat{e}_\rho^\perp, \hat{e}_\theta^\perp, \hat{e}_\phi^\perp)$, and scale factors $(h_\rho^\perp, h_\theta^\perp, h_\phi^\perp)$ to relate the changes in coordinates variables $(\rho, \theta, -\phi)$ to distances in the global bases. The position vector \vec{s} in curvilinear coordinates can be parameterized in terms of normalized minor radius (ρ), poloidal angle (θ), and negative toroidal angle ($-\phi$), by utilizing Eq. (3.10) with values for R and Z given as functions of ρ and θ .

Equation (3.6) can be separated to give expressions for the magnitude of the components of the magnetic field in the toroidal and poloidal directions. The poloidal component of the magnetic field involves a spatial gradient of ψ .

$$\begin{aligned}
\vec{B}_\phi &= \frac{F}{R} \hat{e}_\phi = \frac{F}{R} \\
\vec{B}_\theta &= \frac{1}{R} \nabla \psi \times \hat{e}_\phi
\end{aligned} \tag{3.11}$$

The first piece of Eq. (3.11) gives the toroidal component of the magnetic field vector in terms of the distribution $F[\psi]$ and the major radius, directed along the \hat{e}_ϕ unit vector. This calculation is straightforward in both semi-Cartesian and Orthogonalized Flux-surface Aligned (OFA) curvilinear coordinates, as it does not involve any spatial gradients.

The second piece of Eq. (3.11) expresses the magnitude of the poloidal magnetic field in terms of the gradient of ψ , the major radius, and the toroidal unit vector. Mathematically equivalent expressions for the magnitude of the poloidal magnetic field can be developed by applying the gradient operator for both semi-Cartesian coordinates and curvilinear coordinates to Eq. (3.11). These gradients will depend on the scale factors h_R , h_Z , and h_ϕ for the semi-Cartesian system, and h_ρ^\perp , h_θ^\perp , and h_ϕ^\perp for the OFA curvilinear system.

$$(\nabla \psi)_{R,Z,\phi} = \frac{\partial \psi}{\partial R} \vec{e}_R + \frac{\partial \psi}{\partial Z} \vec{e}_Z + \frac{\partial \psi}{\partial \phi} \vec{e}_\phi = \frac{1}{h_R} \frac{\partial \psi}{\partial R} \hat{e}_R + \frac{1}{h_Z} \frac{\partial \psi}{\partial Z} \hat{e}_Z - \frac{1}{h_\phi} \frac{\partial \psi}{\partial \phi} \hat{e}_\phi \tag{3.12}$$

$$(\nabla \psi)_{\rho,\theta,\phi} = \frac{\partial \psi}{\partial \rho} \vec{e}_\rho + \frac{\partial \psi}{\partial \theta} \vec{e}_\theta + \frac{\partial \psi}{\partial \phi} \vec{e}_\phi = \frac{1}{h_\rho^\perp} \frac{\partial \psi}{\partial \rho} \hat{e}_\rho^\perp + \frac{1}{h_\theta^\perp} \frac{\partial \psi}{\partial \theta} \hat{e}_\theta^\perp - \frac{1}{h_\phi} \frac{\partial \psi}{\partial \phi} \hat{e}_\phi \tag{3.13}$$

Both general gradient expressions in Eq. (3.12) and Eq. (3.13) can be immediately simplified by the requirements of axisymmetry; the gradients with respect to toroidal angle are zero, because ψ is not dependent on ϕ . Because the \vec{e}_R and \vec{e}_Z basis vectors in the semi-Cartesian (R, Z, ϕ) coordinate system are identical to the unit vectors, the scale factors are $h_R = h_Z = 1$ in Eq. (3.12). Then, substituting Eq. (3.12) into the second piece of Eq. (3.11) yields an expression for the magnitude of the poloidal magnetic field in terms of gradients of ψ with respect to R and Z .

$$\vec{RB}_\theta = \nabla\psi \times \hat{e}_\phi = -\frac{\partial\psi}{\partial Z}\hat{e}_R + \frac{\partial\psi}{\partial R}\hat{e}_Z$$

$$|(RB_\theta)_{R,Z,\phi}| = \sqrt{\left(\frac{\partial\psi}{\partial Z}\right)^2 + \left(\frac{\partial\psi}{\partial R}\right)^2}$$
(3.14)

Because EFIT returns the ψ distribution data in terms of R and Z , it is straightforward to apply a numeric method to calculate the gradients in Eq. (3.14). In this analysis, spline-fits of the 65 data-points from EFIT describing the ψ distribution [Figure 5, left] in both coordinate directions are used to approximate the gradients, a method which will be referred to as the *Semi-Cartesian Spline* (SS) method of calculating B_θ .

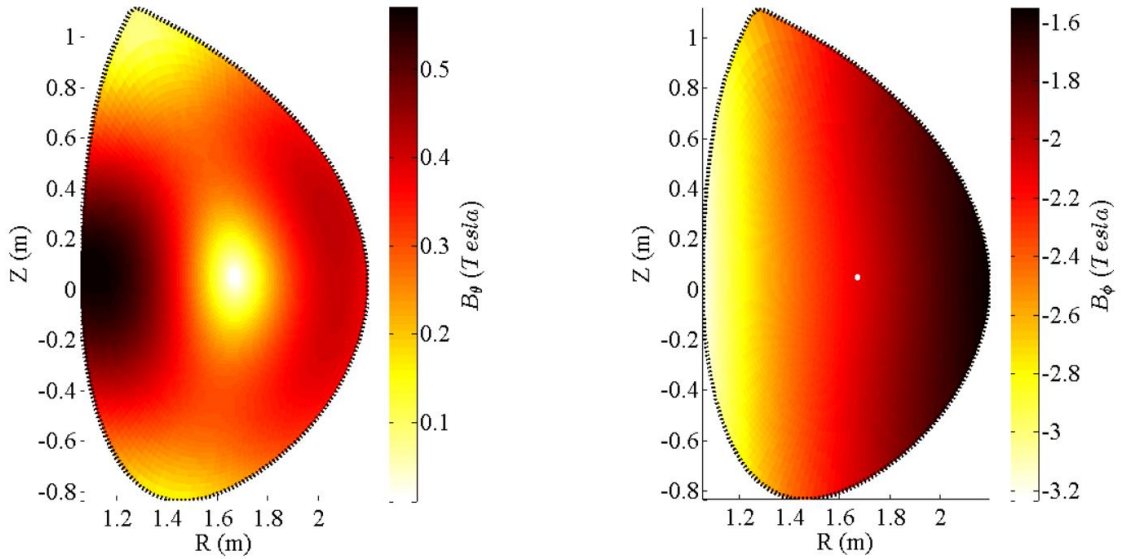


Figure 6: Poloidal magnetic field distribution B_θ (left), calculated using a Semi-cartesian Spline fit (SS fit) to determine gradients in Eq. (3.14). Toroidal magnetic field distribution B_ϕ (right), calculated from Eq. (3.11). DIII-D Shot # 149468, 1905ms.

By applying the gradient operator for curvilinear coordinates [Eq. (3.13)] in Eq. (3.11), a relationship between the poloidal magnetic field and the Orthogonal Flux-surface Aligned (OFA) curvilinear local basis $(\hat{e}_\rho^\perp, \hat{e}_\theta^\perp, \hat{e}_\phi^\perp)$ can be developed.

$$\vec{RB}_\theta = \nabla\psi \times \hat{e}_\phi = -\frac{1}{h_\theta^\perp} \frac{\partial\psi}{\partial\theta} \hat{e}_\theta^\perp + \frac{1}{h_\rho^\perp} \frac{\partial\psi}{\partial\rho} \hat{e}_\rho^\perp$$

$$\left(\vec{RB}_\theta\right)_{\rho,\theta,\phi}^\perp = \frac{\partial\psi}{\partial l_\rho^\perp} \hat{e}_\rho^\perp = \frac{1}{h_\rho^\perp} \frac{\partial\psi}{\partial\rho} \hat{e}_\rho^\perp$$
(3.15)

Because the OFA coordinate system is defined so that ψ is constant on flux surface contours, the gradient $\partial\psi/\partial\theta = 0$. Thus, the final expression for the magnitude of RB_θ given in Eq. (3.15) is independent of the poloidal scale factor h_θ^\perp , determined only by the radial scale factor h_ρ^\perp and radial gradient of ψ [4]. The vector \vec{B}_θ from Eq. (3.15) is confined to the poloidal cross-section plane S_ϕ and directed normal to the flux surfaces in the \hat{e}_ρ^\perp direction.

Equation (3.15) allows the magnitude of the poloidal magnetic field to be determined in any Orthogonal Flux-surface Aligned (OFA) coordinate system with known scale factors. It is useful to define expressions for “mean” values of magnetic fields components which are independent of poloidal angle, in terms of central major radius R_0 and the radial gradient of average minor radius $\left(\frac{\partial r_0}{\partial \rho}\right)$.

$$\bar{B}_\theta = \frac{1}{R_0} \left(\frac{\partial r_0}{\partial \rho} \right)^{-1} \frac{\partial \psi}{\partial \rho}, \quad \bar{B}_\phi = \frac{F}{R_0} \quad (3.16)$$

The definitions for the poloidal dependence of the magnetic field components shown in Eq. (3.11) and Eq. (3.15) can be rewritten in terms of the quantities from Eq. (3.16). These definitions will be used through the remainder of this analysis.

$$\begin{aligned} B_\phi &= \frac{F}{h_\phi} = R_0 \frac{\bar{B}_\phi}{h_\phi} \\ B_\theta &= \frac{1}{h_\phi h_\rho^\perp} \frac{\partial \psi}{\partial \rho} = R_0 \frac{\partial r_0}{\partial \rho} \frac{\bar{B}_\theta}{h_\rho^\perp h_\phi} \end{aligned} \quad (3.17)$$

3.3. General Flux-surface Aligned (GFA) Curvilinear Coordinate System

Any method of representing values for R and Z on flux surfaces in terms of a flux-surface dependent variable (normalized OBMP minor radius ρ), poloidally dependent variable (angle θ), and toroidally dependent variable (angle ϕ) can be used to develop a *General Flux-surface Aligned* (GFA) curvilinear coordinate system. The basis vectors, unit vectors, scale factors, and metric tensor for this system will be dependent on gradients of the position vector with respect to the coordinate variables ρ , θ , and ϕ [11], and the radial and poloidal coordinate axes may not be orthogonal. The expressions

for GFA basis vectors, scale factors, and differential volume elements can be used as a basis for developing the Orthogonal Flux-surface Aligned (OFA) curvilinear coordinate system needed to calculate the poloidal component of the magnetic field [Eq. (3.15)].

The covariant basis vectors $(\vec{e}_\rho^{co}, \vec{e}_\theta^{co}, \vec{e}_\phi^{co})$ for the GFA curvilinear $(\rho, \theta, -\phi)$ coordinates in an axisymmetric plasma can be calculated by the gradients with respect to ρ and θ of the semi-Cartesian representation for the plasma position vector \vec{s}

$(\vec{e}_k^{co} = \frac{\partial \vec{s}}{\partial \zeta_k})$ [Eq. (3.10)]. Individual basis vectors components can be written in terms of the radial and poloidal gradients of R and Z , and the semi-Cartesian unit vectors.

$$\begin{aligned} \vec{e}_\rho^{co} &= \frac{\partial R}{\partial \rho} \hat{e}_R + \frac{\partial Z}{\partial \rho} \hat{e}_Z \\ \vec{e}_\theta^{co} &= \frac{\partial R}{\partial \theta} \hat{e}_R + \frac{\partial Z}{\partial \theta} \hat{e}_Z \\ \vec{e}_\phi^{co} &= R \frac{\partial \hat{e}_R}{\partial \phi} = R \hat{e}_\phi \end{aligned} \quad (3.18)$$

The GFA covariant basis vectors given in Eq. (3.18) can be normalized to obtain unit vectors in these coordinate axes directions, with magnitudes given by the covariant scale factors.

$$\begin{aligned} \hat{e}_k^{co} &= \frac{\vec{e}_k^{co}}{h_k^{co}} \\ k &= (\rho, \theta, \phi) = (\zeta_1, \zeta_2, \zeta_3) \end{aligned} \quad (3.19)$$

$$h_\rho^{co} = \left| \vec{e}_\rho^{co} \right| = \sqrt{\left(\frac{\partial R}{\partial \rho} \right)^2 + \left(\frac{\partial Z}{\partial \rho} \right)^2}, \quad h_\theta^{co} = \left| \vec{e}_\theta^{co} \right| = \sqrt{\left(\frac{\partial R}{\partial \theta} \right)^2 + \left(\frac{\partial Z}{\partial \theta} \right)^2}, \quad h_\phi^{co} = \left| \vec{e}_\phi^{co} \right| = R \quad (3.20)$$

The covariant scale factors relate the magnitudes of the basis vectors \vec{e}_k^{co} to differential changes in the curvilinear variables (ρ, θ, ϕ) . Thus, the differential area element in a plasma cross-section can be calculated by multiplying the cross-product of the radial and poloidal basis vectors by $(d\rho d\theta)$, and will be represented using the area scale-factor \mathcal{H} .

$$\begin{aligned}
d\mathbf{A} &= \vec{e}_\rho \times \vec{e}_\theta \, d\rho d\theta = \mathcal{H} d\rho d\theta \\
\mathcal{H} &= \left(\frac{\partial R}{\partial \rho} \frac{\partial Z}{\partial \theta} - \frac{\partial Z}{\partial \rho} \frac{\partial R}{\partial \theta} \right) > 0
\end{aligned} \tag{3.21}$$

The covariant basis vectors from Eq. (3.18) can be used to calculate the covariant metric tensor \vec{G}^{co} , with elements given by $(g_{k,l}^{co} = \vec{e}_k^{co} \cdot \vec{e}_l^{co})$.

$$\vec{G}^{co} = \begin{pmatrix} g_{\rho,\rho}^{co} & g_{\rho,\theta}^{co} & 0 \\ g_{\theta,\rho}^{co} & g_{\theta,\theta}^{co} & 0 \\ 0 & 0 & g_{\phi,\phi}^{co} \end{pmatrix} = \begin{pmatrix} (h_\rho^{co})^2 & \frac{\partial R}{\partial \rho} \frac{\partial R}{\partial \theta} + \frac{\partial Z}{\partial \rho} \frac{\partial Z}{\partial \theta} & 0 \\ \frac{\partial R}{\partial \rho} \frac{\partial R}{\partial \theta} + \frac{\partial Z}{\partial \rho} \frac{\partial Z}{\partial \theta} & (h_\theta^{co})^2 & 0 \\ 0 & 0 & (h_\phi^{co})^2 \end{pmatrix} \tag{3.22}$$

The contravariant metric tensor \vec{G}_{con} is the inverse of the covariant metric tensor. [11]

$$\begin{aligned}
\vec{G}_{con} &= (\vec{G}^{co})^{-1} = \begin{pmatrix} g_{con}^{\rho,\rho} & g_{con}^{\rho,\theta} & 0 \\ g_{con}^{\theta,\rho} & g_{con}^{\theta,\theta} & 0 \\ 0 & 0 & g_{con}^{\phi,\phi} \end{pmatrix} \\
&= \frac{1}{\mathcal{J}^2} \begin{pmatrix} g_{\theta,\theta}^{co} g_{\phi,\phi}^{co} & -g_{\theta,\rho}^{co} g_{\phi,\phi}^{co} & 0 \\ -g_{\rho,\theta}^{co} g_{\phi,\phi}^{co} & g_{\rho,\rho}^{co} g_{\phi,\phi}^{co} & 0 \\ 0 & 0 & g_{\rho,\rho}^{co} g_{\theta,\theta}^{co} - g_{\rho,\theta}^{co} g_{\theta,\rho}^{co} \end{pmatrix} \\
&= \frac{1}{\mathcal{H}^2} \begin{pmatrix} (h_\theta^{co})^2 & -\left(\frac{\partial R}{\partial \rho} \frac{\partial R}{\partial \theta} + \frac{\partial Z}{\partial \rho} \frac{\partial Z}{\partial \theta} \right) & 0 \\ -\left(\frac{\partial R}{\partial \rho} \frac{\partial R}{\partial \theta} + \frac{\partial Z}{\partial \rho} \frac{\partial Z}{\partial \theta} \right) & (h_\rho^{co})^2 & 0 \\ 0 & 0 & \frac{\mathcal{H}^2}{R^2} \end{pmatrix}
\end{aligned} \tag{3.23}$$

Where the Jacobian determinant \mathcal{J} , referred to in this analysis as the Jacobian, is given by:

$$\mathcal{J} = \left(\vec{e}_\rho \times \vec{e}_\theta \right) \cdot \vec{e}_\phi = \sqrt{|\vec{G}^{co}|} = R\mathcal{H} = R \left(\frac{\partial R}{\partial \rho} \frac{\partial Z}{\partial \theta} - \frac{\partial Z}{\partial \rho} \frac{\partial R}{\partial \theta} \right) > 0 \tag{3.24}$$

The Jacobian can be physically understood as the scale factor used to relate the volume element to the product of differential changes curvilinear variables, $(d\rho d\theta d\phi)$. It can be calculated by the scalar triple product of the basis vectors in all coordinate directions, which is equivalent to taking the square root of the determinant of the covariant metric tensor [Eq. (3.22)].

The contravariant metric tensor can be used to calculate the contravariant basis vectors $(\vec{e}_{\text{con}}^k = g_{\text{con}}^{k,l} \vec{e}_l^{\text{co}})$, which have units of inverse distance.

$$\begin{aligned}
\vec{e}_{\text{con}}^{\rightarrow\rho} &= g_{\text{con}}^{\rho,\rho} \vec{e}_\rho + g_{\text{con}}^{\rho,\theta} \vec{e}_\theta = \frac{1}{\mathcal{H}} \left(\frac{\partial Z}{\partial \theta} \hat{e}_R - \frac{\partial R}{\partial \theta} \hat{e}_Z \right) \\
\vec{e}_{\text{con}}^{\rightarrow\theta} &= g_{\text{con}}^{\theta,\rho} \vec{e}_\rho + g_{\text{con}}^{\theta,\theta} \vec{e}_\theta = \frac{1}{\mathcal{H}} \left(-\frac{\partial Z}{\partial \rho} \hat{e}_R + \frac{\partial R}{\partial \rho} \hat{e}_Z \right) \\
\vec{e}_{\text{con}}^{\rightarrow\phi} &= g_{\text{con}}^{\phi,\phi} \vec{e}_\phi = \frac{1}{R} \hat{e}_\phi
\end{aligned} \tag{3.25}$$

The contravariant scale factors are the inverse of the normalization constants for these contravariant basis vectors.

$$\frac{1}{h_{\text{con}}^\rho} = \left| \vec{e}_{\text{con}}^{\rightarrow\rho} \right| = \frac{h_\theta^{\text{co}}}{\mathcal{H}}, \quad \frac{1}{h_{\text{con}}^\theta} = \left| \vec{e}_{\text{con}}^{\rightarrow\theta} \right| = \frac{h_\rho^{\text{co}}}{\mathcal{H}}, \quad \frac{1}{h_{\text{con}}^\phi} = \left| \vec{e}_{\text{con}}^{\rightarrow\phi} \right| = \frac{1}{R} \tag{3.26}$$

This relationship between scale factors and basis vectors is opposite from covariant forms, where the covariant scale factors are the normalization constants for the covariant basis vectors, instead of their inverses. The contravariant unit vectors can be calculated

$$\text{by } \hat{e}_{\text{con}}^k = h_{\text{con}}^k \vec{e}_{\text{con}}^{\rightarrow k}.$$

This GFA system is not orthogonal in the plane described by the \vec{e}_ρ^{co} and $\vec{e}_\theta^{\text{co}}$ basis vectors, as indicated by the off-diagonal terms in the metric tensors [Eq. (3.22)-(3.23)]. The covariant basis vectors form a parallelogram-shaped differential area element, with area $\mathcal{H}d\rho d\theta$. The contravariant directions are perpendicular to each of the corresponding covariant directions, a property which will make the contravariant directions useful in defining orthogonal sets of coordinate axes.

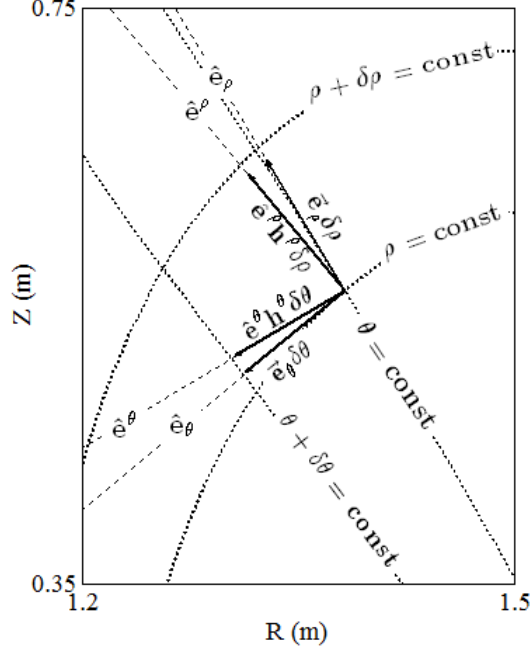


Figure 7: Radial and Poloidal GFA covariant unit vectors (\hat{e}_ζ), scaled covariant basis vector ($\vec{e}_\zeta d\zeta$), contravariant unit vectors (\hat{e}^ζ), and vectors in contravariant directions scaled by contravariant scale factors ($\hat{e}^\zeta h^\zeta d\zeta$) at flux-surface location (ρ, θ) .

The differential length and volume elements in the coordinate directions relate to differential changes in the coordinate variables via the scale factors. The products of the basis vectors from Eq. (3.18) and the differential changes in curvilinear variables yield the differential length elements for general geometry.

$$d\vec{l}_\rho = \frac{\partial \vec{s}}{\partial \rho} d\rho = h_\rho^{co} d\rho \hat{e}_\rho, \quad d\vec{l}_\theta = \frac{\partial \vec{s}}{\partial \theta} d\theta = h_\theta^{co} d\theta \hat{e}_\theta, \quad d\vec{l}_\phi = \frac{\partial \vec{s}}{\partial \phi} d\phi = h_\phi^{co} d\phi \hat{e}_\phi \quad (3.27)$$

An alternative representation of the radial differential length element uses the differential change in the magnetic flux parameter ($d\psi$), instead of the differential change in normalized radius ($d\rho$).

$$d\vec{l}_\rho = \frac{\partial \vec{s}}{\partial \psi} d\psi = \frac{\partial \vec{s}}{\partial \rho} \left(\frac{\partial \psi}{\partial \rho} \right)^{-1} d\psi = \frac{d\vec{l}_\rho}{d\rho} \left(\frac{\partial \psi}{\partial \rho} \right)^{-1} d\psi \quad (3.28)$$

The two representations can be related: $d\vec{l} = h_\rho \left(\frac{\partial \psi}{\partial \rho} \right)^{-1} d\psi \hat{e}_\rho = h_\psi d\psi \hat{e}_\rho = h_\rho d\rho \hat{e}_\rho$

The differential volume element (dV) is the scalar triple product of the differential lengths [Eq. (3.27)] in all covariant coordinate directions. The differential volume element scales with the magnitude of the Jacobian [Eq. (3.24)].

$$dV = d\vec{A}_{\rho\theta} \cdot d\vec{l}_\phi = \left(\vec{e}_\rho \times \vec{e}_\theta \right) \cdot \vec{e}_\phi d\rho d\theta d\phi = \mathcal{H} h_\phi d\rho d\theta d\phi = \mathcal{J} d\rho d\theta d\phi \quad (3.29)$$

This *General Flux-surface Aligned* (GFA) system is semi-orthogonal; the toroidal basis vector is orthogonal to both the poloidal and radial basis vectors, and the poloidal basis vector aligns with flux surfaces. When integrated over the full range of poloidal and toroidal angles for a tokamak, the differential volume element in this general system returns the differential volume of an entire flux surface. Although the toroidal and poloidal basis vectors are parallel to the toroidal and poloidal components of the magnetic field, the radial basis vector is not perpendicular to flux surfaces. This prevents Eq. (3.15) from being used to relate the poloidal component of the magnetic field to the radial gradients of the flux function via these GFA scale factors, without first correcting the direction of the radial basis vector to develop an OFA coordinate system.

3.4. Orthogonalized Flux-surface Aligned (OFA) coordinate system

Because the radial basis vector for General Flux-surface Aligned (GFA) coordinates described in Section 3.3 is not constrained to be normal to flux surfaces, it cannot be directly used to calculate the magnetic field via the relations derived in Section 3.2. However, this general system can be “orthogonalized” so that it retains the flux-surface alignment, but has a covariant radial basis vector directed perpendicular to the flux-surfaces within the poloidal (ρ, θ) plane. This method of determining coordinate axes will be referred to as *Orthogonalized Flux-surface Aligned* (OFA) coordinates and, as indicated by Eq. (3.15), the magnitude and direction of the poloidal component of the magnetic field can be directly related to the radial scale factor and unit-vectors of this system.

The OFA poloidal and toroidal covariant basis vectors are identical to those from the GFA system, and the OFA covariant basis vector (\vec{e}_ρ^\perp) is the GFA contravariant radial unit vector (\hat{e}^ρ) scaled by the GFA contravariant radial scale factor (h^ρ).

$$\begin{aligned}
\vec{e}_\rho^\perp &= h_{con}^\rho \hat{e}_{con}^\rho = h_\rho^\perp \hat{e}_\rho^\perp \\
\vec{e}_\theta^\perp &= e_\theta \\
\vec{e}_\phi^\perp &= e_\phi
\end{aligned} \tag{3.30}$$

Using Eqs. (3.25)-(3.26) the orthogonalized contravariant radial basis vector, unit vector, and scale factor can be represented in terms of gradients of R and Z .

$$\begin{aligned}
\vec{e}_\rho^\perp &= \frac{\mathcal{H}}{h_\theta^2} \left(\frac{\partial Z}{\partial \theta} \hat{e}_R - \frac{\partial R}{\partial \theta} \hat{e}_Z \right) \\
\hat{e}_\rho^\perp &= \frac{1}{h_\theta} \left(\frac{\partial Z}{\partial \theta} \hat{e}_R - \frac{\partial R}{\partial \theta} \hat{e}_Z \right) \\
h_\rho^\perp &= \frac{\mathcal{H}}{h_\theta} = \left(\frac{\partial R}{\partial \rho} \frac{\partial Z}{\partial \theta} - \frac{\partial Z}{\partial \rho} \frac{\partial R}{\partial \theta} \right) \left(\left(\frac{\partial R}{\partial \theta} \right)^2 + \left(\frac{\partial Z}{\partial \theta} \right)^2 \right)^{-1/2}
\end{aligned} \tag{3.31}$$

The elements of the OFA covariant metric tensor can be calculated by $g_{k,l}^\perp = \vec{e}_k^\perp \cdot \vec{e}_l^\perp$,

$$\vec{G}^\perp = \begin{pmatrix} g_{\rho,\rho}^\perp & 0 & 0 \\ 0 & g_{\theta,\theta}^\perp & 0 \\ 0 & 0 & g_{\phi,\phi}^\perp \end{pmatrix} = \begin{pmatrix} h_\rho^{\perp 2} & 0 & 0 \\ 0 & h_\theta^{\perp 2} & 0 \\ 0 & 0 & h_\phi^{\perp 2} \end{pmatrix} = \begin{pmatrix} \frac{\mathcal{H}^2}{h_\theta^2} & 0 & 0 \\ 0 & h_\theta^2 & 0 \\ 0 & 0 & R^2 \end{pmatrix} \tag{3.32}$$

and the contravariant metric tensor can be determined from the inverse of Eq. (3.32)

$$\vec{G}_\perp = \left(\vec{G}^\perp \right)^{-1}$$

$$\vec{G}_\perp = \left(\vec{G}^\perp \right)^{-1} = \frac{1}{\mathcal{J}^2} \begin{pmatrix} g_{\theta,\theta}^\perp g_{\phi,\phi}^\perp & 0 & 0 \\ 0 & g_{\rho,\rho}^\perp g_{\phi,\phi}^\perp & 0 \\ 0 & 0 & g_{\rho,\rho}^\perp g_{\theta,\theta}^\perp \end{pmatrix} \tag{3.33}$$

The Jacobians in both the orthogonalized and general coordinate systems are equivalent.

$$\mathcal{J}^\perp = h_{\rho,\rho}^\perp h_{\theta,\theta}^\perp h_{\phi,\phi}^\perp = \mathcal{J} \tag{3.34}$$

The lack of off-diagonal elements in Eqs. (3.32)-(3.33) indicates that these coordinate axes are orthogonal. Because they are identical, the poloidal and toroidal scale

factors for the OFA system will be represented using the general notation in the remainder of this analysis for simplicity ($h_\theta^\perp \rightarrow h_\theta, h_\phi^\perp \rightarrow h_\phi$).

When plotted against the GFA covariant basis vectors, it becomes clear how the OFA coordinate axes always remain orthogonal, with the OFA covariant basis vectors always perpendicular to the flux-surfaces [solid vectors, Figure 8]. In contrast, the GFA radial basis vectors are oriented in the direction of increasing ρ , while θ remains unchanged; for the CS system, this leads to GFA basis vectors directed away from the plasma center, instead of perpendicular to flux-surfaces [dashed vectors, Figure 8].

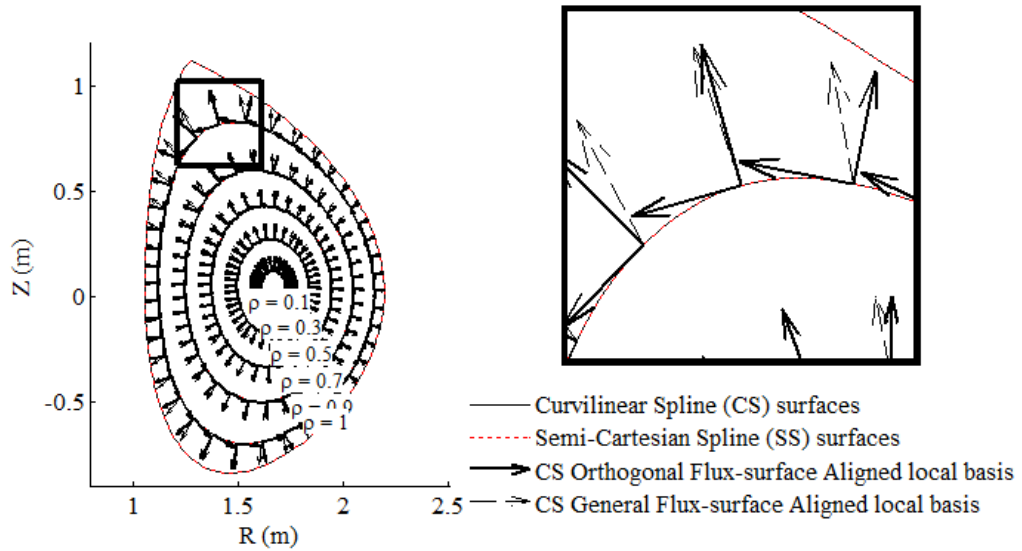


Figure 8: Coordinate axes of the General Flux-surface Aligned (GFA) and Orthogonalized Flux-surface Aligned (OFA) local basis, determined by a Curvilinear Spline (CS) fitting method [Section 4.1]. Figure on right is an expanded view of the inset, showing coordinate axes orientations from the divertor region in greater detail.

The OFA scale factors can be used in the expression for the magnitude of the poloidal magnetic field in Eq. (3.15) to represent the poloidal component of the magnetic field in terms of the gradient of the flux function in the curvilinear coordinate system

$$\left(\frac{\partial\psi}{\partial\rho}\right).$$

$$B_\theta = \frac{1}{h_\phi h_\rho^\perp} \frac{\partial\psi}{\partial\rho} \hat{e}_\rho^\perp = \frac{h_\theta}{h_\phi \mathcal{H}} \frac{\partial\psi}{\partial\rho} \hat{e}_\rho^\perp \quad (3.35)$$

3.5. Calculation of parameters dependent on magnetic field configuration

The plasma safety factor, flux-surface averages of general plasma quantities, and the plasma gyrofrequency are dependent on the magnetic field, and are consequently influenced by the curvilinear coordinate system.

Flux surfaces are defined so that the magnetic fields and differential lengths are related by [12]:

$$\frac{dl_\phi}{dl_\theta} = \frac{B_\phi}{B_\theta} \quad (3.36)$$

The plasma safety factor is defined as the ratio of change in toroidal angle to poloidal angle for the magnetic field lines on a flux surface. A relationship between differential changes in angles can be obtained by writing the differential lengths in Eq. (3.36) in terms of differential angles using Eq. (3.27).

$$d\phi = \frac{B_\phi}{B_\theta} \frac{h_\theta}{h_\phi} d\theta \quad (3.37)$$

The flux-surface value of the safety factor can be obtained by integrating Eq. (3.37) over all poloidal angles to obtain the corresponding change in toroidal angle, and dividing the result by 2π , the equivalent change in poloidal angle. The result describes the number of times that a particle on a flux surface orbits toroidally before completing one full poloidal rotation.

$$q[\rho] = \frac{1}{2\pi} \int_0^{2\pi} \frac{B_\phi}{B_\theta} \frac{h_\theta}{h_\phi} d\theta \quad (3.38)$$

For circular coordinate system geometric coefficients, Eq. (3.38) reduces to the expression for the safety factor given by Stacey [4]. If the poloidal dependence of B_θ and B_ϕ are expanded using Eq. (3.17) and the OFA scale factors, the safety factor expression becomes

$$q[\rho] = \frac{1}{2\pi} \frac{\bar{B}_\phi}{\bar{B}_\theta} \left(\frac{\partial r_0}{\partial \rho} \right)^{-1} \int_0^{2\pi} \frac{\mathcal{H}}{h_\phi} d\theta \quad (3.39)$$

The flux-surface safety-factor expression Eq. (3.39) is a measure of the stability of the plasma force-balance equilibrium; the plasma on flux surfaces with rational values of q is unstable, and prone to magnetic-island formation. The safety factor tends towards one as $\rho \rightarrow 0$. This analysis considers only plasma on flux surfaces with $q < 2$, within the unstable $q=2$ rational-surface region, and corresponding to $\rho \leq 0.7$.

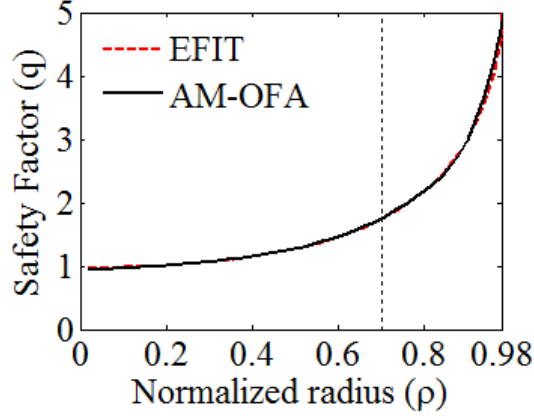


Figure 9: Safety factors calculated by EFIT (red dash) and those calculated using an Asymmetric Miller (AM) model [Section 4.4] to set scale factors and fields for Eq. (3.38) (black).

The total volume of the region with thickness dl_ψ between flux surfaces with flux-functions ψ and $\psi + d\psi$ can be expressed in terms of a poloidal integral and the differential change in ρ . This volume can be normalized by the change in poloidal magnetic flux parameter $\delta\psi$, or the change in the normalized radius $\delta\rho$.

$$\begin{aligned}
\mathbb{V}_\psi &= \frac{1}{\delta\psi} \int_\psi^{\psi+\delta\psi} \oint_\theta \oint_\phi dV = \frac{1}{\delta\psi} \oint_\theta \oint_\phi dl_\psi dl_\theta dl_\phi = \frac{1}{\delta\psi} \left(\frac{\partial\psi}{\partial\rho} \right)^{-1} \oint_\theta \oint_\phi h_\rho h_\theta h_\phi d\theta d\phi \delta\psi \\
&= 2\pi \left(\frac{\partial\psi}{\partial\rho} \right)^{-1} \oint_\theta \mathcal{J} d\theta \\
\mathbb{V}_\rho &= 2\pi \oint_\theta \mathcal{J} d\theta
\end{aligned} \tag{3.40}$$

The expression for \mathbb{V}_ψ can be used in the definition of the flux-surface averaging (FSA) operator, notated using angle-brackets ($\langle \dots \rangle$). The FSA of a poloidally-dependent quantity \mathcal{C} represents the average of this quantity over the volume element ($\mathbb{V}_\psi \delta\psi$), and can be expressed in toroidally axisymmetric geometry as:

$$\begin{aligned}
\langle C \rangle &= \frac{\int_{\psi}^{\psi+\delta\psi} \oint_{\theta} \oint_{\phi} C \, d\mathbf{V}}{\int_{\psi}^{\psi+\delta\psi} \oint_{\theta} \oint_{\phi} d\mathbf{V}} = \frac{2\pi}{\mathbb{V}_{\psi\theta}} \oint_{\theta} C h_{\psi} h_{\phi} h_{\theta} d\theta = \frac{2\pi}{\mathbb{V}_{\psi}} \left(\frac{\partial \psi}{\partial \rho} \right)^{-1} \oint_{\theta} C \mathcal{J} d\theta \\
&= \frac{2\pi}{\mathbb{V}_{\psi\theta}} \oint_{\theta} C \frac{dl_{\theta}}{|B_{\theta}|}
\end{aligned} \tag{3.41}$$

The gyrofrequency Ω_i for species i describes the frequency at which particles spiral about magnetic field lines, and is generally defined as $\Omega_i = \frac{e_i}{m_i} \left| \vec{B} \right|$ [6]. Under the assumption that $|B_{\phi}^2| \gg |B_{\theta}^2|$, the general definition for the gyrofrequency in terms of the total magnetic field strength simplifies to

$$\Omega_i[\rho, \theta] = \frac{e_i}{m_i} \left| \vec{B} \right| = \frac{e_i}{m_i} \sqrt{|B_{\phi}|^2 + |B_{\theta}|^2} \simeq \frac{e_i |\vec{B}_{\phi}|}{m_i} \frac{R_0}{h_{\phi}} \tag{3.42}$$

CHAPTER 4

ANALYTIC MODELS FOR REPRESENTING FLUX-SURFACES

In order to apply the formalism developed in the previous section to calculate geometric coefficients and formulate vector operations in *Orthogonal Flux-surface Aligned* (OFA) curvilinear systems, it is necessary to be able to calculate gradients of the flux-surface location vector Eq. (3.10) with respect to the curvilinear variables (ρ, θ, ϕ) . In addition to a method of approximating these gradients from EFIT-determined ψ distributions using spline fits of the tabulated spatial (ρ, θ) variations of R and Z for flux surface contours (CS fitting method), analytic models of $R[\rho, \theta]$ and $Z[\rho, \theta]$ in terms of radially-dependent fitting coefficients and trigonometric functions of θ can be used to develop simple analytic expressions for these gradients. These analytical methods include a Flux-surface conserving “Circular” model (FC), two models that represent flux surfaces in terms of Fourier expansions (DF and SF), and both symmetric and asymmetric variations of the “Miller” model (SM and AM).

The following sections use Semi-Cartesian Spline (SS) calculations of flux surfaces and poloidal magnetic fields and an OFA coordinate system determined by a Curvilinear Spline (CS) method as a basis for comparing the flux surfaces and poloidal magnetic fields calculated using OFA coordinate systems based on representations of $R[\rho, \theta]$ and $Z[\rho, \theta]$ gradients in variations of the Circular, Fourier expanded, and Miller coordinate systems.

4.1. Curvilinear Spline (CS) fitting method for comparison of flux-surface fitting models

The most accurate method of representing the gradients of R and Z with respect to curvilinear variables ρ and θ is to use the gradients of radial and poloidal spline fits through all available R and Z flux surface locations interpolated from the EFIT ψ distribution. This method will be referred to as the *Curvilinear Spline* (CS) fitting method, and allows for calculations of both the OFA and GFA sets of scale factors and

the poloidal magnetic field distribution from Eq. (3.35). While the SS and CS flux surface locations are identical, the poloidal field distribution calculated using the SS model differs from the field distribution computed using the simpler and more accurate SS method [Eq. (3.14)]. Consequently, a complete plasma geometry described by the shared spline-fit interpolation of flux surfaces, the CS basis vectors, and the SS poloidal magnetic field distribution will be used as a basis for comparing equivalent plasma geometries obtained using the simpler fitting models.

4.1.1. Using Spline fits to relate EFIT flux surfaces and OFA basis vectors to curvilinear variables ρ and θ

Any location within the plasma has associated values for R, Z, ρ and θ , which can all be related to each other in the semi-Cartesian representation of the Grad-Shafranov equilibrium (ψ) distribution by using 2D spline-interpolation to find flux-surfaces of constant ψ [Figure 5]. From the results of this 2D spline interpolation, two separate distributions of $R[\rho, \theta]$ and $Z[\rho, \theta]$ can be determined from the single original $\psi[R, Z]$ distribution. Figure 10 shows these two distributions using 200 poloidal locations to represent each of 50 radial flux surfaces.

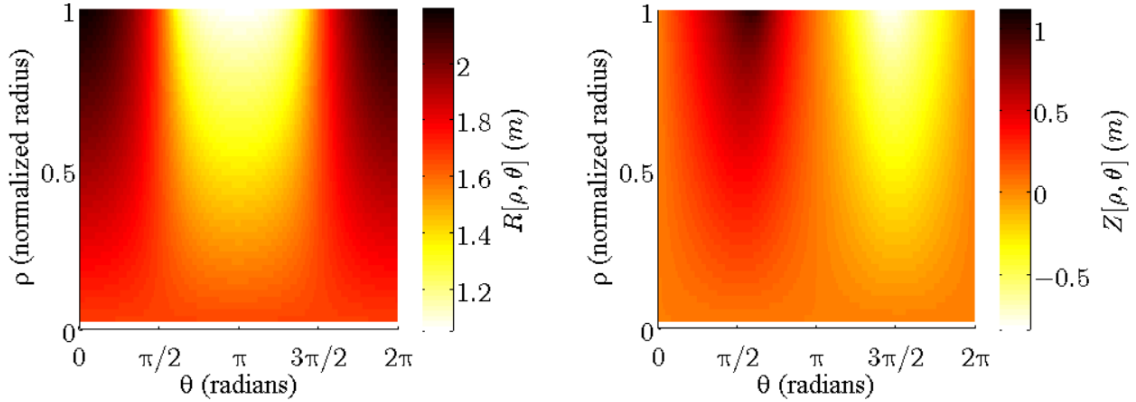


Figure 10: Distributions of major radius $R[\rho, \theta]$ (left) and vertical position $Z[\rho, \theta]$ (right) relative to the flux-surface curvilinear coordinates (ρ, θ) .

Calculating the distributions R and Z [Figure 10] directly from EFIT is the most accurate method, and the “positional” error in the flux surface representations of all other fitting methods can be determined by how much they differ from these distributions. A metric of a model’s positional error in representing a flux surface can be calculated by

$$\mathcal{E}_{position}[\rho, \theta] = \frac{|r[\rho, \theta] - r_{ss}[\rho, \theta]|}{\langle r_{ss}[\rho, \theta] \rangle} \quad (4.1)$$

where $r_{ss} = \sqrt{R^2 + Z^2}$ is calculated using the spline-interpolated distributions shown in Figure 10. The flux surface average of Eq. (4.1) is a measure of the accuracy of the curvilinear model at matching the flux-surface shape and position determined directly from ψ contours. However, because this metric depends only on minor radius, this positional error does not account for differences in the major radius R_0 between models [Figure 3].

A curvilinear model is necessary to evaluate the FSA of the denominator of Eq. (4.1), which requires that gradients $\left(\frac{\partial R}{\partial \rho}, \frac{\partial R}{\partial \theta}, \frac{\partial Z}{\partial \rho}, \frac{\partial Z}{\partial \theta}\right)$ be calculated and used to evaluate the curvilinear formalism of Section 3.4. Spline fits of the two distributions shown in Figure 10 with respect to both ρ and θ curvilinear variables can be used to determine these four gradients, which are then used to calculate covariant basis vectors [Eq. (3.18), Figure 8], scale factors [Eq. (3.20)], and evaluate all of the remaining GFA and OFA formalism discussed in the previous section. This method of determining the OFA basis vectors and scale factors will be referred to as a *Curvilinear Spline* (CS) method, and shares the same flux-surface locations used to map the SS calculations of poloidal magnetic field to the plasma. As a consequence of this, positional error [Eq. (4.1)] for the CS model is always zero.

4.1.2. Curvilinear poloidal magnetic field error

The scale factors calculated from the CS fits can be used to calculate the poloidal magnetic field distribution from Eq. (3.35). This calculation of the poloidal magnetic field is mathematically equivalent to the field calculated using Eq. (3.14), but performed in curvilinear coordinates instead of Semi-Cartesian coordinates. However, there are differences between the two B_θ distributions, due to error introduced by the spline-fitting methods used to determine gradients in both the Semi-Cartesian (SS) and Curvilinear (CS) systems [Figure 11]; this error can be quantified by a metric referred to as the “field error”.

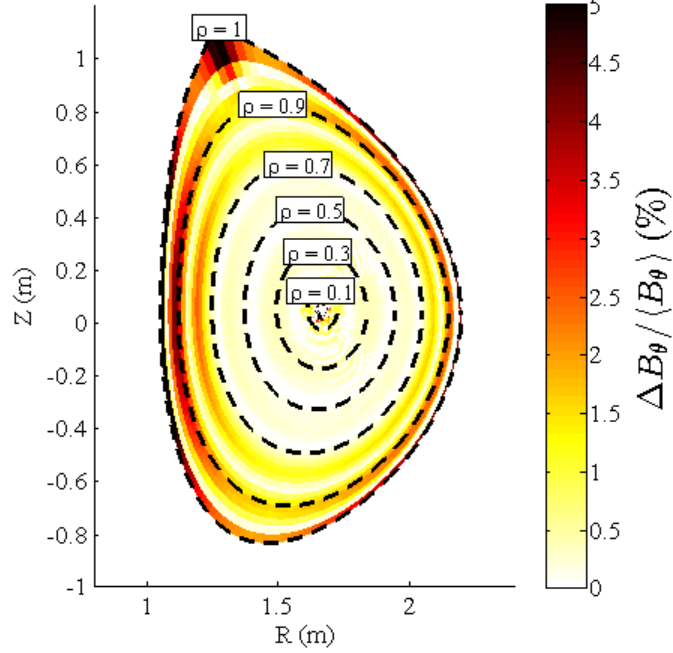


Figure 11: The field error \mathcal{E}_{field} between CS and SS predictions of B_θ , normalized by flux-surface constant values of Semi-Cartesian Spline (SS) $\langle B_\theta \rangle$, calculated by applying the FSA operation [Eq. (3.41)] to a field calculated using Eq. (3.14).

Because the SS calculation [Eq. (3.14)] involves the least complex spline fits, its poloidal magnetic field distribution will be used as a reference from which the errors of all other models can be calculated. Consequently, the field error and its flux surface average can be calculated by:

$$\mathcal{E}_{field} = \frac{|B_\theta - B_\theta^{SS}|}{\langle B_\theta^{SS} \rangle} \quad (4.2)$$

$$\langle \mathcal{E}_{field} \rangle = \frac{\langle |B_\theta - B_\theta^{SS}| \rangle}{\langle B_\theta^{SS} \rangle}$$

where B_θ^{SS} is the poloidal magnetic field calculated by using Eq. (3.14), and CS-OFA flux surfaces and scale factors are used to perform the FSA operation over the denominator. Because representing the poloidal magnetic field correctly is essential to calculations of the viscous and electromagnetic terms of the momentum balance equations, the field error of Eq.(4.2) is directly related to the ability of a curvilinear model to be used to accurately formulate the plasma equations.

Averages of the field error over poloidal and radial sectors of the plasma can be used to summarize the local variations in poloidal magnetic field in a more condensed form than full 2D topological error distributions. In addition using the full flux-surface average, field errors can be defined over poloidal sectors of the plasma; considering the single-null upper divertor configuration of shot 149468, the partial FSA of errors over the lower plasma hemisphere ($\langle \mathcal{E}_{field}^{low} \rangle$) and the left and right portions of the upper plasma hemisphere ($\langle \mathcal{E}_{field}^{upL} \rangle$ and $\langle \mathcal{E}_{field}^{upR} \rangle$) will be considered separately in this analysis [Figure 12].

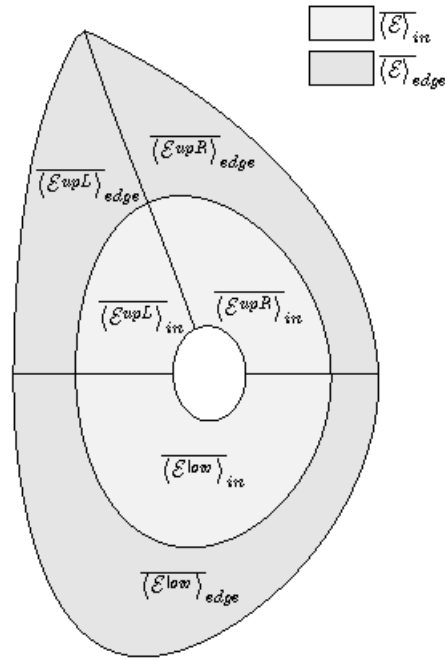


Figure 12: Plasma sectors for error calculations. Upper right (upR), upper left (upL), and lower (low) regions. Inner and edge regions are separated by the $q=2$, $\rho \cong 0.7$ flux surface.

The poloidal angle of the divertor (108°) will be used to separate the upper left and right errors; $\langle \mathcal{E}_{field}^{upR} \rangle$ is defined from ($0 < \theta < 108^\circ$), $\langle \mathcal{E}_{field}^{upL} \rangle$ over ($108^\circ < \theta < 180^\circ$), and $\langle \mathcal{E}_{field}^{low} \rangle$ from ($180^\circ < \theta < 360^\circ$). In order to represent the field error localized to the plasma edge, $\langle \mathcal{E}_{field} \rangle_{edge}$ will be defined as the radial average of the flux-surface averages of errors outside of the $q = 2$ flux surface ($0.7 < \rho < 1$). A metric of the error over the inner plasma region ($\langle \mathcal{E}_{field} \rangle_{in}$) will be defined by the radial average of

error over $0.2 < \rho < 0.7$. Because the value of B_θ in the denominator of Eq.(4.2) trends towards zero as $\rho \rightarrow 0$, field error calculations over the small region of plasma with $\rho < 0.2$ becomes unreliable (central region of Figure 11), which is why this portion of the plasma is excluded from the calculation of inner plasma field error $\left(\overline{\langle \mathcal{E}_{field} \rangle_{in}}\right)$.

Table 1: Curvilinear Spline (CS) model field errors [Eq. (4.2)] (%) in three inner plasma sectors (left columns), and averaged over the full inner and edge plasma regions [Figure 12]

Model Type	Upper Hemisphere		Lower Hemisphere	$\overline{\langle \mathcal{E}_{field} \rangle_{in}}$	$\overline{\langle \mathcal{E}_{field} \rangle_{edge}}$
	Inner Error (%)		Inner Error (%)		
	$\overline{\langle \mathcal{E}_{field}^{upR} \rangle_{in}}$	$\overline{\langle \mathcal{E}_{field}^{upL} \rangle_{in}}$	$\overline{\langle \mathcal{E}_{field}^{low} \rangle_{in}}$		
Curvilinear Spline (CS)	0.224	0.207	0.215	0.22	1.75

The field error for the CS plasma fit is generally less than 1%, although it increases to around 5% at a few points near the LCFS [Figure 11].

4.1.3. General flux-surface fitting techniques

All models considered in this analysis, including the CS model, depend on radially-dependent fitting parameters that can be adjusted in order to approximate the positions and locations of flux-surfaces. The most common of these are the major radius (R_0) and the minor radius (r_0), which are both present in all but one version of Fourier fitting model. In the circular model, R_0 can be approximated as a constant for all flux surfaces. In simple circular models and variations of the Miller model, the minor radius r_0 is modeled as linearly dependent on ρ . In the case of the CS model, all 200 interpolated values for R and Z on each flux surface shown in Figure 10 are used, making this by far the most complex model considered in this analysis.

The most effective way of determining the radial dependence of all other fitting parameters which minimizes positional error is usually through a linear least-squares fit of the minor radius of the model being considered to the minor radius determined by spline-interpolated R and Z distributions [Figure 10], with the fitting parameters as degrees of freedom. In this analysis, only models with up to ten fitting coefficients per

flux surface are considered, in order to compare the accuracy of models with approximately equivalent complexity.

The fitting processes yields flux-surface dependent values for each fitting parameter, which often show irregularities near the extreme center and edge of the plasma, around $\rho = 0$ and $\rho = 1$. In order to smooth these fits and develop a purely analytic representation for the flux surface positions with respect to the curvilinear variables ρ and θ , a second least-squares routine is applied to the radial profiles of fitting coefficients to determine a piecewise polynomial fit of the radial dependence. Separate radially dependent polynomial fits are used to represent the radial dependence of fitting coefficients for flux surfaces on various sides of the $q=2$ ($\rho \cong 0.7$) flux-surface, although these polynomial fits are constrained so that the full profile and gradients are continuous across this surface. The analytic representations for the radial gradients of these polynomials will used to develop analytic expressions for the curvilinear gradients of R and Z in some models.

4.2. Circular Model for General and Orthogonalized Flux-surface Aligned Coordinates (C-GFA and C-OFA)

The radial and poloidal variations in R and Z can be simply represented in terms of ρ and θ using a “circular” model for the poloidal variations in plasma shape. This type of method represents the position vector $\vec{s}[\rho, \theta]$ analytically using a central major radius (R_0) and a radially dependent minor radius (r_0) for each flux-surface, along with trigonometric functions of the poloidal angle θ . The minor radius can be modeled as increasing linearly with ρ to an outer flux-surface with surface area approximately equivalent to the surface area of an elliptical torus with elongation determined from the EFIT LCFS (*Edge flux-equivalent Circular* (EC) model), or the elongations for all fitted EFIT flux surfaces can be used to set the radial dependence of the minor radius so that all circular model flux-surfaces have areas approximately equivalent to the corresponding EFIT surfaces (*Flux-equivalent Circular* (FC) model). The gradients of the analytic expressions for the position vector can be used to determine basis vectors and scale factors for the GFA circular coordinate system, and show that this coordinate system is naturally orthogonal due to the lack of radial dependence in R_0 . The errors in the

corresponding poloidal magnetic field distributions are used to compare the ability of the more accurate *Flux-equivalent Circular* (FC) model to represent the plasma against the very low errors attainable using the much more complex Curvilinear Spline (CS) method for representing the EFIT plasma geometry.

The components of the circular model position vector Eq. (3.10) relative to the tokamak absolute origin in terms of R_0 and r_0 are

$$\begin{aligned} R[\rho, \theta] &= R_0 + r_0[\rho] \cos \theta \\ Z[\rho, \theta] &= r_0[\rho] \sin \theta \end{aligned} \quad (4.3)$$

Where $r_0[\rho]$ describes the minor radii of the circular tori representing flux surfaces. For the circular model, the central major radius R_0 is set by the distance from the tokamak central axis to the central point between the LCFS on the inboard and outboard midplanes, and is constant for all flux surfaces throughout the plasma. The EFIT determined value of major radius is $R_0 = 1.623 \text{ m}$.

A circular model geometry can be constructed with a linearly increasing minor radius, so that the surface areas of the outer flux surface ($\mathbb{S} = 4\pi^2 r_0 R_0$) is approximately equivalent to the areas of the LCFS for an elliptical tori with an elongation κ and minor radii $a\rho$ determined from the EFIT plasma LCFS [14]. The radial dependence of the minor radius r_0 can then be calculated in terms of the fixed plasma elongation κ and the minor radius a :

$$r_0 = a\rho \sqrt{\frac{1}{2}(1 + \kappa^2)} \quad (4.4)$$

The most common variation of this Edge flux-equivalent Circular (EC) model uses an elongation determined by that of the EFIT LCFS, ($\kappa = 1.722$). This elongation is the ratio of the maximum plasma height to the minor radius at the midplane of the LCFS, $a = 0.569$. The effective circular minor radius at the outboard midplane for this *Edge flux-equivalent Circular* (EC) model is $\bar{a} = r_0|_{\rho=1} = 0.801$, and both the minor radius and its gradient can be represented in terms of this effective circular LCFS minor radius as:

$$r_0 = \bar{a}\rho, \quad \frac{\partial r_0}{\partial \rho} = \bar{a} \quad (4.5)$$

If a radially dependent elongation is used to separately conserve surface area for each flux surface, then an expression for the radial gradient of minor radius in this *Flux-equivalent Circular* (FC) system can be determined from Eq. (4.4), with κ modeled as a function of ρ .

$$\frac{\partial r_0}{\partial \rho} = \frac{a}{\sqrt{2(1+\kappa^2)}} \left(1 + \kappa^2 + \rho \kappa \frac{\partial \kappa}{\partial \rho} \right) \quad (4.6)$$

The radial profile of elongation can be determined by averaging the distance from the midplane to the most extreme points in the upper and lower hemispheres for each flux

surface, and normalizing by the corresponding minor radius $\kappa = \frac{\min[Z[\theta]] + \max[Z[\theta]]}{2a}$.

The minor radii at the plasma edge (\bar{a}) for both of these variations of the circular model will be larger than the true plasma minor radius at the OBMP LCFS (a). Because of the averaging process, the FC model has a slightly smaller LCFS minor radius than the EC model, as the elongation used throughout the EC model is the maximum elongation of the EFIT plasma. The EC model's total plasma volume is larger than that of the FC model, and the true EFIT volume is smaller than that of both circular models

($\mathbb{V} = 2\pi^2 r_0^2 R_0$). The plasma effective minor radius (\bar{a}), LCFS surface area (\mathbb{S}), the full plasma volume (\mathbb{V}), the LCFS elongation (κ), and the averaged positional errors over the inner and edge plasma regions are shown in Table 2, comparing the accuracy of the FC and EC models for the upper single-null divertor plasma of Shot# 149468, at 1905ms.

Table 2: FC dimensions and positional errors. $\mathbb{V}_{EFIT} = 15.962$.

Model	\bar{a} (m)	S (m ²)	V (m ³)	κ_{LCFS}	$\overline{\langle \mathcal{E}_{position} \rangle}_{in}$	$\overline{\langle \mathcal{E}_{position} \rangle}_{edge}$
Edge flux-equivalent Circular (EC)	0.801	51.335	20.564	1.722	22.57%	19.80%
Flux-equivalent Circular (FC)	0.776	49.74	19.306	1.648	9.32%	13.07%

Interestingly, the positional error $\langle \mathcal{E}_{position} \rangle$ actually decreases with increasing minor radius for the EC model, while increasing for the FC model. The flux surfaces for the more accurate FC model are shown in Figure 13, illustrating how the error is caused primarily by the circular model's inability to adjust to represent the plasma's up-down asymmetries, which become especially significant towards the outer flux surfaces.

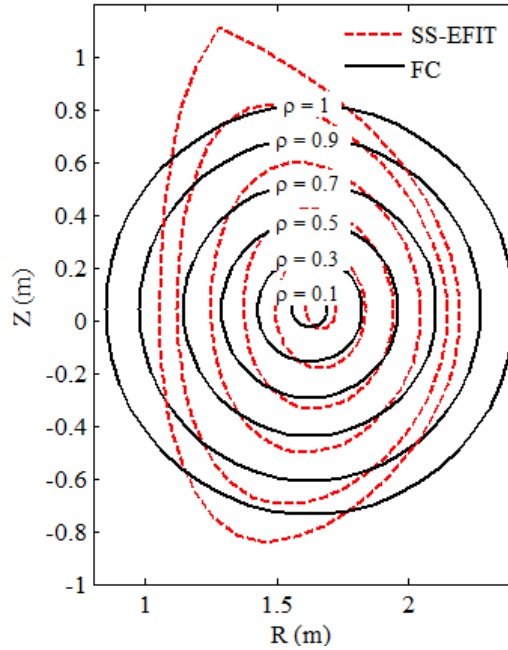


Figure 13: Comparison of EFIT SS/CS flux-surfaces (RED) and Flux-equivalent Circular (FC) predictions of flux-surfaces (BLACK) [Eq. (4.3)], for Shot# 149468, 1905ms.

The dashed EFIT flux surfaces in Figure 13 illustrate the Shafranov shift [15] in the central major radius R_0 towards the outside, which the Circular model is unable to

account for. This discrepancy, particularly noticeable in the offset between the inner EFIT and FC flux surfaces, does not influence the positional error calculations [Eq. (4.1)], which are dependent only on minor radius. Consequently, the positional errors reported in Table 2 slightly underestimate discrepancy between true and circular-model flux surfaces.

By applying Eq. (3.18), the General Flux-surface Aligned (GFA) basis vectors and scale factors can be calculated for the circular model.

$$\begin{aligned} \vec{e}_\rho &= \frac{\partial r_0}{\partial \rho} \cos \theta \hat{e}_R + \frac{\partial r_0}{\partial \rho} \sin \theta \hat{e}_Z \\ \vec{e}_\theta &= -r_0 \sin \theta \hat{e}_R + r_0 \cos \theta \hat{e}_Z \\ \vec{e}_\phi &= (R_0 + r_0 \cos \theta) \hat{e}_\phi \end{aligned} \quad (4.7)$$

$$h_\rho = \frac{\partial r_0}{\partial \rho}, \quad h_\theta = r_0, \quad h_\phi = R_0 + r_0 \cos[\theta] \quad (4.8)$$

Because the major radius is independent of flux surface ($\frac{\partial R_0}{\partial \rho} = 0$), the circular model minor radius and the area scale factor reduce to forms that are independent of poloidal angle.

$$\begin{aligned} r &= \sqrt{(R - R_0)^2 + Z^2} = r_0 \\ \mathcal{H} &= r_0 \frac{\partial r_0}{\partial \rho} \end{aligned} \quad (4.9)$$

Plotting the *Flux-equivalent Circular* set of General Flux-surface Aligned basis vectors (FC-GFA) calculated from Eq. (4.7) and scaled by ($d\rho = 0.1, d\theta = 0.16$) at evenly-spaced poloidal positions on six flux surfaces ranging from the plasma center to edge shows how the orientation of the local curvilinear coordinate axes rotates with poloidal location [Figure 14]. Variations of the circular model are unique among general curvilinear systems because their Orthogonalized Flux-surface Aligned (OFA) basis vectors [Eq. (3.31)] are identical to their General Flux-surface Aligned (FC-GFA) basis vectors. The radial basis vectors change direction so that they are always directed away from the plasma center, which is also perpendicular to the flux-surfaces for the circular formalism.

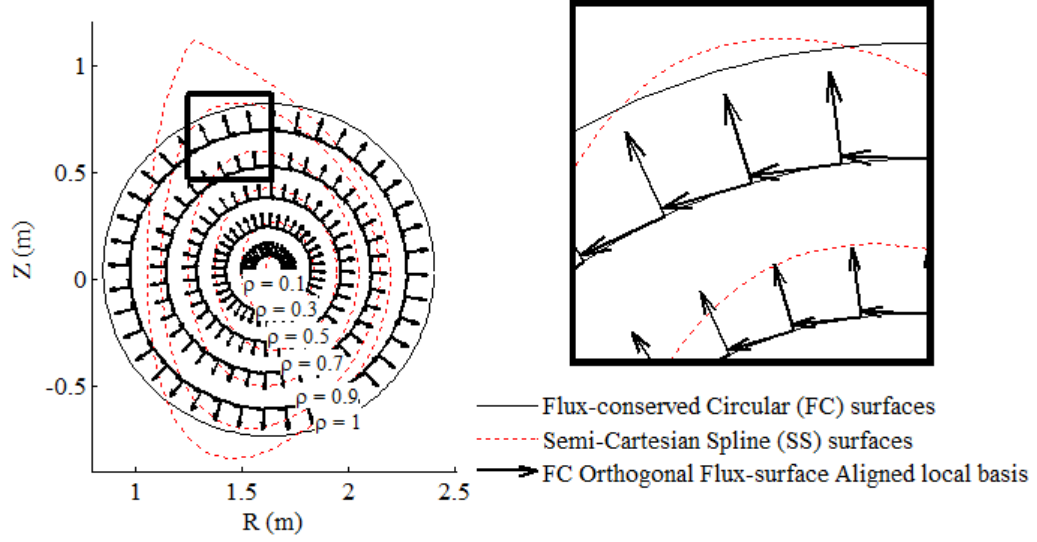


Figure 14: The directions of FC-OFA and FC-GFA basis vectors are identical [Eq. (4.7)]. Magnification of inset shown on right.

Applying the scale factors of Eq. (4.8) to the field definitions from Eq. (3.17), the components of the magnetic field for the circular coordinate system can be written in terms of \bar{B}_θ and \bar{B}_ϕ :

$$\begin{aligned}
 B_\phi &= \frac{\bar{B}_\phi}{1 + \varepsilon \cos \theta} \\
 B_\theta &= \frac{\bar{B}_\theta}{1 + \varepsilon \cos \theta}
 \end{aligned}
 \tag{4.10}$$

where $\left(\varepsilon = \frac{r_0}{R_0} = \frac{\bar{a}\rho}{R_0}\right)$. These are identical to the circular-model expressions for the components of the magnetic field given by Stacey [4].

The effectiveness of the Flux-equivalent Circular (FC) at predicting a poloidal magnetic field distribution can be measured by the average of sector-dependent field-error calculations [Eq. (4.2), Table 3] computed using poloidal fields of the form of Eq. (4.10). The sector-averaged field errors for the Curvilinear Spline model are shown for comparison.

Table 3: Circular model field errors [Eq. (4.2)] (%) in three inner plasma sectors (left columns), and averaged over the full inner and edge plasma regions [Figure 12].

Model Type		Upper Hemisphere		Lower Hemisphere	$\overline{\langle \mathcal{E}_{field} \rangle}_{in}$	$\overline{\langle \mathcal{E}_{field} \rangle}_{edge}$
		Inner Error (%)		Inner Error (%)		
		$\overline{\langle \mathcal{E}_{field}^{upR} \rangle}_{in}$	$\overline{\langle \mathcal{E}_{field}^{upL} \rangle}_{in}$	$\overline{\langle \mathcal{E}_{field}^{low} \rangle}_{in}$		
Spline	CS	0.22	0.21	0.21	0.22	1.75
Circular	EC	26.03	11.57	19.34	20.16	33.57
	FC	18.03	7.35	12.34	13.25	40.13

The errors in the circular model predictions for the poloidal magnetic field distribution are two orders of magnitude greater than the error introduced by developing a curvilinear system by spline-fits of the EFIT data (CS model). Interestingly, while the FC model decreased positional errors throughout the circular model as compared to the EC model, it actually results in a higher field error over the edge region. Plotting the FC model field error distribution shows how the majority of the error is introduced in the outer edge region, with a sharp increase in the region around the upper nulls in the poloidal magnetic field.

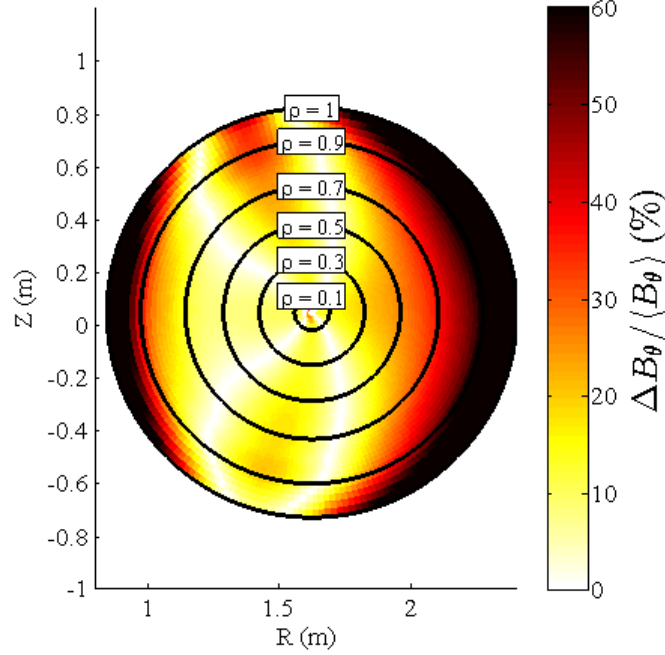


Figure 15: Distribution of poloidal magnetic field error \mathcal{E}_{field} (%) for the FC-OFA model [Eq. (4.2) and (4.8)]

Because the representation of the poloidal magnetic field is essential to correctly formulating both the electromagnetic and the viscous contributions to the momentum balance equations [Eq. (2.6), Appendix A.3], and errors in the scale factors influence the flux-surface averaging operation [Eq. (3.41)], the size of the circular-model field errors are large enough to call into question the ability of this model to set poloidal fields and scale factors in the plasma equations over certain regions of the plasma.

4.3. Single Fourier Expansion model (SF) for minor radius (r)

Using a Fourier expansions to represent the poloidal variations in minor radius corresponding to each flux surface is a robust method of representing arbitrarily high order flux-surface structure, while retaining an analytic model that involves only simple trigonometric basis functions. However, while expanding this *Single Fourier* (SF) model to high enough order does allow for arbitrarily accurate representations of flux-surface shapes, it also requires the use of many more fitting coefficients than the two required for circular models. Applying a fourth order (O(4)) expansion limits this model to ten fitting coefficients per flux-surface, and is the most complex geometry besides the CS model that will be considered in this analysis. The poloidal magnetic field resulting from scale

factors calculated in this O(4) *Single Fourier Orthogonalized Flux-surface Aligned* (SF-OFA) coordinate system can be compared against the CS fields predictions in order to assess the ability of the SF(4) model to represent flux-surfaces and the poloidal magnetic field.

The Cartesian components of the position vector in SF coordinates are identical in form to the circular model representations, but apply a radially dependent central major radius and poloidally dependent minor radius.

$$\begin{aligned} R[\rho, \theta] &= R_0[\rho] + r[\rho, \theta] \cos[\theta] \\ Z[\rho, \theta] &= r[\rho, \theta] \sin[\theta] \end{aligned} \quad (4.11)$$

The minor radius is represented by using a Fourier series expansion of order N (O[N]), with radially dependent sine and cosine expansion coefficients ($r^{s,c}$).

$$\begin{aligned} r[\rho, \theta] &= r_0 \left(1 + \sum_{n=1}^N r^{c,n} \cos n\theta + \sum_{n=1}^N r^{s,n} \sin n\theta \right) \\ &= r_0[\rho] + \hat{r}[\rho, \theta] = r_0 \left(1 + \epsilon \tilde{r} \right) \end{aligned} \quad (4.12)$$

The representation for $r[\rho, \theta]$ in the first piece of Eq. (4.12) can be separated into an average, flux-surface dependent minor radius (r_0) and a smaller $O(\epsilon)$ term (\hat{r}). The expansion coefficients higher than 0th order are typically of order ϵ for a ‘‘D’’ shaped plasma such as the one considered in this analysis, where $\left(\epsilon = \frac{a}{R_0} = 0.3416 < 1 \right)$ is a plasma constant with no radial dependence. Finally, the minor radius r_0 can be factored out of the full expression, and \hat{r} can be rewritten in terms of a poloidally dependent term \tilde{r} which is of order unity. This poloidally-dependent asymmetry term and its gradients are necessary for calculations of the scale factors in this system, and can all be written in terms of the normalized radially dependent Fourier asymmetries $\tilde{r}^{s,c}$.

$$\begin{aligned}
\tilde{r} &= \sum_{n=1}^N (\tilde{r}^{c,n} \cos n\theta + \tilde{r}^{s,n} \sin n\theta) \\
\frac{\partial \tilde{r}}{\partial \theta} &= \sum_{n=1}^N (-\tilde{r}^{c,n} \sin n\theta + \tilde{r}^{s,n} \cos n\theta) \\
\frac{\partial \tilde{r}}{\partial \rho} &= \sum_{n=1}^N \left(\frac{\partial \tilde{r}^{c,n}}{\partial \rho} \cos n\theta + \frac{\partial \tilde{r}^{s,n}}{\partial \rho} \sin n\theta \right)
\end{aligned} \tag{4.13}$$

If $\tilde{r} \rightarrow 0$ and $\frac{\partial R_0}{\partial \rho} \rightarrow 0$ the SF formalism reduces to the circular model.

It is straightforward to apply a least-squares method to constrain the SF model flux surfaces to match as closely as possible with the EFIT surfaces. The SF model is linear with respect to the asymmetries, which are the fitting coefficients for this model. Increasing the expansion from zeroth to 4th order drops the positional error throughout the plasma by about an order of magnitude [Table 4].

Table 4: Positional Errors (%) and number of fitting coefficients per. flux surface of three expansion orders of the Single Fourier (SF) model.

Model	$\frac{N_{coef}}{surface}$	$\langle \mathcal{E}_{position} \rangle_{in}$	$\langle \mathcal{E}_{position} \rangle_{edge}$
Single Fourier O(0) (SF0)	2	8.92	11.59
Single Fourier O(2) (SF2)	6	1.67	4.55
Single Fourier O(4) (SF)	10	0.38	1.61

A 0th order SF expansion fitted using the above technique yields a more advanced variation of the circular model with a non-orthogonal GFA system due to the Shafranov shift, and a minor radius which is not linearly dependent on ρ . These changes further decrease the positional error from the Flux-equivalent Circular (FC) model. The highest order O(4) SF expansion considered here involves ten fitting coefficients ($R_0, r_0, r^{s,1}, r^{c,1}, r^{s,2}, r^{c,2}, r^{s,3}, r^{c,3}, r^{s,4}, r^{c,4}$); while increasing the order to this model does significantly decrease the positional error, flux-surface representations in the edge region does show a ‘‘wavy’’ behavior characteristic of Fourier series fits. This model’s ability to be expanded to arbitrarily high orders may be an advantage if an extremely accurate representation of flux surfaces is necessary enough to justify calculating values for even more fitting coefficients.

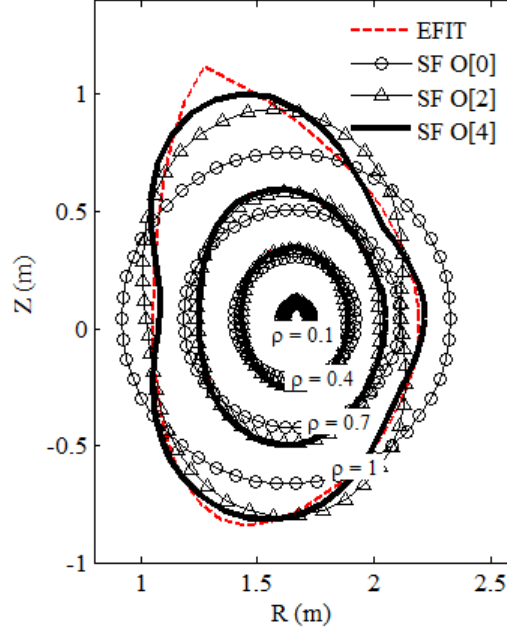


Figure 16: Comparison of the shapes of CS flux surfaces from EFIT (red dashed contours) with three orders of Single Fourier (SF) model flux surfaces (solid bold black contours).

The gradients of the poloidally-dependent components of the position vector given in Eq. (4.11), are necessary for calculation of the SF basis vectors and geometric coefficients. In terms of gradients of the poloidally-dependent minor radius [Eq. (4.12)], these are:

$$\begin{aligned}
 \frac{\partial R}{\partial \rho} &= \frac{\partial R_0}{\partial \rho} + \frac{\partial r}{\partial \rho} \cos[\theta] \\
 \frac{\partial R}{\partial \theta} &= -r \sin[\theta] + \frac{\partial r}{\partial \theta} \cos[\theta] \\
 \frac{\partial Z}{\partial \rho} &= \frac{\partial r}{\partial \rho} \sin[\theta] \\
 \frac{\partial Z}{\partial \theta} &= r \cos[\theta] + \frac{\partial r}{\partial \theta} \sin[\theta]
 \end{aligned} \tag{4.14}$$

where the gradients of the minor radius from Eq. (4.12) can be written in terms of the gradients of r_0 and \tilde{r} shown in Eq. (4.13).

$$\begin{aligned}
 \frac{\partial r}{\partial \rho} &= \frac{\partial r_0}{\partial \rho} \left(1 + \epsilon \tilde{r}\right) + r_0 \epsilon \frac{\partial \tilde{r}}{\partial \rho} \\
 \frac{\partial r}{\partial \theta} &= r_0 \epsilon \frac{\partial \tilde{r}}{\partial \theta}
 \end{aligned} \tag{4.15}$$

After applying the expressions for gradients of R and Z given in Eq. (4.14) to Eq. (3.20) and simplifying, the SF-GFA radial, poloidal, and toroidal scale factors can be expressed in terms of the major and minor radii.

$$\begin{aligned}
 h_\rho &= \sqrt{\left(\frac{\partial r}{\partial \rho}\right)^2 + \left(\frac{\partial R_0}{\partial \rho}\right)^2 + 2\frac{\partial r}{\partial \rho}\frac{\partial R_0}{\partial \rho}\cos\theta} \\
 h_\theta &= \sqrt{\left(\frac{\partial r}{\partial \theta}\right)^2 + r^2} \\
 h_\phi &= R_0 + r\cos\theta
 \end{aligned} \tag{4.16}$$

The area scale factor can be simplified to:

$$\mathcal{H} = r\frac{\partial r}{\partial \rho} + \frac{\partial R_0}{\partial \rho}\left(r\cos\theta + \frac{\partial r}{\partial \theta}\sin\theta\right) \tag{4.17}$$

Following the methods of Section 3.4, values for these scale factors can be directly calculated, and used to determine the SF-OFA radial scale factor and basis vectors. These OFA and GFA systems of curvilinear basis vectors are not identical, unlike the circular model systems [Appendix C.1].

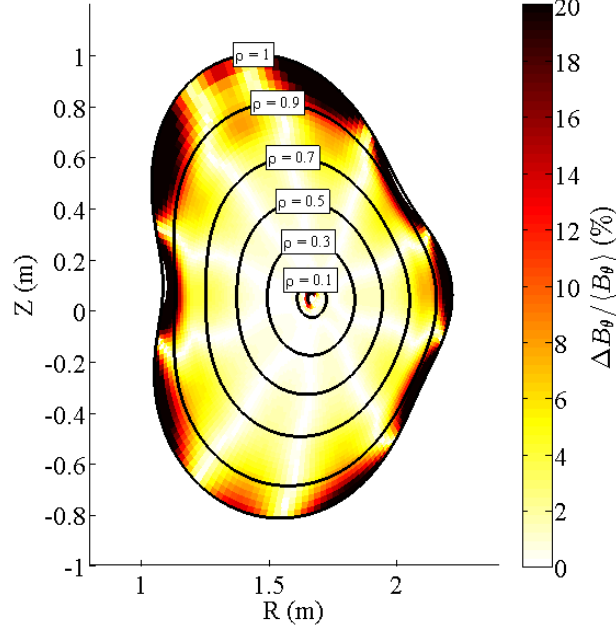


Figure 17: Field error \mathcal{E}_{field} for B_θ predictions using scale factors for an O(4) SF-OFA coordinate system [Eqs. (3.35), (3.20), (3.31), and (4.19)].

The error in the poloidal magnetic field calculated using the SF(4)-OFA coordinate system is around 1% for the inner plasma, and increases by an order of magnitude in the outside edge [Figure 17]. As with the positional error, even the 0th order SF expansion, with complexity comparable to the FC model, has a slightly lower positional error for the inner plasma, and a much lower error in the edge plasma. Despite the larger number of fitting coefficients, applying the 4th order SF expansion method produces a huge decrease in field error from the ~13% inner-plasma FC error [Table 5].

Table 5: Comparison of Single Fourier Magnetic field errors [Eq. (4.2)] (%) in three inner plasma sectors (left columns), and averaged over the full inner and edge plasma regions [Figure 12].

Model Type		Upper Hemisphere		Lower Hemisphere	$\overline{\langle \mathcal{E}_{field} \rangle}_{in}$	$\overline{\langle \mathcal{E}_{field} \rangle}_{edge}$
		Inner Error (%)		Inner Error (%)		
		$\overline{\langle \mathcal{E}_{field}^{upR} \rangle}_{in}$	$\overline{\langle \mathcal{E}_{field}^{upL} \rangle}_{in}$	$\overline{\langle \mathcal{E}_{field}^{low} \rangle}_{in}$		
Spline	CS	0.22	0.21	0.21	0.22	1.75
Fourier	SF(0)	14.06	9.17	10.79	11.49	29.79
	SF(2)	5.24	2.52	3.35	3.77	19.16
	SF(4)	1.37	0.91	0.96	1.07	9.68

4.4. Double Fourier Expansion model (DF) for R and Z

An alternative to the Single Fourier (SF) technique of expanding the minor radius using one Fourier expansion is to double the number of expansions, separately representing the poloidal variations in R and Z. Other analysis have applied this *Double Fourier* (DF) model [11]; it offers a greater degree of flexibility over the SF representation, although this is offset by an increases in complexity. Scale factors for an O(2) Double Fourier Orthogonalized Flux-surface Aligned (DF(2)-OFA) curvilinear system can be used to calculate a poloidal magnetic field distribution and poloidal field errors, which show that the DF system is less accurate than a Single-Fourier (SF) model of equivalent complexity at representing the EFIT data.

The Fourier-series representations for the semi-Cartesian components of the position vector [Eq. (3.10)] are:

$$\begin{aligned}
 R[\rho, \theta] &= \sum_{n=0}^N R^{s,n}[\rho] \sin n\theta + \sum_{n=0}^N R^{c,n}[\rho] \cos n\theta \\
 &= R_0 + \epsilon \sum_{n=1}^N (\tilde{R}^{s,n} \sin n\theta + \tilde{R}^{c,n} \cos n\theta) \\
 Z[\rho, \theta] &= \sum_{n=0}^N Z^{s,n}[\rho] \sin n\theta + \sum_{n=0}^N Z^{c,n}[\rho] \cos n\theta \\
 &= \epsilon \sum_{n=1}^N (\tilde{Z}^{s,n} \sin n\theta + \tilde{Z}^{c,n} \cos n\theta)
 \end{aligned} \tag{4.18}$$

where $R_0 = R^{c,0}$, $Z^{s,c,i} = \epsilon \tilde{Z}^{s,c,i}$, and $R^{s,c,i} = \epsilon \tilde{R}^{s,c,i}$. The coordinate system is chosen so that $Z_0 = Z_0^c = 0$.

A DF model will have half the expansion order of the SF model with an equivalent number of fitting parameters; consequently, an O(2) DF model with nine fitting coefficients ($R_0, R^{s,1}, R^{c,1}, Z^{s,1}, Z^{c,1}, R^{s,2}, R^{c,2}, Z^{s,2}, Z^{c,2}$) is comparable in complexity to the O(4) SF model with ten fitting coefficients analyzed in Section 4.3. Despite this increase in complexity, the flexibility of this DF model to describe a wide variety of flux-surface shapes, including surfaces which do not enclose the central major radius location (R_0), could potentially make it desirable for representing the structure of magnetic islands. As for the SF formalism, a linear least-squares method can be used to

determine the asymmetries which minimize the differences from EFIT in the DF predictions for R and Z.

Table 6: Averaged flux-surface positional error (%) number of expansion coefficients per. flux surface for two Double Fourier (DF) models.

Model	$\frac{N_{coef}}{surface}$	$\langle \mathcal{E}_{position} \rangle_{in}$	$\langle \mathcal{E}_{position} \rangle_{edge}$
Double Fourier O[1] (DF1)	5	4.5%	6.4%
Double Fourier O[2] (DF)	9	4.4%	5.8%

As the expansion order is increased, the ability of the DF model to represent the up-down plasma asymmetries improves slightly; both 0th and 1st order expansions have about half the positional error as the Flux-equivalent Circular (FC) model, although neither approach the accuracy of the O(2) and O(4) SF models of equivalent complexity. The changes in flux surface shapes as the expansion order is increased is illustrated in Figure 18, which compares the flux-surfaces for O(1) and O(2) DF expansions.

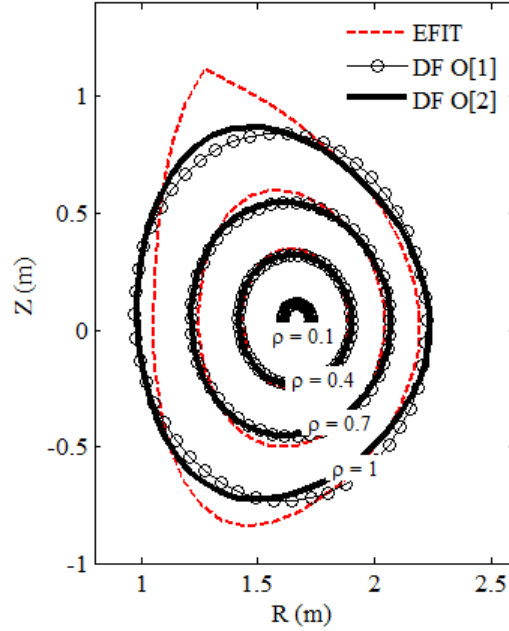


Figure 18: Comparison of EFIT flux surfaces (red dashes) with flux surface predictions for two orders of DF expansions [Eq. (4.18)] fitted to EFIT contours (circles, bold line).

The gradients of the components of the position vector defined in Eq. (4.18), in terms of the normalized asymmetries, are:

$$\begin{aligned}
\frac{\partial R}{\partial \rho} &= \frac{\partial R_0}{\partial \rho} + \epsilon \sum_{n=1}^N \left(\sin[n\theta] \frac{\partial \tilde{R}^{s,n}}{\partial \rho} + \cos[n\theta] \frac{\partial \tilde{R}^{c,n}}{\partial \rho} \right) \\
\frac{\partial Z}{\partial \rho} &= \epsilon \sum_{n=1}^N \left(\sin[n\theta] \frac{\partial \tilde{Z}^{s,n}}{\partial \rho} + \cos[n\theta] \frac{\partial \tilde{Z}^{c,n}}{\partial \rho} \right) \\
\frac{\partial R}{\partial \theta} &= \epsilon \sum_{n=1}^N n \left(\cos[n\theta] \tilde{R}^{s,n}[\rho] - \sin[n\theta] \tilde{R}^{c,n}[\rho] \right) \\
\frac{\partial Z}{\partial \theta} &= \epsilon \sum_{n=1}^N n \left(\cos[n\theta] \tilde{Z}^{s,n}[\rho] - \sin[n\theta] \tilde{Z}^{c,n}[\rho] \right)
\end{aligned} \tag{4.19}$$

These definitions can be used to calculate the directions of the Double Fourier General Flux-surface Aligned (DF-GFA) basis vectors according to Eq. (3.18)., and the general scale factors and area scale factor can be computed by Eq. (3.20) and Eq. (4.18). Similarly to the SF model basis vectors, the radial basis vectors in the DF GFA coordinate system are not perpendicular to flux surfaces, and consequently do not match the DF-OFA basis vectors [Appendix C.1]. Using Eq. (3.35), (3.31), and (3.20), the poloidal magnetic field can be expressed in terms of curvilinear gradients of R and Z .

$$B_\theta = \frac{1}{R} \sqrt{\left(\frac{\partial R}{\partial \theta}\right)^2 + \left(\frac{\partial Z}{\partial \theta}\right)^2} \left(\frac{\partial R}{\partial \rho} \frac{\partial Z}{\partial \theta} - \frac{\partial Z}{\partial \rho} \frac{\partial R}{\partial \theta}\right)^{-1} \frac{\partial \psi}{\partial \rho} \tag{4.20}$$

It is straightforward to apply the calculations of Section 3.4 and Eq. (4.20) for the poloidal magnetic field to determine the field error [Eq. (4.2)] throughout the DF model for the plasma geometry.

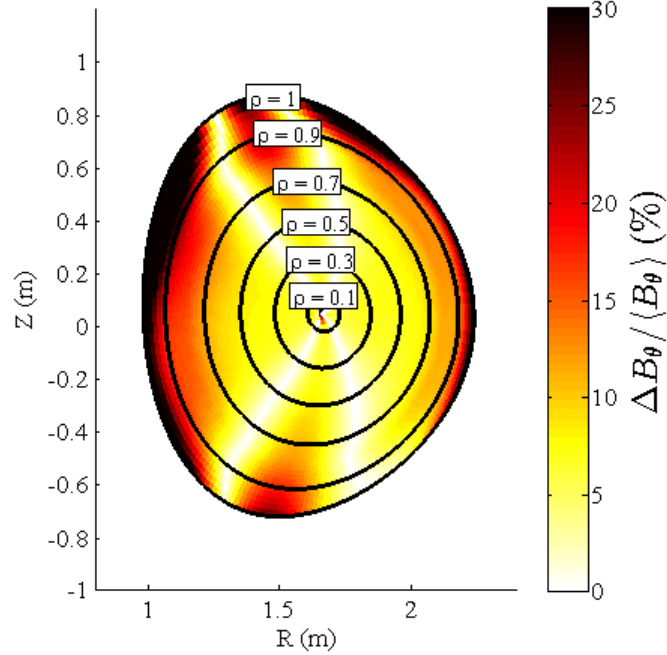


Figure 19: Field error \mathcal{E}_{field} for B_θ predictions using O[2] DF-OFA scale factors [Eqs. (3.35), (3.20), (3.31), and (4.19)].

Field errors throughout the DF plasma model are nearly half the size of the FC errors, but still much greater than errors for SF models of equivalent complexity.

Table 7: Comparison of Double Fourier Magnetic field errors [Eq. (4.2)] (%) in three inner plasma sectors (left columns), and averaged over the full inner and edge plasma regions [Figure 12].

Model Type		Upper Hemisphere		Lower Hemisphere	$\overline{\langle \mathcal{E}_{field} \rangle}_{in}$	$\overline{\langle \mathcal{E}_{field} \rangle}_{edge}$
		Inner Error (%)		Inner Error (%)		
		$\overline{\langle \mathcal{E}_{field}^{upR} \rangle}_{in}$	$\overline{\langle \mathcal{E}_{field}^{upL} \rangle}_{in}$	$\overline{\langle \mathcal{E}_{field}^{low} \rangle}_{in}$		
Spline	CS	0.22	0.21	0.21	0.22	1.75
Fourier	DF(1)	8.00	6.13	6.12	6.70	19.70
	DF(2)	6.43	5.93	5.55	5.90	15.01

4.5. Symmetric and Asymmetric Miller models (SM and AM)

A plasma model introduced by Miller [1] allows for a more accurate representation than the circular model of the elongated “D” shape of a plasma cross-section. This formalism represents the semi-Cartesian (R, Z) coordinates of plasma flux surfaces in terms of the plasma elongation κ and triangularity δ . The relationship

between these semi-Cartesian coordinates and the curvilinear (ρ, θ_m) coordinates is non-linear, requiring iterative methods to be used to fit this model to the EFIT-determined flux-surface shapes. This flux-surface fit can be improved if the *Symmetric Miller* (SM) model is extended to use separate values of elongation (κ) and triangularity (δ) to account for asymmetries between the upper and lower hemispheres [14]. This extension results in four fitting coefficients to represent each flux surface $(\kappa_{up}, \delta_{up}, \kappa_{low}, \delta_{low})$, and will be referred to as the *Asymmetric Miller* (AM) model. After developing Miller *Orthogonalized Flux-surface Aligned* (M-OFA) coordinates from the Miller *General Flux-surface Aligned* (M-GFA) coordinates, approximations for the plasma poloidal magnetic field show great improvements over both the circular and Fourier expansion models' predictions for B_θ .

The Miller major radius and elongation can be computed by

$$\begin{aligned} R[\rho, \theta] &= R_0 + r_0 \cos \xi \\ Z[\rho, \theta] &= \kappa r_0 \sin \theta_m \end{aligned} \tag{4.21}$$

Where $r_0[\rho] = a \rho$, $\xi[\rho, \theta] = \theta_m + x_\delta[\rho] \sin \theta_m$, and $x_\delta = \text{Sin}^{-1} \theta_m$. The directions of ξ and the Miller-model angle θ_m , relative to the true poloidal angle θ are shown in Figure 20. The angle ξ is used to form a right triangle with a hypotenuse equal to the minor radius r_0 and a horizontal side equal to the difference $(R - R_0)$. The angle θ_m is used similarly, along with the elongation κ , to form a triangle with a height of distance Z , and hypotenuse of length (κr_0) .

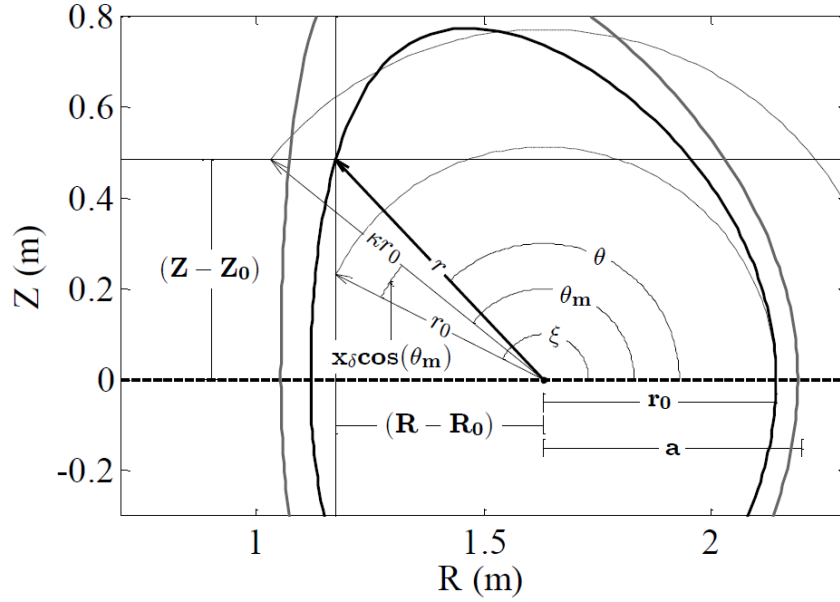


Figure 20: Geometric relationship of R , Z , and θ with Miller parameters R_0 , a , x_δ , κ , ξ , and θ_m .

In Miller's original *Symmetric Miller* (SM) formulation of this model, two fitting parameters - elongation (κ) and triangularity (δ) - were used to parameterize each complete flux surface. However, flux surfaces can often be better represented by using separate values of these two parameters to describe the upper and lower plasma hemispheres. Because the expressions in Eq. (4.21) are independent of the values of κ and δ on the midplane where $\theta_m = \theta = [0, \pi]$, the extension of this model to a piecewise poloidally constant *Asymmetric Miller* (AM) model for δ and κ , discontinuous at the midplane, still returns a representation of the R and Z components of the position vector which is continuous with respect to ρ and θ_m , while adding the ability to represent up-down plasma asymmetries.

In order to apply a least-squares method to determine the fitted values of κ and x_δ which correspond to Miller flux surfaces in best agreement with the EFIT data for R and Z , the two expressions in Eq. (4.21) can be rearranged to solve for the flux-surface values of x_δ and κ in terms of θ_m .

$$\begin{aligned}
x_\delta[\rho] &= \frac{1}{N_\theta} \sum_{n=1}^{N_\theta} \frac{1}{\sin \theta_{m,n}} \left(\arccos \left[\frac{R[\rho, \theta_n] - R_0[\rho]}{a\rho} \right] - \theta_{m,n} \right) \\
\kappa[\rho] &= \frac{1}{N_\theta} \sum_{n=1}^{N_\theta} \frac{1}{\sin \theta_{m,n}} \frac{Z[\rho, \theta_n]}{a\rho}
\end{aligned} \tag{4.22}$$

The expressions in Eq. (4.22) can be computed from EFIT data for $(R - R_0)$ and (Z) on flux surfaces [Figure 10], using the true poloidal angle as an initial guess for θ_m . When determining Symmetric Miller (SM) fits for radially dependent κ and x_δ , all poloidal angles are considered together, and N_θ is equal to the number of points used to represent locations on each EFIT ψ contour. To determine Asymmetric Miller (AM) fits, κ and x_δ must be determined separately for upper and lower hemispheres. This requires that the summations of Eq. (4.22) be performed over the range $(1 < n < N_\theta/2)$ to determine κ_{up} and $x_{\delta,up}$, and over $(N_\theta/2 + 1 < n < N_\theta)$ to determine κ_{low} and $x_{\delta,low}$. Subsequently, the value of θ_m can be updated from the κ and δ fit-parameters, by using a nonlinear Newton's method to solve:

$$\tan \left[\frac{R - R_0}{Z} \right] = \frac{\cos[\theta_m + x_\delta \sin \theta_m]}{\kappa \sin \theta_m} \tag{4.23}$$

for θ_m , where R , R_0 , and Z are determined from EFIT contours. By converging Eqs. (4.22)-(4.23) separately on for the upper and lower plasma hemispheres on each flux-surface, converged fitted values of $(\kappa_{up}, x_{\delta,up})$ and $(\kappa_{low}, x_{\delta,low})$ can be determined which yield the best AM fit for the EFIT flux surface contours.

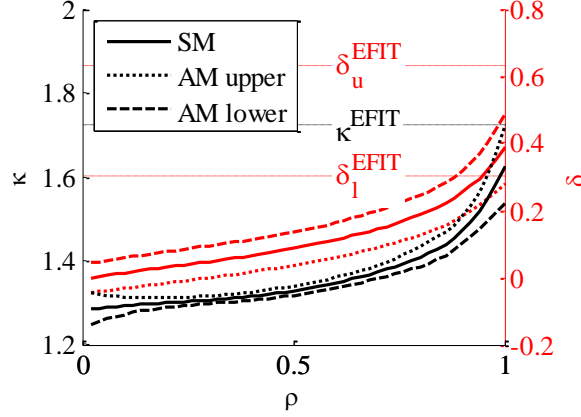


Figure 21: Radial dependence of Miller plasma elongation κ (left axes) and modified triangularity x_δ (right axes), for Symmetric Miller (solid line) and Asymmetric Miller upper and lower (dotted and dashed) hemispheres of Shot# 149468, 1905ms.

The radial profiles of converged values for κ and x_δ coefficients are subsequently fitted using 4th order polynomials, so that their radial gradients can be calculated analytically. Separate polynomial fits are used for $\rho < 0.7$ and $\rho > 0.7$, although the radial profiles and gradients are constrained to be continuous at $\rho = 0.7$. The LCFS values of the resulting radial profiles for upper plasma elongation and lower plasma triangularity shown in Figure 21 match well with the EFIT values of $\kappa^{EFIT} = 1.722$ and $\delta_{low}^{EFIT} = 0.303$. Interestingly, the LCFS value of upper triangularity is noticeably smaller than the EFIT-predicted value of $\delta_{up}^{EFIT} = 0.630$, suggesting a difference between methods of determining this parameter.

Table 8: Positional Errors (%) and number of fitting coefficients per. flux surface for the Symmetric Miller (SM) and the Asymmetric Miller (AM) models.

Model	$\frac{N_{coef}}{surface}$	$\langle \mathcal{E}_{position} \rangle_{in}$	$\langle \mathcal{E}_{position} \rangle_{edge}$
Symmetric Miller (SM)	4	0.91	1.44
Asymmetric Miller (AM)	6	0.32	0.43

The flux surface agreement for both variations of the Miller model is almost two orders of magnitude better than the agreement between the FC model and spline-fit flux surfaces presented in Section 4.2 [Table 2], and both models appropriately account for the Shafranov shift. The averages of AM positional error are around a third of the SM

error; the difference is especially notable when comparing flux surface agreement in the edge plasma regions, as seen in Figure 22.

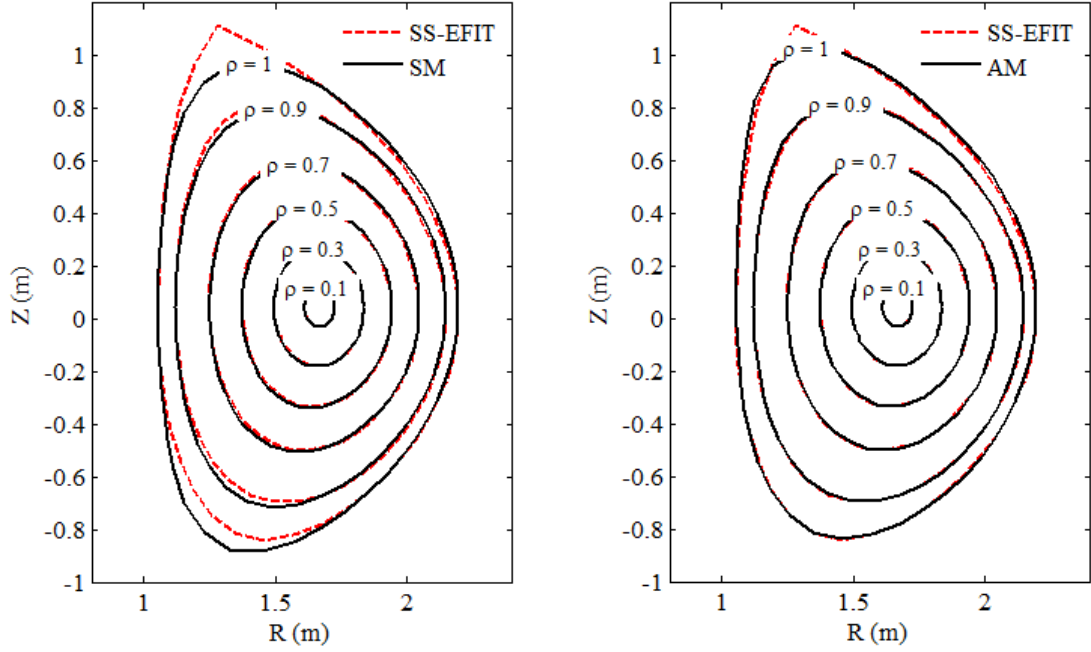


Figure 22: Symmetric Miller (left, black) and Asymmetric Miller (right, black) predictions for flux surfaces Eq. (4.21), compared to EFIT SS flux surfaces (red dashed).

The gradients of the components of the position vector $\vec{s}[\rho, \theta_m]$ given in Eq. (4.21) can be represented analytically in terms of κ , x_δ , R_0 , and a .

$$\begin{aligned}
 \frac{\partial R}{\partial \rho} &= \frac{\partial R_0}{\partial \rho} + a \left(\cos \xi - \left(\frac{\partial x_\delta}{\partial \rho} \rho \sin \theta_m \right) \sin \xi \right) \\
 \frac{\partial R}{\partial \theta} &= -a(1 + x_\delta \cos \theta_m) \rho \sin \xi \\
 \frac{\partial Z}{\partial \rho} &= a \left(\kappa + \rho \frac{\partial \kappa}{\partial \rho} \right) \sin \theta_m \\
 \frac{\partial Z}{\partial \theta} &= \kappa a \rho \cos \theta_m
 \end{aligned} \tag{4.24}$$

The poloidal area scale factor for Miller General Flux-surface Aligned (M-GFA) coordinates can be derived by applying the definitions of Eq. (4.24) to the calculations developed in Section 3.3.

$$\mathcal{H} = a^2 \rho \kappa \left(\left(\frac{1}{a} \frac{\partial R_0}{\partial \rho} + \cos \xi \right) \cos \theta_m + \left(\left(1 + \frac{1}{\kappa} \frac{\partial \kappa}{\partial \rho} \right) \rho \right) (1 + x_\delta \cos \theta_m) - \left(\frac{\partial x_\delta}{\partial \rho} \right) \rho \cos \theta_m \right) \sin \xi \sin \theta_m \quad (4.25)$$

The area scale factor Eq. (4.25) can subsequently be used in the calculations of Section 3.4 to yield the orthogonalized scale factors from the M-OFA coordinate system.

The final forms of the M-OFA scale factors in terms of κ , x_δ , a , and R_0 profiles and poloidally dependent ξ and θ_m angles are:

$$h_\rho^\perp = \frac{a \left(\left(\frac{1}{a} \frac{\partial R_0}{\partial \rho} + \cos \xi \right) \cos \theta_m + \left(\left(1 + \frac{\rho}{\kappa} \frac{\partial \kappa}{\partial \rho} \right) (1 + x_\delta \cos \theta_m) - \rho \frac{\partial x_\delta}{\partial \rho} \cos \theta_m \right) \sin \xi \sin \theta_m \right)}{\sqrt{\cos^2 \theta_m + \frac{1}{\kappa^2} (1 + x_\delta \cos \theta_m)^2 \sin^2 \xi}}$$

$$h_\theta = a \rho \sqrt{\kappa^2 \cos^2 \theta_m + (1 + x_\delta \cos \theta_m)^2 \sin^2 \xi} \quad (4.26)$$

$$h_\phi = R_0 + a \rho \cos \xi$$

In the limit of $\kappa \rightarrow 1$, $\delta \rightarrow 0$, and $\frac{\partial R_0}{\partial \rho} \rightarrow 0$, the above expressions reduce to the circular model form, with $\bar{a} = a$.

Unlike the circular model, the M-GFA and M-OFA coordinate systems are not equivalent, especially in the plasma edge. Plotting the *Asymmetric Miller Orthogonalized Flux-surface Aligned* (AM-OFA) covariant basis vectors weighted by $d\rho = 0.1$, $d\theta = 0.16$ for ($0 \leq \theta_m < 2\pi$) on six evenly spaced flux surfaces with ($0 < \rho < 1$) [Figure 23] illustrates how these basis vectors always describe orthogonalized coordinate directions. The coordinate system orientation changes based on poloidal position so that the poloidal basis vectors remain parallel to flux-surface contours (poloidally-directed bold arrows), and the radial basis vectors remain perpendicular to flux-surface contours (radially-directed bold arrows). In contrast, the AM-GFA covariant radial basis vectors are oriented outward along contours of constant θ_m , which have no physical significance in the plasma. These radial covariant basis vectors (dashed arrows) often show significant variations from the flux-surface normal directions, especially in the plasma edge.

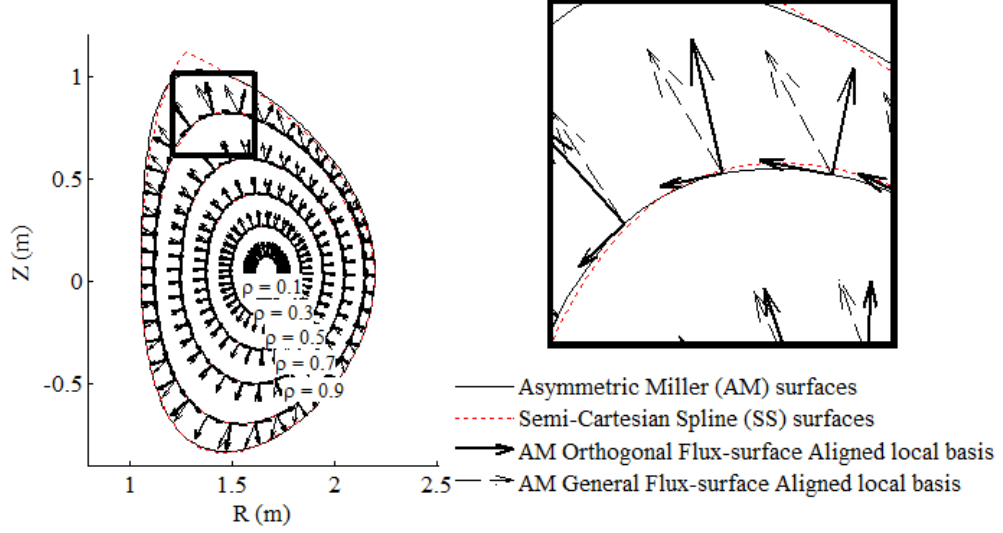


Figure 23: Comparison of AM-GFA basis vectors (narrow arrows) with AM-OFA basis vectors (bold arrows) [Eq. (4.26)] on sample AM flux surfaces. Magnification of inset shown on right.

In Asymmetric Miller coordinates, the magnitude of the components of the magnetic field can be computed by applying the orthogonalized scale factors in in Eq. (3.17).

$$\begin{aligned}
 B_\phi &= \frac{\bar{B}_\phi}{1 + \varepsilon \cos \xi} \\
 B_\theta &= \frac{\bar{B}_\theta}{1 + \varepsilon \cos \xi} \frac{\sqrt{\cos^2 \theta_m + \frac{1}{\kappa^2} (1 + x \cos \theta_m)^2 \sin^2 \xi}}{\left(\left(\frac{1}{a} \frac{\partial R_0}{\partial \rho} + \cos \xi \right) \cos \theta_m + \left(\left(1 + \frac{\rho}{\kappa} \frac{\partial \kappa}{\partial \rho} \right) (1 + x_\delta \cos \theta_m) - \rho \frac{\partial x_\delta}{\partial \rho} \cos \theta_m \right) \sin \xi \sin \theta_m \right)}
 \end{aligned} \tag{4.27}$$

The expressions of Eq. (4.27) allow the components of the magnetic field to be calculated analytically directly from the fitted values for κ and δ determined using Eqs. (4.22)-(4.23). The distribution of field errors in the AM model predictions for B_θ are shown in Figure 24.

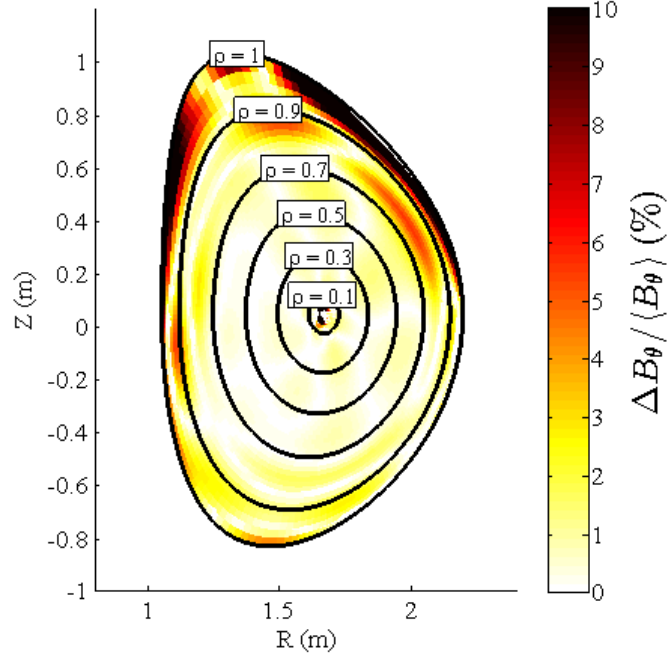


Figure 24: Field error \mathcal{E}_{field} for B_θ predictions using AM-OFA scale factors [Eq. (4.27)].

When compared to the semi-Cartesian calculation of the poloidal magnetic field, the average inner plasma field errors for the Miller models are at or below 1% [Figure 9]. The Asymmetric Miller (AM) model has errors comparable to the Curvilinear Spline field errors, while requiring over 60 times fewer fitting coefficients to represent a flux surface.

Table 9: Comparison of Miller poloidal magnetic field errors [Eq. (4.2)] (%) in three inner plasma sectors (left columns), and averaged over the full inner and edge plasma regions [Figure 12].

Model Type		Upper Hemisphere		Lower Hemisphere	$\overline{\langle \mathcal{E}_{field} \rangle}_{in}$	$\overline{\langle \mathcal{E}_{field} \rangle}_{edge}$
		Inner Error (%)		Inner Error (%)		
		$\overline{\langle \mathcal{E}_{field}^{upR} \rangle}_{in}$	$\overline{\langle \mathcal{E}_{field}^{upL} \rangle}_{in}$	$\overline{\langle \mathcal{E}_{field}^{low} \rangle}_{in}$		
Spline	CS	0.22	0.21	0.21	0.22	1.75
Miller	SM	1.46	0.59	1.01	1.07	4.54
	AM	0.87	0.28	0.36	0.50	3.89

4.6. Summary of analytic curvilinear coordinate models

The effectiveness of the most accurate variations of each class of curvilinear geometry models methods can be compared based on their accuracy at representing the true plasma flux surfaces and poloidal magnetic field over flux surfaces. The Flux-equivalent Circular model is significantly less accurate than the O(2) Double and O(4) Single Fourier expansion methods; the most accurate models are the Asymmetric Miller and Curvilinear Spline fits. Evaluating fitting methods based on a performance parameter Γ which accounts for the benefits of simplicity clearly illustrates the superiority of the Asymmetric Miller fitting method at representing variations in poloidal magnetic field for plasma, especially within the $q = 2$ rational flux surface.

Comparing the radial variations in FSA of positional and field errors for the Flux-equivalent Circular, Single Fourier, Double Fourier, Asymmetric Miller, and Curvilinear Spline models illustrates how well these four classes of fitting techniques perform as a function of minor radius [Figure 25]. The effectiveness of all models generally decreases towards the plasma edge, and the poloidal magnetic field error $\langle \mathcal{E}_{field} \rangle$ increases much more rapidly than positional error $\langle \mathcal{E}_{position} \rangle$. The Flux-equivalent Circular (FC) model is the least accurate method in both classes, with up to $\sim 100\%$ field error at the plasma edge.

Both the Single Fourier and Asymmetric Miller methods are around an order of magnitude better than the Double Fourier method towards the plasma center. However, whereas the AM positional error is almost independent of radial location for $\rho < 0.9$, the SF positional and magnetic field error increase exponentially from the plasma center to DF-comparable errors in the edge. The Curvilinear Spline method shares flux-surface position with the reference Semi-Cartesian Spline surfaces, and consequently has no positional error. Its poloidal field error is the smallest of all models, although it is comparable to the AM field error at several locations.

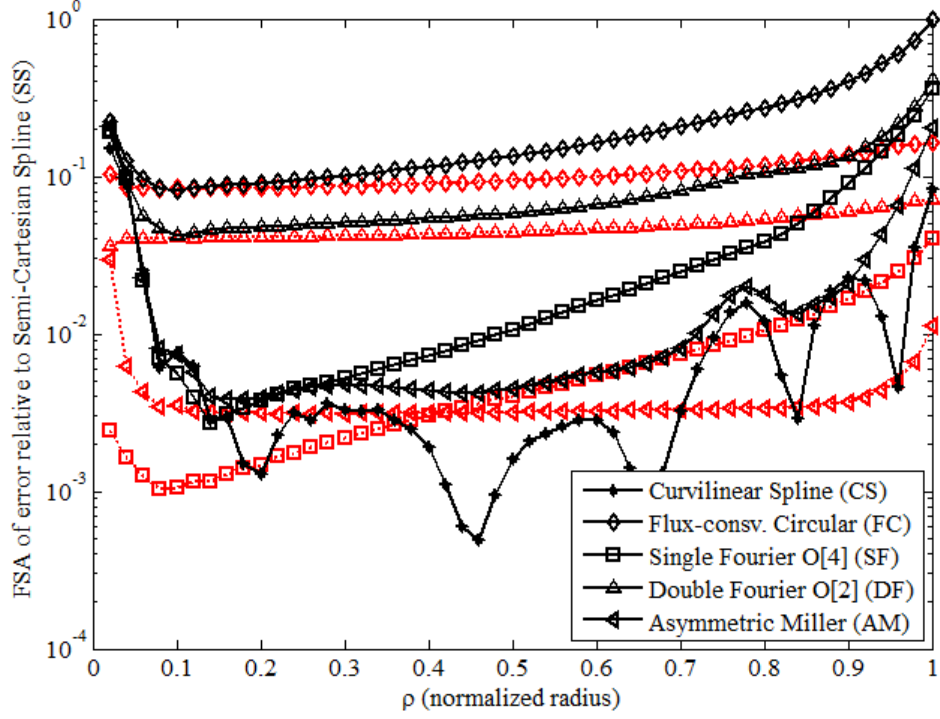


Figure 25: Flux surface averages of positional error $\langle \mathcal{E}_{position} \rangle$ [red, Eq. (4.1)] and poloidal field error $\langle \mathcal{E}_{field} \rangle$ [black, Eq. (4.2)] for CS, FC, AM, DF, and SF coordinate system models.

A performance parameter can be defined to evaluate models based on a balance of their accuracy and their simplicity.

$$\Gamma = \frac{\left(\langle \mathcal{E}_{field} \rangle \right)^{-1}}{N_{coef}} \quad (4.28)$$

Larger values of Γ indicate more effective plasma models. Because the agreement of many models is significantly different between the plasma center and edge, this performance parameter will be evaluated separately for inner (Γ_{in}) and edge (Γ_{edge}) plasma, based on the inner and outer averaged field errors [Eq. (4.2)].

Table 10: Comparison of sector dependent field errors, number of fitting coefficients per flux surface, and both inner and outer performance parameters for the most effective geometry models of each class considered in this analysis.

Model Type	Upper Hemisphere		Lower Hemisphere	$\frac{N_{fit}}{surface}$	Γ_{in}	Γ_{edge}
	Inner Error (%)		Inner Error (%)			
	$\langle \mathcal{E}_{field}^{upR} \rangle_{in}$	$\langle \mathcal{E}_{field}^{upL} \rangle_{in}$	$\langle \mathcal{E}_{field}^{low} \rangle_{in}$			
Curvilinear Spline (CS)	0.224	0.207	0.215	400	1.2	0.14
Flux-equivalent Circular (FC)	18.0	7.35	12.3	2	3.8	1.25
O(4) Single Fourier (SF)	1.37	0.91	0.96	10	9.3	1.03
O(2) Double Fourier (DF)	6.42	5.93	5.55	9	1.9	0.74
Asymmetric Miller (AM)	0.867	0.283	0.362	6	33	4.29

It is interesting to note the relative ineffectiveness of the Double Fourier method, due to the large number of fitting coefficients outweighing the relatively low fitting accuracy. In contrast, the O(4) Single Fourier model performs much better than the Flux-equivalent Circular model, indicating that the disadvantage of increasing the number of fitting coefficients from the O(1) SF model (which is a variation of the circular model) is more than compensated for by the increase in accuracy. This suggests that higher orders of the SF model would be the best choice if a plasma model with accuracy higher than that of the Asymmetric Miller model is required.

Overall, the Asymmetric Miller model is shown to be the most effective method for calculating the plasma poloidal magnetic field from the plasma geometry. It is the only model besides a Curvilinear Spline fit with averaged field error below 1% for all sectors of the inner plasma, and its performance parameter is an order of magnitude larger than all others. This analysis indicates that the Asymmetric Miller model is the

best method of representing the inner plasma; it will be applied in the remainder of this analysis to formulate the plasma equations.

CHAPTER 5

FORMULATING CONTINUITY AND MOMENTUM BALANCE EQUATIONS IN CURVILINEAR COORDINATE SYSTEM

The basic continuity and momentum balance equations undergo significant simplification when formulated in a curvilinear coordinate system. Plasma flow between flux surfaces is very small in comparison to movement on the surfaces, which allows the radial momentum balance to be reduced to the balance of pressure and electromagnetic effects [Eq. (5.3)]. Although all the original terms of the poloidal momentum balance equation must still be evaluated [Eq. (5.5)], axisymmetry and the lack of a significant radial magnetic field simplify the pressure and electromagnetic contributions in the toroidal angular momentum balance [Eq. (5.8)]. The flux-surface average of the toroidal angular momentum balance reduces to a gyroviscous drag torque balanced with electromagnetic, frictional, and external momentum torques [Eq. (5.7)].

The quantities comprising the plasma equations can be separated into three classifications: those dependent on the plasma geometry, asymmetries describing the poloidal variation of plasma properties, and mean values of all plasma properties. Distributions for the geometry-dependent quantities (scale factors and magnetic fields) throughout the plasma can be determined completely from EFIT data using the methods described in Section 0. The plasma asymmetries can all be expressed in terms of the poloidal variations in density, velocity, and electric potential. Setting all the mean values for plasma properties from experimental measurements, allows the plasma equations to be applied to solve for the poloidal variations in plasma properties.

5.1. Equations formulated for curvilinear coordinates

In curvilinear coordinates, expanding Eq. (2.1) and applying the FSA operation yields the continuity equation for a flux surface in a toroidally symmetric plasma.

$$\left\langle \frac{1}{h_\theta h_\rho h_\phi} \left(\frac{\partial \llbracket V_{r,i} n_i h_\theta h_\phi \rrbracket}{\partial \rho} + \frac{\partial \llbracket V_{\theta,i} n_i h_\rho h_\phi \rrbracket}{\partial \theta} \right) \right\rangle_{streaming} = \langle S_i^0 \rangle_{source} \quad (5.1)$$

The second term in Eq. (5.1) vanishes in the FSA operation, and the remaining form of the FSA of the continuity equation in a general orthogonal curvilinear system relates the particle source and the radial particle flux $\Gamma = nV_r$.

$$\left\langle \frac{1}{h_\theta h_\rho h_\phi} \frac{\partial [V_{r,i} n_i h_\theta h_\phi]}{\partial \rho} \right\rangle = \langle S_{i}^0 \rangle \quad (5.2)$$

In curvilinear coordinates, the plasma flow is very small across flux surfaces – the radial direction in flux surface aligned coordinates. Thus, in the radial component of the momentum balance equation, the inertial, viscous, and frictional terms are negligibly small in comparison to the pressure and electromagnetic contributions. The radial balance reduces to the FSA of a balance between the outward pressure force, and the inward-directed electromagnetic force comprised of the radial electric field and the magnetic pinch.

$$\left\langle \frac{1}{h_\rho} \frac{\partial [p_i]}{\partial \rho} \right\rangle = \left\langle e_i n_i \left(-\frac{1}{h_\rho} \frac{\partial \Phi}{\partial \rho} + B_\phi V_{\theta,i} - B_\theta V_{\phi,i} \right) \right\rangle \quad (5.3)$$

In the poloidal direction, the FSA of the momentum balance equation becomes [Appendix A]:

$$\begin{aligned} & m_i \left\langle \frac{1}{h_\theta^2 h_\rho h_\phi} \frac{\partial [V_{\theta,i} V_{r,i} n_i h_\theta h_\phi^2]}{\partial \rho} + \frac{1}{h_\theta h_\rho h_\phi} \frac{\partial [V_{\theta,i}^2 n_i h_\theta h_\rho]}{\partial \theta} - n_i \left(\frac{V_{r,i}^2}{h_\theta h_\rho} \frac{\partial h_\rho}{\partial \theta} + \frac{V_{\phi,i}^2}{h_\theta h_\phi} \frac{\partial h_\phi}{\partial \theta} \right) \right\rangle_{inertial} + \\ & \left\langle \frac{1}{h_\theta^2 h_\rho h_\phi} \frac{\partial [\Pi_{r,\theta} h_\theta^2 h_\phi]}{\partial \rho} + \frac{1}{h_\theta h_\rho h_\phi} \frac{\partial [\Pi_{\theta,\theta} h_\rho h_\phi]}{\partial \theta} - \frac{1}{h_\theta h_\rho} \frac{\partial h_\rho}{\partial \theta} \Pi_{r,r} - \frac{1}{h_\theta h_\phi} \frac{\partial h_\phi}{\partial \theta} \Pi_{\phi,\phi} \right\rangle_{viscous} + \\ & \left\langle \frac{1}{h_\theta} \frac{\partial [p_i]}{\partial \theta} \right\rangle_{pressure} = \left\langle e_i n_i \left(-\frac{1}{h_\theta} \frac{\partial \Phi}{\partial \theta} - B_\phi V_{r,i} \right) \right\rangle_{emag} + \left\langle m_i n_i (V_{\theta,i} - V_{\theta,j}) v_{i,j} \right\rangle_{friction} + \langle S_{\theta,i}^1 \rangle_{source} \end{aligned} \quad (5.4)$$

The second elements in both the inertial and viscous pieces vanish in the FSA operation. In the ordering $f_r \ll f_p < 1$, the $\Pi_{r,\theta}$ tensor element has no dependence on parallel viscosity, and is negligible in comparison to $\Pi_{r,r}^0$ and $\Pi_{\theta,\theta}^0$ [8]. Additionally, there is no significant external source of poloidal momentum in the plasma core. The simplified form of the FSA of the poloidal momentum balance then becomes

$$\begin{aligned}
& \left\langle \frac{m_i}{h_\theta^2 h_\rho h_\phi} \frac{\partial \llbracket V_{\theta,i} V_{r,i} n_i h_\phi h_\theta^2 \rrbracket}{\partial \rho} \right\rangle - \left\langle m_i n_i \left(\frac{V_{r,i}^2}{h_\theta h_\rho} \frac{\partial h_\rho}{\partial \theta} + \frac{V_{\phi,i}^2}{h_\theta h_\phi} \frac{\partial h_\phi}{\partial \theta} \right) \right\rangle - \left\langle \frac{1}{h_\theta h_\rho} \frac{\partial h_\rho}{\partial \theta} \Pi_{r,r}^0 \right\rangle - \\
& \left\langle \frac{1}{h_\theta h_\phi} \frac{\partial h_\phi}{\partial \theta} \Pi_{\phi,\phi}^0 \right\rangle + \left\langle \frac{1}{h_\theta} \frac{\partial \llbracket p_i \rrbracket}{\partial \theta} \right\rangle = \left\langle e_i n_i \left(-\frac{1}{h_\theta} \frac{\partial \Phi}{\partial \theta} - B_\phi V_{r,i} \right) \right\rangle + \left\langle m_i n_i (V_{\theta,i} - V_{\theta,j}) v_{i,j} \right\rangle
\end{aligned} \tag{5.5}$$

The cross-product of the momentum balance equation with the tokamak major radius returns the toroidal angular momentum balance, describing torque about the tokamak central axis [Appendix A].

$$\begin{aligned}
& \left\langle \frac{m_i}{h_\theta h_\rho h_\phi} \left(\frac{\partial \llbracket V_{\phi,i} V_{r,i} n_i h_\phi^2 h_\theta \rrbracket}{\partial \rho} + \frac{\partial \llbracket V_{\phi,i} V_{\theta,i} n_i h_\phi^2 h_\rho \rrbracket}{\partial \theta} \right) \right\rangle_{inertial} + \left\langle \frac{1}{h_\theta h_\rho h_\phi} \left(\frac{\partial \llbracket \Pi_{r,\phi} h_\phi^2 h_\theta \rrbracket}{\partial \rho} + \frac{\partial \llbracket \Pi_{\theta,\phi} h_\phi^2 h_\rho \rrbracket}{\partial \theta} \right) \right\rangle_{viscous} + \\
& \left\langle \frac{1}{h_\phi} \frac{\partial p_i}{\partial \phi} \right\rangle_{pressure} = \left\langle h_\phi e_i n_i \left(-\frac{\partial \llbracket A_\phi \rrbracket}{\partial t} + B_\theta V_{r,i} \right) \right\rangle_{emag} + \left\langle h_\phi m_i n_i (V_{\phi,i} - V_{\phi,j}) v_{i,j} \right\rangle_{friction} + \left\langle h_\phi S_{\phi,i}^1 \right\rangle_{beam}
\end{aligned} \tag{5.6}$$

The first term in the inertial component is dependent on the radial velocity, and can be neglected, while the second term vanishes in the FSA operation. Because the second term in the viscous component vanishes in the FSA operation, the remaining $\Pi_{r,\phi}$ component of the viscosity tensor determines the viscous contribution to the toroidal angular momentum balance. Because the parallel viscosity contribution to this term vanishes in the ordering $f_r \ll f_p \ll 1$, the gyroviscosity $\Pi_{r,\phi}^{3,4}$ becomes the dominant viscous force in Eq. (5.6). The pressure gradient in the toroidal direction vanishes by axisymmetry, and the remaining, simplified form of the equation becomes:

$$\left\langle \frac{1}{h_\theta h_\rho h_\phi} \left(\frac{\partial \llbracket \Pi_{r,\phi}^{3,4} h_\phi^2 h_\theta \rrbracket}{\partial \rho} \right) \right\rangle = \left\langle h_\phi e_i n_i \left(-\frac{\partial \llbracket A_\phi \rrbracket}{\partial t} + B_\theta V_{r,i} \right) \right\rangle + \left\langle h_\phi m_i n_i (V_{\phi,i} - V_{\phi,j}) v_{i,j} \right\rangle_{friction} + \left\langle h_\phi S_{\phi,i}^1 \right\rangle_{beam} \tag{5.7}$$

If the toroidal angular momentum balance equation is weighted by any poloidally dependent function before the FSA operation is applied, the poloidally-dependent portion of the inertial term and the parallel viscosity do not vanish. Forms of Eq. (5.6) weighted by the Fourier basis functions $g[\theta] = \text{Sin}[\theta], \text{Cos}[\theta]$, will be applied to calculate poloidal asymmetries in the toroidal component of velocity, and take the form:

$$\begin{aligned}
& m_i \left\langle \frac{g[\theta]}{h_\theta h_\rho h_\phi} \left(\frac{\partial \llbracket V_{\phi,i} V_{\theta,i} n_i h_\phi^2 h_\rho \rrbracket}{\partial \theta} \right) \right\rangle + \left\langle \frac{g[\theta]}{h_\theta h_\rho h_\phi} \left(\frac{\partial \llbracket \Pi_{\theta,\phi}^0 h_\phi^2 h_\rho \rrbracket}{\partial \theta} \right) \right\rangle \\
& = \left\langle g[\theta] h_\phi e_i n_i \left(-\frac{\partial \llbracket A_\phi \rrbracket}{\partial t} + B_\theta V_{r,i} \right) \right\rangle + \left\langle g[\theta] h_\phi m_i n_i (V_{\phi,i} - V_{\phi,j}) v_{i,j} \right\rangle + \left\langle g[\theta] h_\phi S_{\phi,i}^1 \right\rangle
\end{aligned} \tag{5.8}$$

5.2. Relating unknown poloidal variations in plasma properties to asymmetries in density, velocity, and electric potential.

In the plasma equations, the curvilinear representation for the distributions of all plasma properties can be simplified by separation of variables into a poloidally dependent ‘‘asymmetry’’ contribution, and a radially dependent ‘‘mean’’ value describing the averaged behavior on a flux surface. The poloidal variations in plasma density, components of velocity, and electric potential can be expanded using low order Fourier series, which introduces a Sine and Cosine Fourier asymmetry for each of these variables. Poloidal variations in plasma collision frequencies, gyrofrequencies, and viscosity coefficients can be expressed in terms of these asymmetries and geometric scale factors.

A general poloidally dependent quantity $x[\rho, \theta]$ can be separated into radially and poloidally dependent contributions.

$$x[\rho, \theta] = \bar{x}[\rho] \tilde{x}[\theta] \tag{5.9}$$

The first part of the right of Eq. (5.9) will be referred to as the mean value of quantity x at flux surface ρ , and is a radially dependent quantity describing how plasma parameters change between flux surfaces. The second piece is purely poloidally dependent, and represents how plasma parameters vary within flux surfaces. Using a technique similar to that applied to represent minor radius in the SF model, the poloidally-dependent portion of Eq. (5.9) can be represented in the form:

$$\begin{aligned}
\tilde{x}[\theta] &= 1 + \sum_{n=1}^N (x^{s,n} \sin n\theta + x^{c,n} \cos n\theta) = 1 + \epsilon \bar{x} \\
\bar{x} &= \sum_{n=1}^N (\tilde{x}^{s,n} \sin n\theta + \tilde{x}^{c,n} \cos n\theta)
\end{aligned} \tag{5.10}$$

In this analysis, the poloidal variations in density (n), electric potential (Φ), and both poloidal and toroidal velocities (V_θ, V_ϕ) throughout the plasma equations described in Section 5.1 are expanded in this manner to first order.

$$\begin{aligned}
n_i[\rho, \theta] &= \bar{n}_i \tilde{n}_i = \bar{n}_i (1 + \epsilon \tilde{n}_i^{sl} \sin[\theta] + \epsilon \tilde{n}_i^{cl} \cos[\theta]) \\
\Phi[\rho, \theta] &= \bar{\Phi} \tilde{\Phi} = \bar{\Phi} (1 + \epsilon \tilde{\Phi}^{sl} \sin[\theta] + \epsilon \tilde{\Phi}^{cl} \cos[\theta]) \\
V_{p,i}[\rho, \theta] &= \bar{V}_{\theta,i} \tilde{V}_{\theta,i} = \bar{V}_{\theta,i} (1 + \epsilon \tilde{V}_{\theta,i}^{sl} \sin[\theta] + \epsilon \tilde{V}_{\theta,i}^{cl} \cos[\theta]) \\
V_{\phi,i}[\rho, \theta] &= \bar{V}_{\phi,i} \tilde{V}_{\phi,i} = \bar{V}_{\phi,i} (1 + \epsilon \tilde{V}_{\phi,i}^{sl} \sin[\theta] + \epsilon \tilde{V}_{\phi,i}^{cl} \cos[\theta])
\end{aligned} \tag{5.11}$$

Temperature and radial velocity in these equations are assumed to have no poloidal variation, and are approximated using only flux-surface dependent mean values.

$$\begin{aligned}
T_i[\rho, \theta] &= \bar{T}_i \\
V_{r,i}[\rho, \theta] &= \bar{V}_{r,i}
\end{aligned} \tag{5.12}$$

The poloidal dependence of both isotropic pressure ($p = nT$) and collision frequency (ν) can be expressed in terms of the density asymmetry.

$$p_i[\rho, \theta] = n_i T_i = \bar{p}_i \tilde{n}_i, \quad \bar{p}_i = \bar{n}_i \bar{T}_i \tag{5.13}$$

$$\begin{aligned}
\nu_{i,j}[\rho, \theta] &= \bar{\nu}_{i,j} \tilde{n}_j \\
\nu_{i,j}^*[\rho, \theta] &\approx \hat{\nu}_{i,j} \tilde{n}_j
\end{aligned} \tag{5.14}$$

The poloidal dependence of the gyrofrequency can be separated from the mean-value of gyrofrequency, and is the same as the poloidal variation of toroidal magnetic field [Eq. (3.42)].

$$\Omega_i[\rho, \theta] = \bar{\Omega}_i \left(\frac{R_0}{h_\phi} \right) \tag{5.15}$$

with $\bar{\Omega}_i = \frac{e_i \bar{B}_\phi}{m_i}$. Consequently, the poloidal dependence of the gyroviscous viscosity

coefficients can be written in terms the radially dependent mean viscosity coefficients $\bar{\eta}_i^{3,4}$, where the poloidal dependence is the combination of the poloidal variations in the density and the poloidal dependence of the toroidal scale factor.

$$\eta_{4,i}[\rho, \theta] = 2\eta_{3,i}[\rho, \theta] \approx \bar{\eta}_{4,i} \left(\frac{h_\phi}{R_0} \right) \tilde{n}_i \quad (5.16)$$

and $\bar{\eta}_{4,i} = \frac{\bar{n}_i \bar{T}_i}{\bar{\Omega}_i}$. The plasma considered in this analysis is predominantly in a

“collisionless” regime, where, $\hat{v}_{i,i} \ll 1$ [Figure 1]. Thus, the poloidal dependence of the collisionality interpolation function can be well approximated by the square of the density variations [Appendix B].

$$f_i = \bar{f}_i \tilde{n}_i^2 \quad (5.17)$$

This allows the poloidal dependence of the parallel viscosity coefficient can then be written as:

$$\eta_{0,i} = \bar{\eta}_{0,i} \tilde{n}_i^2 = \bar{\eta}_{0,i} (1 + 2n_s \sin \theta + 2n_c \cos \theta + \dots) \quad (5.18)$$

where the mean value is $\bar{\eta}_{0,i} = 2 \frac{\bar{n}_i \bar{T}_i}{\bar{v}_{i,i}} \bar{f}_i$, and $\bar{f}_i = \frac{\varepsilon^{-3/2} \hat{v}_{i,i}^2}{(1 + \varepsilon^{-3/2} \hat{v}_{i,i})(1 + \hat{v}_{i,i})}$.

5.3. Determining radially dependent plasma properties from experimental measurements

In order to develop a system of equations that can be used to solve for the poloidal asymmetries, mean values for densities, velocities, temperatures, particle and momentum sources, and the electric field must be determined. Measurements are available for the radial variations of poloidal and toroidal velocity, density, and temperature for this shot, and the ONETWO code can be used to set particle and momentum sources. From these measurements and calculations, the mean electric potential ($\bar{\Phi}$) can be initialized using the FSA of the continuity equations for both species Eq. (5.2), and the radial velocity (\bar{V}_r) can be calculated using the FSA of the composite radial momentum balance equation Eq. (5.3).

For Shot 149468 at 1905 ms, measurements of the carbon and deuterium mean velocity profiles [Figure 26], and mean densities for carbon, deuterium and electrons [Figure 27] are taken from experiment [16].

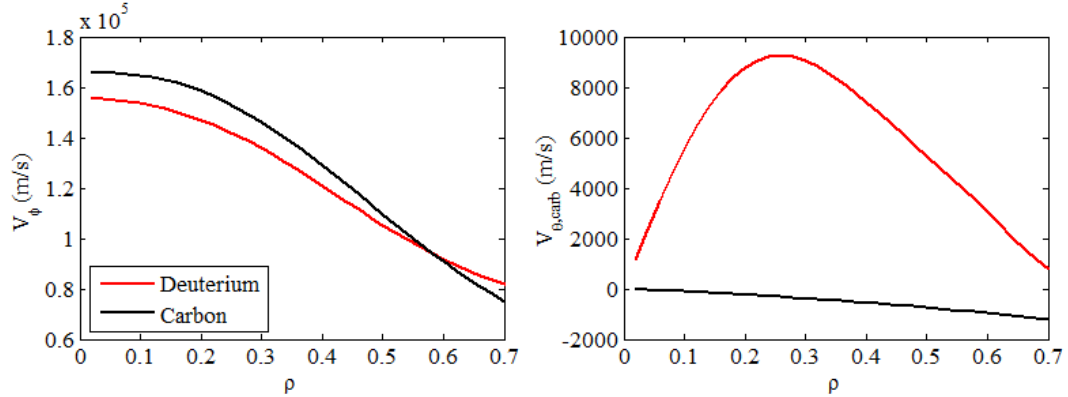


Figure 26: Measurements of Toroidal Velocities (left) and Poloidal Velocities (right) for Deuterium (red) and Carbon (black) in Shot 149468 at 1905 ms.

In addition, the ONETWO code is used to calculate radial profiles of toroidal torque from neutral-beam injection for deuterium ($R \cdot S_d^1$), and radial profiles for deuterium particle sources from the beam and the wall (S_d^0) [Figure 27] [17]. External carbon sources of torque and particles are assumed to be negligible in the central plasma considered in this analysis.

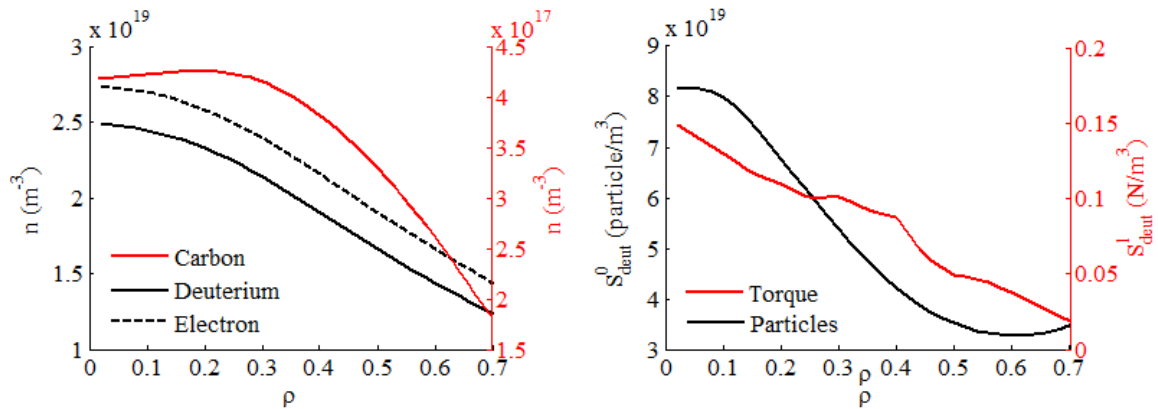


Figure 27: Density measurements for Deuterium, Carbon, and Electrons (left) and ONETWO calculations of external particle and momentum sources for Deuterium (right). Black profiles plotted against left axes, red profiles plotted against right axes.

The flux-surface-averaged continuity equation [Eq. (5.2)] relates the radial velocity to the density and particle sources. Assuming that the radial particle velocity has

no poloidal dependence [Eq. (5.12)], the continuity equation can be formatted into a differential equation in \bar{V}_r .

$$\frac{\partial \bar{V}_{r,i}}{\partial \rho} \left\langle \frac{n_i}{h_\rho} \right\rangle + \bar{V}_{r,i} \left\langle \frac{1}{h_\theta h_\rho h_\phi} \frac{\partial [n_i h_\theta h_\phi]}{\partial \rho} \right\rangle = \langle S_i^0 \rangle \quad (5.19)$$

In the shot considered in this analysis, the only significant particle source for the central plasma ($\rho < 0.7$) is from deuterium, sourced to the plasma by neutral-beam injection. The profile for deuterium \bar{V}_r can be determined by solving Eq.(5.19) using an integrating factor [Eq. (5.20)].

$$I = e^{\int_{\rho'=0}^{\rho} \left\langle \frac{1}{h_\theta h_\rho h_\phi} \frac{\partial [n_i h_\theta h_\phi]}{\partial \rho'} \right\rangle \left\langle \frac{n_i}{h_\rho} \right\rangle^{-1} d\rho'} \quad (5.20)$$

The radial profile for $\frac{\partial \bar{\Phi}}{\partial \rho}$ is directly calculated from the composite radial momentum balance, constructed by adding Eq. (5.3) for both deuterium and carbon. After expanding the electric potential using Eq. (5.11), the gradient of the mean potential can be factored out of the FSA operation.

$$\frac{\partial \bar{\Phi}}{\partial \rho} \left\langle \frac{\tilde{\Phi}}{h_\rho} (e_i n_i + e_j n_j) \right\rangle = - \left\langle \frac{1}{h_\rho} \left(\frac{\partial [p_i]}{\partial \rho} + \frac{\partial [p_j]}{\partial \rho} \right) \right\rangle + \left\langle B_\phi (e_i n_i V_{\theta,i} + e_j n_j V_{\theta,j}) \right\rangle - \left\langle B_\theta (e_i n_i V_{\phi,i} + e_j n_j V_{\phi,j}) \right\rangle \quad (5.21)$$

Equation (5.21) can be used to directly solve for the radial gradient of electric potential; i.e., the radial electrostatic field. The mean potential profile can be calculated by using a Simpson's-rule numeric integration, with potential on the plasma boundary constrained to zero.

CHAPTER 6

CALCULATION METHODOLOGY AND RESULTS

The plasma equations of Section 5.1, applicable throughout the central tokamak plasma within the $q = 2$ rational surface ($\rho < 0.7$), are used to construct a model to predict poloidal asymmetries in electric potential, density, and poloidal and toroidal components of velocity. A MATLAB [18] fitting program designed to automatically calculate from EFIT output files the formalism needed to analytically represent scale factors and magnetic field distributions for any of the plasma models discussed in Section 0 is applied to fit the Asymmetric Miller geometry, and to fit experimental and ONETWO radial profiles and gradients of plasma mean-values. A separate Mathematica [19] program is applied which automates the process of deriving of a set of coupled nonlinear equations from the basic plasma continuity and momentum balance equations introduced in Section 0, using the techniques described in Section 0. Mathematica writes the results of this derivation into text files, which are parsed using Python [20] into Fortran 90 [21] subroutines designed to calculate all coefficients for the set of nonlinear equations from the fitted data outputted by the MATLAB fitting-program. Finally, a Fortran code which utilizes both these Mathematica-generated subroutines and MATLAB generated input files of fitted data solves the coupled set of nonlinear plasma equations for the plasma asymmetries, using an iterative matrix-inversion technique.

These asymmetries describe the poloidal-variation of density, potential, and velocity in the plasma core necessary to satisfy the Fourier moments of the continuity and momentum balance equations. Performing the above-described analysis with scale factors set using the circular model significantly modifies the final predictions for plasma asymmetries. Additionally, although it may be simpler to calculate and apply only the non-orthogonal GFA covariant or contravariant scale factors rather than determine the OFA model values, analyses performed with these modifications to the AM scale factors changes the plasma equations and influences the resulting asymmetry predictions –

emphasizing the importance of proper application of the orthogonalization techniques outlined in Section 0.

6.1. MATLAB fitting-program for setting geometry and mean plasma parameters from experiment, ONETWO, and EFIT

Fitting of the Asymmetric Miller Orthogonalized Flux-surface Aligned (AM-OFA) model, determined in Section 4.6 to be the most effective method of representing the EFIT-determined plasma geometry, is performed using a MATLAB fitting program. The radial-profile fitting functions are also applied to fit radial profiles and determine gradients of experimental measurements and ONETWO outputs.

MATLAB routines calculate polynomial fits for radial profiles of the geometric quantities necessary to analytically represent the Asymmetric Miller model. From the Semi-Cartesian data returned by EFIT, 2D splines are used to determine contours of constant ψ , and from the positions of these contours determine ψ , F , and R_0 . The radial profiles for upper and lower triangularities and elongations for an Asymmetric Miller-model fit are then calculated the nonlinear convergence methods described in Section 4.5, and all resulting radial profiles are fitted using radially-dependent polynomials. Radial gradients through 3rd order are calculated at 50 radial locations, and resulting fits are written to text files to be used as inputs by the Fortran solution code.

These same MATLAB routines are applied to fit radial profiles and gradients to the experimentally measured mean-values of electron and ion temperatures, electron and ion densities, both the poloidal and the toroidal components of velocity for ions, and external deuterium momentum and particle sources [Figure 26, Figure 27]. The resulting fits of profiles and radial gradients through 2nd order are also written to input text files for the Fortran code.

Other plasma constants used in the Fortran calculations are determined from the MATLAB fits of EFIT output, or taken directly from the DIII-D database. The minor radius at the last-closed flux-surface ($a = 0.570$ m) is obtained from the MATLAB fit. The toroidal inductance variable VLOOP, used to set the toroidal electric field, and the plasma volume ($\bar{V} = 15.962$ m³) are taken directly from the DIII-D database.

6.2. Mathematica automated-derivation of a system of fourteen plasma asymmetry equations

The resulting plasma equations can be formulated into a coupled set of partial differential equations relating plasma density, velocities, and electric potential. Separation of variables is applied to reduce a subset of these 2D (r,theta) PDEs to a set of poloidally dependent ODEs at each of 50 radial locations. Representing the poloidal variations using Fourier series expansions, weighting the resulting equations by the Fourier basis functions ($\sin n\theta$, $\cos n\theta$), and taking the flux surface average to make use of orthogonality further reduces the set of ODEs to a coupled set of fourteen nonlinear equations relating the first order plasma asymmetries ($\Phi^{s,c}, n^{s,c}, V_p^{s,c}, V_t^{s,c}$) for both Deuterium and Carbon species.

A combination of Mathematica scripts are used to construct the bulk of the analytic formalism described in Sections 0, 0, 0, and Appendix A, and apply it to develop the set of plasma equations relating asymmetries within Mathematica. After expanding all the calculus-dependent portions of Equations (2.1)-(2.2) in terms of scale-factors, and substituting in the viscosity formalism outlined in Appendix A.3, the resulting partial differential equations are formatted entirely in terms of quantities with both radial and poloidal dependence, and their gradients in both radial and poloidal curvilinear directions. Applying separation of variables allows these PDEs to be reduced to poloidally-dependent ODEs, where values for all radial dependent terms are known. The expansions for the poloidal dependence of plasma variables [Eq. (5.11)] and other quantities that share these poloidal variations [Eqs. (5.13)-(5.18)] are inserted into the Mathematica equations, introducing fourteen unknown plasma asymmetries. Weighting the resulting equations by the Fourier basis functions ($\sin n\theta$, $\cos n\theta$) and taking the flux surface average to make use of orthogonality further reduces these ODEs to an overdetermined coupled set of nonlinear equations relating the fourteen first order plasma asymmetries ($\Phi^{s,c}, n^{s,c}, V_p^{s,c}, V_t^{s,c}$) for both Deuterium and Carbon species.

In order to manipulate these complex equations into forms that can be solved, each is fully expanded in Mathematica to collect and isolate all terms dependent on the variable asymmetries. The multipliers on these asymmetries are the FSA of quantities

comprised of known scale factors, magnetic fields, Fourier basis functions, and mean plasma quantities. This allows Mathematica to rewrite the plasma equations as the sum of terms comprised of only the fourteen asymmetries and flux-surface-averaged coefficients. The definitions for each of these coefficients, in terms of the scale factors and mean-values of measured or fitted plasma parameters, are stored separately. The resulting forms of the asymmetry equations are split apart to collect all terms that are nonlinear with respect to the asymmetries or independent of asymmetries into a nonlinear nonlinear source ($\vec{\mathbf{q}}[\vec{\mathbf{x}}]$). The final result is a linear system of fourteen equations ($\vec{\mathbf{A}}$) with fourteen unknown asymmetries ($\vec{\mathbf{x}}$).

$$\vec{\mathbf{A}} \vec{\mathbf{x}} = \vec{\mathbf{q}}[\vec{\mathbf{x}}] \quad (6.1)$$

$$\vec{\mathbf{x}} = [\tilde{\Phi}^{s,1}, \tilde{\Phi}^{c,1}, \tilde{n}_d^{s,1}, \tilde{n}_d^{c,1}, \tilde{n}_c^{s,1}, \tilde{n}_c^{c,1}, \tilde{V}_{\theta,d}^{s,1}, \tilde{V}_{\theta,d}^{c,1}, \tilde{V}_{\theta,c}^{s,1}, \tilde{V}_{\theta,c}^{c,1}, \tilde{V}_{\phi,d}^{s,1}, \tilde{V}_{\phi,d}^{c,1}, \tilde{V}_{\phi,c}^{s,1}, \tilde{V}_{\phi,c}^{c,1}]$$

This system of equations, constructed from the Fourier moments of the continuity equation and toroidal momentum balance for Deuterium and Carbon (8 equations) and the Fourier moments of the poloidal momentum balance for Deuterium, Carbon, and Electrons (6 equations), is written by Mathematica into output files, along with the definitions of the poloidally-dependent coefficients.

Python is used to parse Mathematica-generated output files containing the reformatted plasma equations into Fortran 90 subroutines. The formatted Mathematica equations are written to several output text files in the general structure of Fortran subroutines. Python parsing routines generate Fortran compliant subroutines from these output files. When incorporated into the full Fortran calculation code, these Mathematica/Python-generated subroutines compute the poloidally dependent coefficients for the plasma equations, perform the flux-surface averaging operation on these coefficients and other poloidally-dependent plasma parameters, solve differential equations constructed from the continuity and radial momentum balance equations for radial velocity and electric potential, solve the nonlinear set of plasma moment equations, and writes values of all radially and poloidally dependent Fortran variables and gradients to output files. This method of coupling the strengths of these languages allows changes in even the early stages of the analytic derivation portion of this analysis to be quickly

converted into Fortran and applied to the asymmetry calculations, while minimizing the possibility of human error during the derivation and coding process.

6.3. Fortran 90 solution code to calculate plasma asymmetries

The set of nonlinear equations developed in Mathematica is linearized, solved for asymmetries, and iterated until these asymmetries satisfy the set of plasma equations throughout the plasma using a Fortran solution code, and input files containing data fitted by MATLAB. These radially-dependent profiles of plasma asymmetries can be used to reconstruct the 2D variations of plasma potential, densities, and velocities.

The main Fortran input file contains the values of plasma constants, and the file-paths for the input files containing radial profiles of plasma parameters and gradients constructed by MATLAB. This input file contains options to allow the user to change which set of basis-vectors are used in the plasma equations, modify the forms of the plasma equations being used in the calculation, and set the convergence criteria for the iterative methods applied to solve the system of plasma moment equations. It also contains additional options to allow the particle and momentum sources to be approximated using the neutral-beam powers, as an approximation for profiles calculated using ONETWO.

The Fortran computation code sets all possible radial profiles of plasma parameters and geometric quantities from input files containing MATLAB fits, and calculates 2D distributions plasma parameters and geometric quantities dependent on these fits. It sets temperature profiles for both ion species from the read-in ion temperature profile, and sets the deuterium density profile and gradients \bar{n}_{deut} using \bar{n}_{elec} , \bar{n}_{carb} , and charge neutrality. These temperatures and densities are subsequently used to compute the pressure profiles ($\bar{p} = \bar{n} \bar{T}$) for both ion species. The most-probable thermal velocity $\bar{V}_{th} = \sqrt{\frac{2k\bar{T}}{m}}$ is also calculated for both ion species from the temperature profiles, and used in conjunction with the densities and temperatures to determine the mean-values for the collision frequencies ($\bar{\nu}$) using Eq. (2.7), the collisionality interpolation function (\bar{f}) from Eq. (5.17), and parallel and gyroviscous drag coefficients

$(\bar{\eta}_0, \bar{\eta}_{3,4})$ using Eqs. (5.18) and (5.16). Radial-profiles for the mean-values of the magnetic fields are computed from the fits of F and $\frac{\partial\psi}{\partial\rho}$ [Eq. (3.16)].

Two-dimensional distributions of geometric scale factors, magnetic fields, and gyrofrequencies are determined from the radially dependent parameters. Although the default execution mode for the Fortran code implements the AM-OFA model for geometry, the execution mode can be switched to use the FC model, or to use only the AM-GFA covariant or contravariant scale factors to set the Miller geometry. This portion of the calculation could be easily extended to include any of the other geometric models discussed in Section IV. The scale factors are used to calculate distributions for the components of the magnetic field using Eq. (3.17), field-curvature ratios [Eq. (3.37)], gyrofrequencies [Eq. (3.42)], particle sources [Eq.], and inductive electric field [Eq.].

After all of these experimentally-based plasma distributions are set in the Fortran code, the coefficients used to define the matrix-form of the system of fourteen plasma moment equations [Eq. (6.1)] are calculated and flux-surface averaged (FSA), and both the deuterium continuity [Eq. (5.19)] and the composite radial momentum balance [Eq. (5.21)] ordinary differential equations are solved numerically to determine radial profiles and gradients for both the radial component of velocity (\bar{V}_r) and mean electric potential ($\bar{\Phi}$). The flux-surface averages of the definitions for poloidally-dependent coefficients set from the Mathematica outputs are calculated numerically using a Simpson's rule poloidal integration. Fortran subroutines generated from Mathematica-formatted equations are used for all of these calculations, including the solutions to the differential equations for \bar{V}_r and $\bar{\Phi}$. When these profiles are initially calculated, the asymmetries in the composite radial momentum balance and deuterium continuity equations are set to zero. After these asymmetries are solved for, these two profiles will be updated, and this updating process will be iterated until the final profiles of \bar{V}_r and $\bar{\Phi}$ become consistent with the calculated asymmetries [Appendix C.2].

Finally, the set of core Fortran subroutines generated by Mathematica calls a LAPACK routine to solve the linearized system of moment equations for asymmetries [Eq. (6.1)]. The resulting asymmetries are used to update the nonlinear source $\vec{q}[\vec{x}]$ in the

system of plasma equations, and this process is iterated until the nonlinear system of equations constructed from the flux-surface averaged Fourier moments of the plasma equations converges for all fourteen asymmetries on all flux surfaces within the $q = 2$ rational surface, around $\rho < 0.7$. Because this analysis does not consider sources of carbon impurities from the edge, no attempt is made to solve for plasma asymmetries in the edge region, with > 2 ($\rho > 0.7$).

After the outer iteration between the subroutine used to compute asymmetries and that which calculates \bar{V}_r and $\bar{\Phi}$ profiles converges, the resulting plasma parameters satisfy a total of sixteen plasma equations. Normalized residuals for these equations converge to less than 10^{-4} for all fourteen Fourier moment equation used to calculate the asymmetries, and for both the composite radial momentum balance and the deuterium continuity equation. Most residuals are much smaller, closer to the limits of double precision computing at $\sim 10^{-15} - 10^{-10}$, as shown in Figure 28.

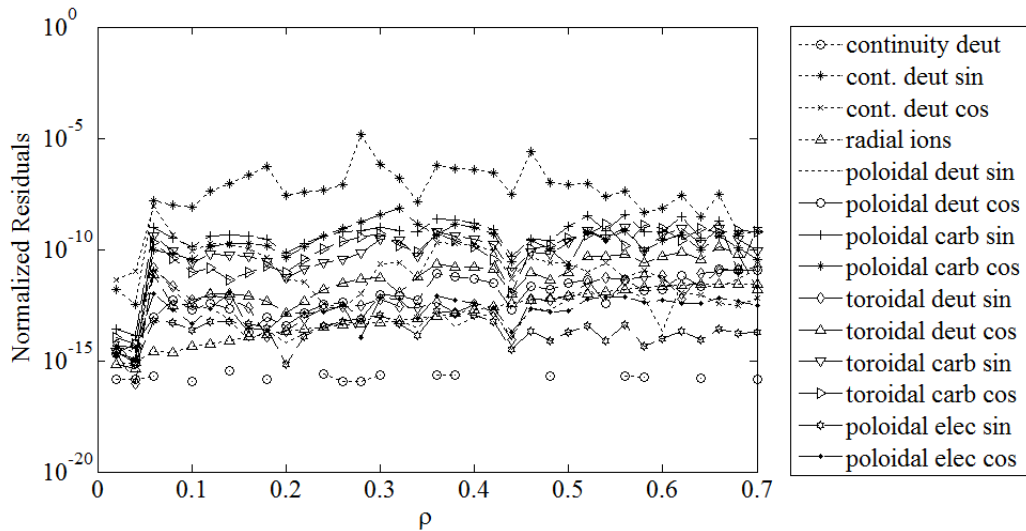


Figure 28: The system of sixteen plasma equations is converged at each radial location within the $q = 2$ flux surface ($\rho = 0.7$) until all normalized residuals are less than 0.01%

6.4. Results, and analysis of the effects of modifications to the geometry model

The Fortran code calculates radial profiles for radial velocity, electric potential, converged asymmetries for potential, density, and velocities, and 2D distributions of several other plasma quantities. The default method of execution uses orthogonalized asymmetric Miller (AM-OFA) scale factors to formulate the plasma equations, however,

to illustrate the effects of the geometry model on the results, comparative calculations of all quantities are performed using a Flux-surface equivalent Circular (FC) model. Additionally, the effects of using only covariant or only contravariant scale factors on the Miller-model results are shown.

Changes to the scale factors have the immediate effect of modifying the plasma differential volume element, which influences the calculations of the flux-surface volumes (∇_ρ) [Eq. (3.40)]. The FC model flux surfaces volumes are too large throughout the plasma, especially towards the plasma edge. The flux surfaces computed using the AM-GFA covariant scale factors and those calculated using AM-GFA contravariant scale factors have flux surfaces with volumes larger and smaller than the default AM-OFA flux surfaces. As expected considering its low positional error, the AM-OFA flux-surface volumes match very well with those calculated from EFIT using spline fits.

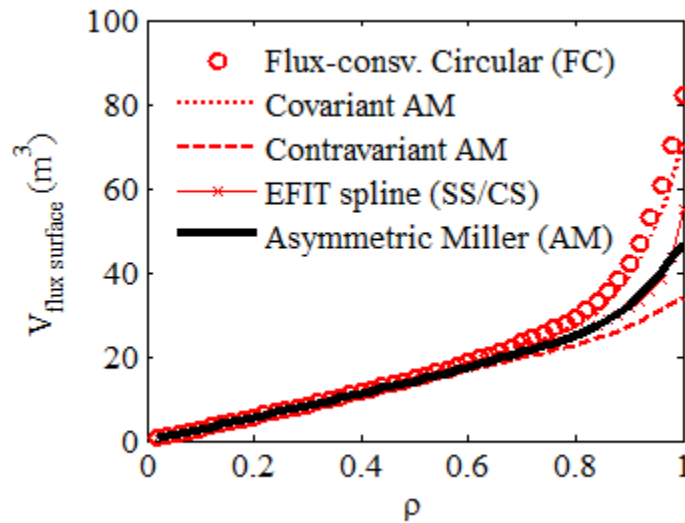


Figure 29: Flux-surface volume ($\nabla_\rho d\rho$) comparisons between plasma models. [Eq. (3.40)]

The volume changes of Figure 29 are consistent with the definitions for covariant and contravariant basis vectors shown in Figure 7; covariant scale factors are the edges of the parallelepiped volume element, and the volume element of a covariant-covariant system will be the product of the edges. This product will be larger than the true volume

determined by the cross-product of the covariant basis vectors, just as the product of the two vectors scaled by the smaller contravariant scale factors will be smaller than the true volume.

The accuracy of the geometric models at representing the plasma volume can be checked against a Monte-Carlo volume calculation, which samples 10^8 positions within a Cartesian box containing the model plasma. The Monte-Carlo calculations match the volume obtained by integrating the differential volume elements for the FC and AM-OFA systems over the full range of toroidal, poloidal, and radial locations [Table 11]. The AM model volume calculated by integration while using only covariant scale factors is too large for agreement, at 18.240 m^3 , and the volume using only contravariant scale factors is too small, at 14.430 m^3 – both of these discrepancies show how failure to correctly perform the Orthogonalization methods leads to differential volume elements which do not correctly integrate to the full plasma volume.

Table 11: Comparison of Monte-Carlo calculated plasma volumes with volumes obtained by integrating differential volume elements over the full variable phase space.

Model	Integrated Volume	Monte-Carlo Volume
EFIT	15.962	-
Flux-equivalent Circular (FC)	19.306	19.308 ± 0.006
Asymmetric Miller Orthogonal Flux Surface Aligned (AM-OFA)	16.009	16.005 ± 0.005
Covariant Asymmetric Miller General Flux-Surface Aligned (Con. AM-GFA)	18.240	16.005 ± 0.005
Contravariant Asymmetric Miller General Flux-Surface Aligned (Co. AM-GFA)	14.430	16.005 ± 0.005

In all geometry models, the asymmetries in plasma properties have only quadratic effects on the radial profiles for electric potential and radial deuterium velocity calculated from the radial ion momentum balance and deuterium continuity equations [Appendix C.2]. Consequently, the final V_r and Φ profiles calculated using the orthogonalized Asymmetric Miller (AM-OFA) geometry are only slightly different from profiles

resulting from the FC formulated equations. [Figure 30]. The difference from using only covariant or only contravariant AM scale factors is even smaller.

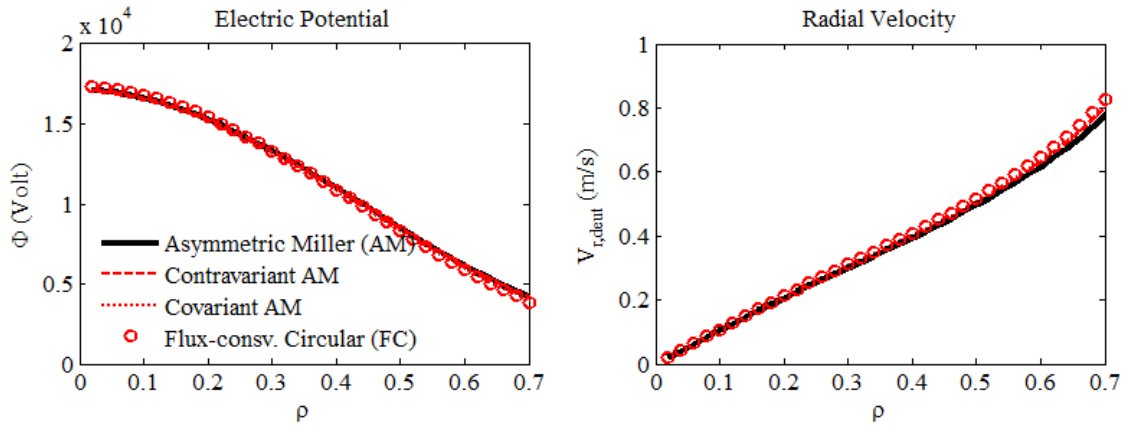


Figure 30: Electric Potential (left) and Radial Velocity (right) profiles, calculated using four separate geometric models. Default AM-OFA profiles shown as solid black lines.

The potential asymmetries calculated from the system of Fourier moment equations described in the previous section are very small, on the order of $10^{-4} - 10^{-3}$. They show a noticeable shift in radial profile around the $\rho = 0.3$ flux surface, which is reflected in all the other calculated asymmetry profiles. A significant difference in the sine asymmetry profiles results from applying the FC model, instead of the AM model.

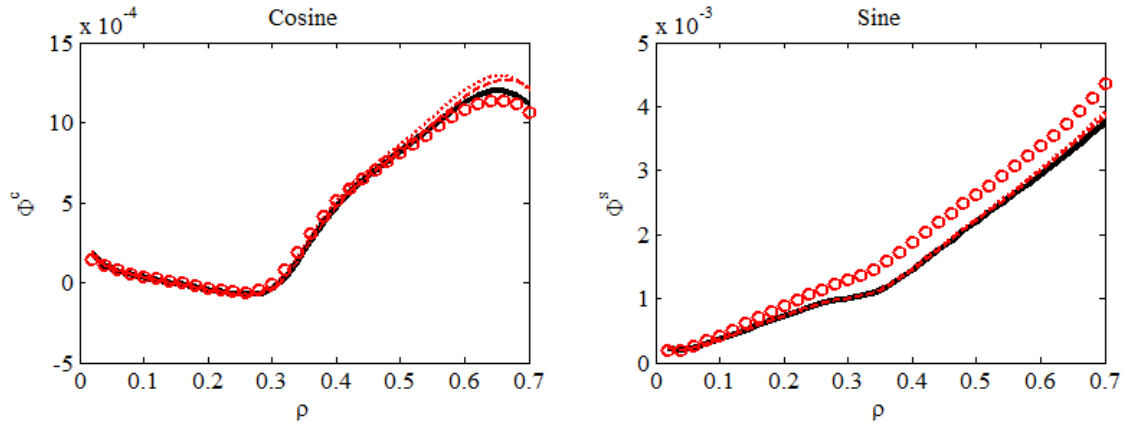


Figure 31: Electric Potential (Φ) Asymmetries, Cosine (LEFT) and Sine (RIGHT), calculated using four separate geometric models. Default AM-OFA profiles shown as solid black lines.

The density asymmetries are shaped similarly to the potential asymmetries, but are approximately an order of magnitude larger. The asymmetries in the Carbon density are two orders of magnitude larger than the Deuterium density asymmetries, especially farther away from the plasma center [Figure 32]. The AM density asymmetries are much

more pronounced than those calculated using the FC model, differing by over 30% for $\rho > 0.5$ in all but the deuterium sine asymmetries. While the covariant and contravariant AM asymmetries are noticeable, they are relatively small, with differences from AM-OFA remaining less than $\sim 5\%$.

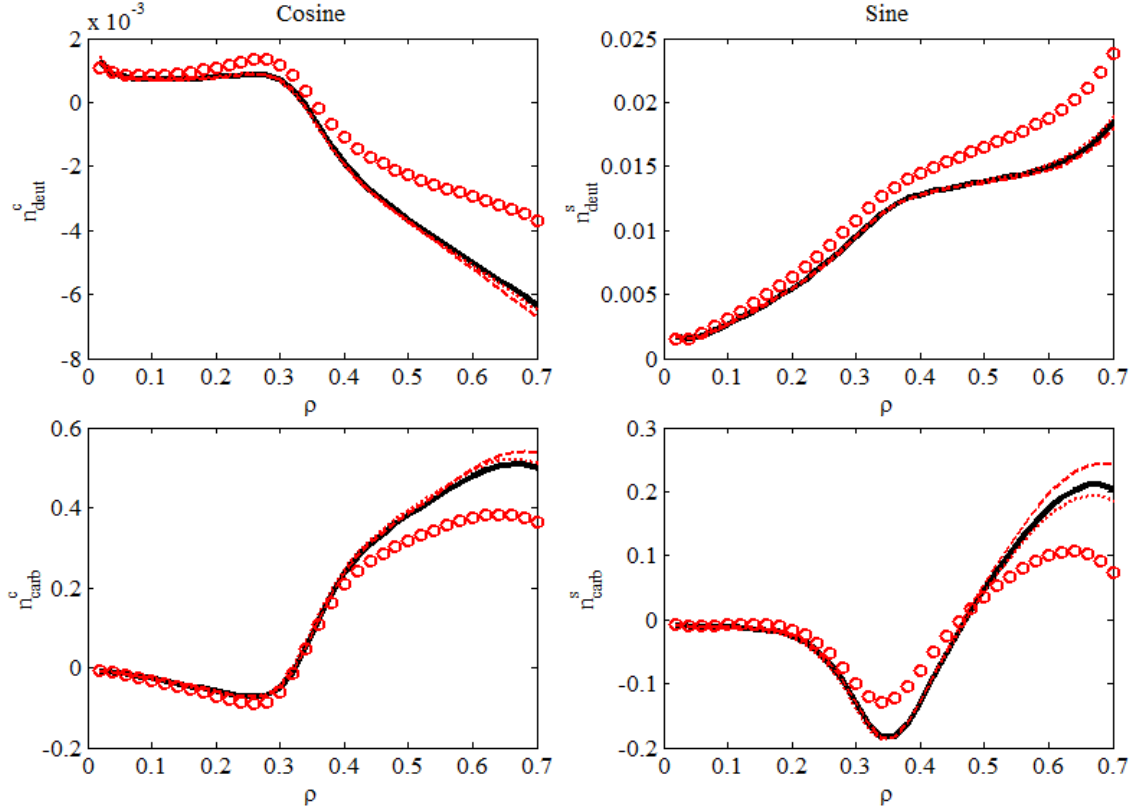


Figure 32: Density (n) Asymmetries, Cosine (LEFT) and Sine (RIGHT), for Deuterium (TOP) and Carbon (BOTTOM), calculated using four separate geometric models. Default AM-OFA profiles shown as solid black lines.

The asymmetries in poloidal velocity [Figure 33] differ between species, and are affected by the geometry model. Carbon V_θ asymmetries are over an order of magnitude larger than those for Deuterium, and are smaller when calculated using the FC model than when computed using variations of the AM model. In the Deuterium poloidal velocity asymmetries, applying only AM covariant scale factors or using the FC model can more than double the magnitudes of the asymmetries throughout most of the plasma.

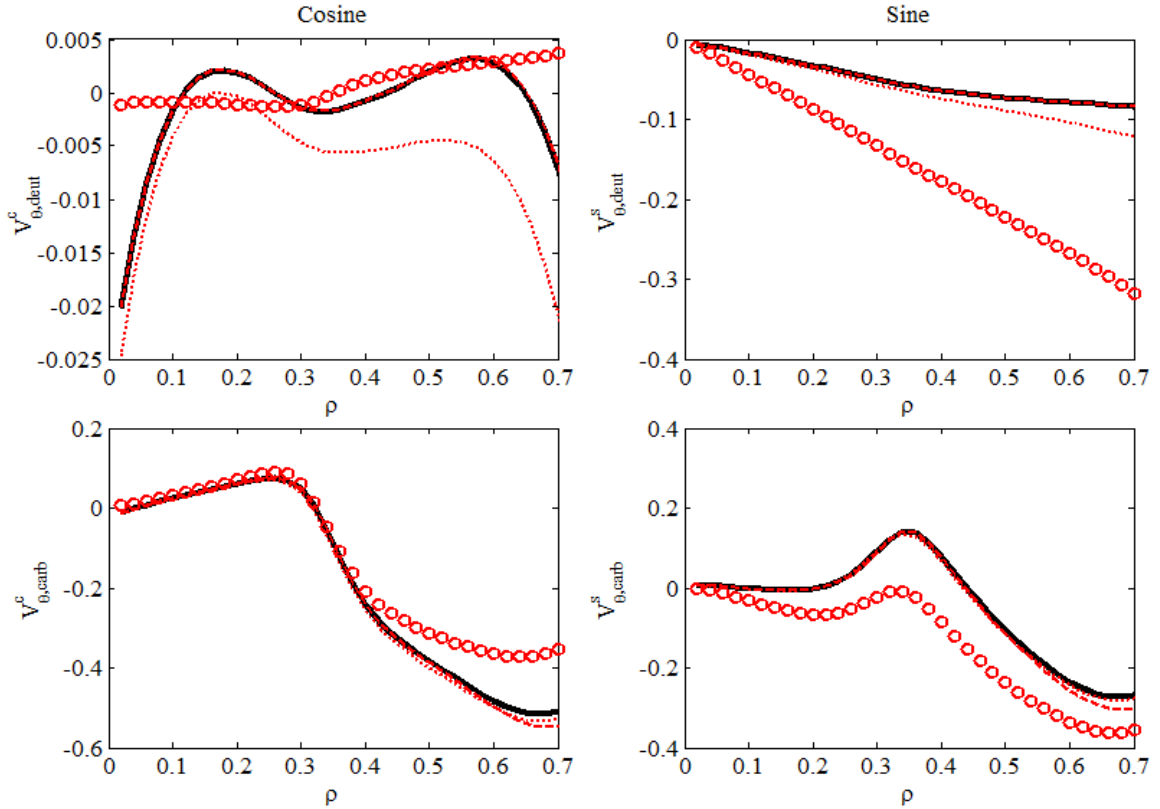


Figure 33: Poloidal velocity (V_{θ}) asymmetries, cosine (left) and sine (right), for Deuterium (top) and Carbon (bottom), calculated using four separate geometric models. Default AM-OFA profiles shown as solid black lines.

Toroidal velocity asymmetries show less variation between geometric models than poloidal velocity asymmetries. The most significant differences are between the AM-OFA and FC-OFA sine asymmetries. As the variations from the orthogonalized AM model caused by using only covariant or contravariant scale factors are small, $\sim 1\%$.

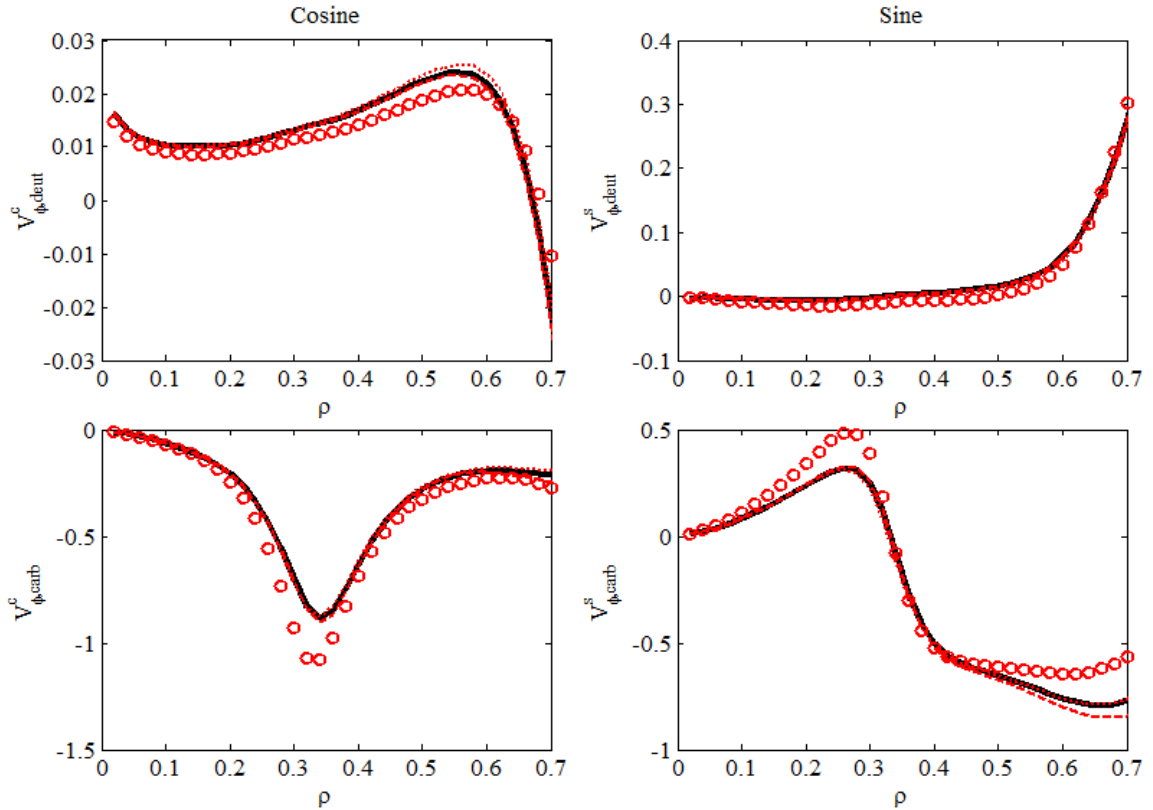


Figure 34: Toroidal velocity (V_ϕ) asymmetries, cosine (left) and sine (right), for Deuterium (top) and Carbon (bottom), calculated using four separate geometric models. Default AM-OFA profiles shown as solid black lines.

The asymmetries can be used to reconstruct distributions of the poloidal and radial variations in plasma quantities over the plasma cross-section. The small deuterium asymmetries cause the deuterium distributions to be largely symmetric about the plasma center, as can be seen in the deuterium density distribution [Figure 35, left]. However, the carbon density distribution is noticeably peaked towards the divertor region [Figure 35, right].

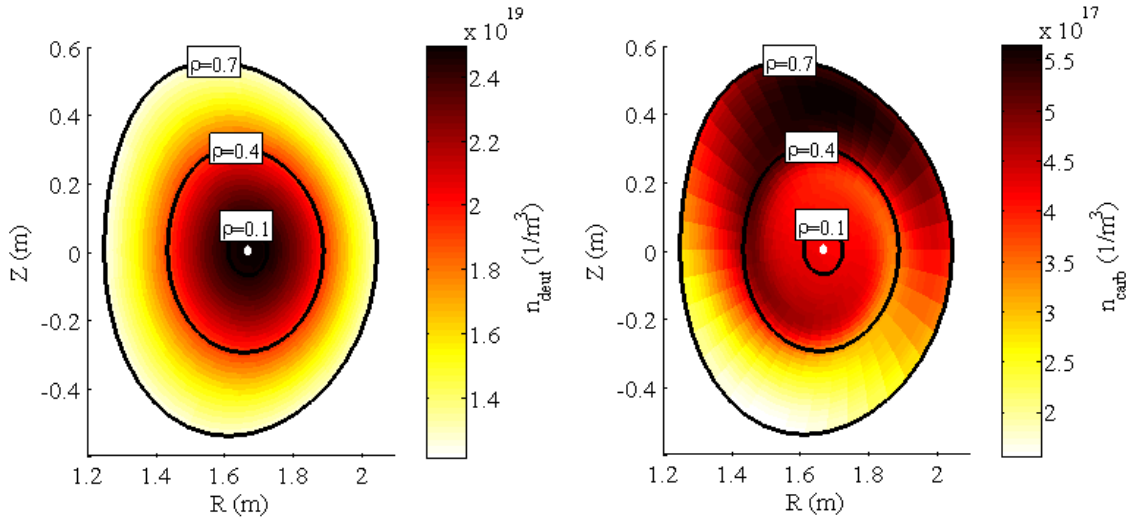


Figure 35: Predicted Deuterium and Carbon density distributions using the AM-OFA geometry model.

The Carbon poloidal and toroidal velocity distributions also show the effects of the large carbon asymmetries, generally requiring increased carbon velocities in the lower plasma hemisphere, corresponding to predictions for the region of lower density carbon [Figure 36]. Predictions for Carbon V_ϕ show an especially large up-down asymmetry near the plasma core, in the region $0.1 < \rho < 0.4$.

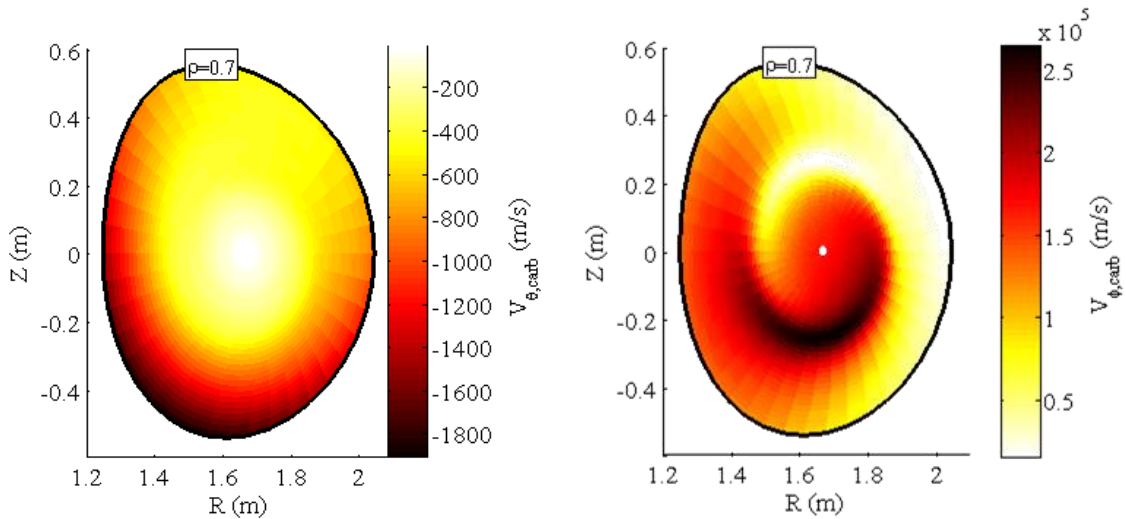


Figure 36: Predicted Carbon Poloidal (left) and Toroidal (right) Velocity distributions, using the AM-OFA geometry model.

Recent analyses have applied similar calculations of plasma asymmetries to predict components of poloidal and toroidal velocities from the flux-surface averaged toroidal and poloidal momentum balance equations [22]. In addition, traditional 1D neoclassical calculations have not been able to explain recent measurements of poloidal density, velocity, and radial electric field asymmetries in the plasma edge of the Alcator C-mod tokamak [23], suggesting that the extension of the 2D asymmetry calculation methods presented here may be helpful.

CHAPTER 7

CONCLUSIONS

From radial measurements of flux surface averaged plasma density, velocity, and external source and a Grad-Shafranov calculation of the variations in the magnetic field structure across a plasma cross-section, neoclassical rotation theory can be used to predict poloidal variations in plasma properties on flux surfaces. Fourier moments of the continuity equation and components of the momentum balance equations for Carbon and Deuterium in a realistic up-down asymmetric plasma can be used to calculate the poloidal variations in distributions of densities, velocities, and electric potential adhering to low-order Fourier expansions. Use of a realistic orthogonalized curvilinear coordinate system to represent the plasma geometry significantly influences these poloidal variations, as compared to the results obtained in identical analysis using the circular model.

In order to apply a curvilinear flux surface aligned model to calculate gradient operators in plasma equations formulated relative to flux-surfaces, it is important to use a system of orthogonalized basis vectors and scale factors developed from the general curvilinear system in order to correctly perform volume integrals. This is an additional complication that arises when the curvilinear system under consideration deviates from a toroidally symmetric circular-model, which does not require orthogonalization.

The Asymmetric Miller Orthogonalized Flux-surface Aligned Coordinate system is significantly more accurate than several alternative methods of equivalent complexity at representing the shape of EFIT-determined flux surfaces, while also requiring the smallest number of fitting coefficients. Although these alternative curvilinear systems are uniquely suited to modeling irregularly shaped plasmas and can be expanded to arbitrary accuracy at the price of a large increase in complexity, there are few practical situations in which the error in a model's representation of the poloidal magnetic field in the central plasma must be reduced below the $\sim 0.8\%$ attainable using the Asymmetric Miller model.

These calculations of poloidal asymmetries can be applied to update many calculations which rely on approximations for variations of the plasma properties on flux surfaces. More work needs to be done in order to expand this analysis to apply in the plasma edge region, extend the viscosity representation to include the effects of toroidal axisymmetry, and consider the effects of applying higher order Fourier expansions to represent the poloidal asymmetries in plasma properties. Accounting for radial gradients in the plasma asymmetries may also influence the calculation, although the increased complexity of the system of asymmetry equations resulting from this modification may require that the convergence method be updated to apply a nonlinear Newton's method.

APPENDIX A INERTIAL TERMS AND ELEMENTS OF THE VISCOSITY TENSOR

The Jacobian in orthogonalized curvilinear coordinates is $\mathcal{J} = h_\theta h_\rho h_\phi$

A.1 Expansion of Continuity Streaming Term in OFA Geometry

In the Continuity Equation, expanding the vector operations in the streaming term yields

$$\nabla \cdot \left(\vec{nV} \right) = \frac{1}{\mathcal{J}} \left(\frac{\partial \llbracket nV_r h_\theta h_\phi \rrbracket}{\partial \rho} + \frac{\partial \llbracket nV_\theta h_\rho h_\phi \rrbracket}{\partial \theta} \right) \quad (\text{A.1})$$

A.2 Expansion of Momentum and Torque Inertial Terms in OFA Geometry

Poloidal Momentum Balance:

$$\left(\hat{e}_\theta \cdot \nabla \cdot nm \vec{V} \vec{V} \right) = \frac{m}{\mathcal{J}} \left(\frac{1}{h_\theta} \frac{\partial \llbracket nV_\theta V_r h_\phi h_\theta^2 \rrbracket}{\partial \rho} + \frac{\partial \llbracket nV_\theta^2 h_\phi h_\rho \rrbracket}{\partial \theta} \right) - mn \left(\frac{V_r^2}{h_\rho h_\theta} \frac{\partial h_\rho}{\partial \theta} + \frac{V_\phi^2}{h_\rho h_\theta} \frac{\partial h_\phi}{\partial \theta} \right) \quad (\text{A.2})$$

Toroidal Angular Momentum Balance:

$$\left(R \hat{e}_\phi \right) \cdot \left(\nabla \cdot nm \vec{V} \vec{V} \right) = \frac{m}{\mathcal{J}} \left(\frac{\partial \llbracket V_\phi V_r n h_\phi^2 h_\theta \rrbracket}{\partial \rho} + \frac{\partial \llbracket V_\phi V_\theta n h_\phi^2 h_\rho \rrbracket}{\partial \theta} \right) \quad (\text{A.3})$$

A.3 Elements of the Viscosity Tensor in OFA Geometry

The elements of the stress tensor can be decomposed into parallel $\left(\Pi_{\alpha,\beta}^0 \right)$, perpendicular

$\left(\Pi_{\alpha,\beta}^{12} \right)$, and gyroviscous $\left(\Pi_{\alpha,\beta}^{34} \right)$ components:

$$\begin{aligned} \Pi_{\alpha,\beta} &= \Pi_{\alpha,\beta}^0 + \Pi_{\alpha,\beta}^{12} + \Pi_{\alpha,\beta}^{34} \\ &= -\eta_0 W_{\alpha,\beta}^0 - \left(\eta_1 W_{\alpha,\beta}^1 + \eta_2 W_{\alpha,\beta}^2 \right) + \eta_3 W_{\alpha,\beta}^3 + \eta_4 W_{\alpha,\beta}^4 \end{aligned} \quad (\text{A.4})$$

These tensor elements can be written in terms of viscosity coefficients $(\eta_0, \eta_1, \eta_2, \eta_3, \eta_4)$

and elements of the traceless rate-of-strain tensor for plasma under the influence of a

strong external magnetic field $\left(\vec{B} = (B_r, B_\theta, B_\phi) \right)$.

The elements of the traceless rate-of-strain tensor are

$$\begin{aligned}
W_{\alpha,\beta}^0 &= \sum_{\mu=1}^3 \sum_{\nu=1}^3 \left(\frac{3}{2} \left(f_\alpha f_\beta - \frac{1}{3} \delta_{\alpha,\beta} \right) \left(f_\mu f_\nu - \frac{1}{3} \delta_{\mu,\nu} \right) W_{\mu,\nu} \right) \\
W_{\alpha,\beta}^1 &= \sum_{\mu=1}^3 \sum_{\nu=1}^3 \left(\left((\delta_{\alpha,\mu} - f_\alpha f_\mu) (\delta_{\beta,\nu} - f_\beta f_\nu) + \frac{1}{2} (\delta_{\alpha,\beta} - f_\alpha f_\beta) f_\mu f_\nu \right) W_{\mu,\nu} \right) \\
W_{\alpha,\beta}^2 &= \sum_{\mu=1}^3 \sum_{\nu=1}^3 \left(\left((\delta_{\alpha,\mu} - f_\alpha f_\mu) f_\beta f_\nu + (\delta_{\beta,\nu} - f_\beta f_\nu) f_\alpha f_\mu \right) W_{\mu,\nu} \right) \\
W_{\alpha,\beta}^3 &= \sum_{\mu=1}^3 \sum_{\nu=1}^3 \sum_{\gamma=1}^3 \left(\frac{1}{2} \left((\delta_{\alpha,\mu} - f_\alpha f_\mu) \epsilon_{\beta,\gamma,\nu} + (\delta_{\beta,\nu} - f_\beta f_\nu) \epsilon_{\alpha,\gamma,\mu} \right) f_\gamma W_{\mu,\nu} \right) \\
W_{\alpha,\beta}^4 &= \sum_{\mu=1}^3 \sum_{\nu=1}^3 \sum_{\gamma=1}^3 \left(\frac{1}{2} \left(f_\alpha f_\mu \epsilon_{\beta,\gamma,\nu} + f_\beta f_\nu \epsilon_{\alpha,\gamma,\mu} \right) f_\gamma W_{\mu,\nu} \right)
\end{aligned} \tag{A.5}$$

Where $\delta_{\alpha,\beta}$ is the Kronecker delta function, $\epsilon_{\alpha,\beta,\gamma}$ is the antisymmetric unit tensor, and the elements of the general rate-of-strain tensor $W_{\alpha,\beta}$ can be defined in terms of the velocity and unit vectors for the GFA coordinate system:

$$W_{\alpha,\beta} = \left(\hat{e}_\alpha \cdot \nabla \vec{V} \cdot \hat{e}_\beta + \hat{e}_\beta \cdot \nabla \vec{V} \cdot \hat{e}_\alpha - \frac{2}{3} \delta_{\alpha,\beta} \nabla \cdot \vec{V} \right) \tag{A.6}$$

The magnetic field ratios in a tokamak can be ordered as

$$f_t = \left| \frac{B_\phi}{B} \right| \approx 1, \quad f_p = \left| \frac{B_\theta}{B} \right| \ll 1 \rightarrow f_p^2 \approx 0, \quad f_r = \left| \frac{B_r}{B} \right| \approx 0 \tag{A.7}$$

Because $V_r \ll V_\theta < V_\phi$, the radial component of velocity can be neglected in this

formalism. Assuming axisymmetry $\left(\frac{\partial}{\partial \phi} \approx 0 \right)$, and defining A_0 as:

$$A_0 \equiv 2 \left(-\frac{1}{3} \frac{h_\phi^2}{h_\rho} \frac{1}{h_\theta} \frac{\partial}{\partial \theta} \left[\frac{h_\rho}{h_\phi^2} V_\theta \right] + f_p \frac{h_\phi}{h_\theta} \frac{\partial}{\partial \theta} \left[\frac{V_\phi}{h_\phi} \right] \right) \tag{A.8}$$

the elements of the viscous stress tensor shown in Table 12 can be developed.

Table 12: Elements of the Viscosity Tensor, with $f_p = \left| \frac{B_\theta}{B} \right|$, $f_t = \left| \frac{B_\phi}{B} \right| \approx 1$, $\eta_2 = 4\eta_1$, and $\eta_4 = 2\eta_3$.

	<i>Parallel</i> $\Pi_{\alpha,\beta}^0 \equiv -\eta_0 W_{\alpha,\beta}^0$	<i>Perpendicular</i> $\Pi_{\alpha,\beta}^{12} \equiv -\eta_1 W_{\alpha,\beta}^1 - \eta_2 W_{\alpha,\beta}^2$	<i>Gyroviscous</i> $\Pi_{\alpha,\beta}^{34} \equiv \eta_3 W_{\alpha,\beta}^3 + \eta_4 W_{\alpha,\beta}^4$
$\Pi_{\rho,\rho}$	$\frac{1}{2}\eta_0 A_0$	$\eta_1 \frac{h_\rho}{h_\theta} \frac{\partial}{\partial \theta} \left[\frac{V_\theta}{h_\rho} \right]$ $-f_p \eta_1 \frac{h_\phi}{h_\theta} \frac{\partial}{\partial \theta} \left[\frac{V_\phi}{h_\phi} \right]$	$-\eta_3 \frac{h_\theta}{h_\rho} \frac{\partial}{\partial \rho} \left[\frac{V_\theta}{h_\theta} \right]$ $+f_p \eta_3 \frac{h_\phi}{h_\rho} \frac{\partial}{\partial \rho} \left[\frac{V_\phi}{h_\phi} \right]$
$\Pi_{\rho,\theta} = \Pi_{\theta,\rho}$	0	$-\eta_1 \frac{h_\theta}{h_\rho} \frac{\partial}{\partial \rho} \left[\frac{V_\theta}{h_\theta} \right]$ $+f_p (\eta_1 - \eta_2) \frac{h_\phi}{h_\rho} \frac{\partial}{\partial \rho} \left[\frac{V_\phi}{h_\phi} \right]$	$-\eta_3 \frac{h_\rho}{h_\theta} \frac{\partial}{\partial \theta} \left[\frac{V_\theta}{h_\theta} \right]$ $+f_p \left(\eta_3 - \frac{\eta_4}{2} \right) \frac{h_\phi}{h_\theta} \frac{\partial}{\partial \theta} \left[\frac{V_\phi}{h_\phi} \right]$
$\Pi_{\rho,\phi} = \Pi_{\phi,\rho}$	0	$-\eta_2 \frac{h_\phi}{h_\rho} \frac{\partial}{\partial \rho} \left[\frac{V_\phi}{h_\phi} \right]$ $+f_p (\eta_1 - \eta_2) \frac{h_\theta}{h_\rho} \frac{\partial}{\partial \rho} \left[\frac{V_\theta}{h_\theta} \right]$	$-\frac{\eta_4}{2} \frac{h_\theta}{h_\rho} \frac{\partial}{\partial \theta} \left[\frac{V_\phi}{h_\phi} \right]$ $+f_p \left(\eta_3 \frac{h_\rho}{h_\theta} \frac{\partial}{\partial \theta} \left[\frac{V_\theta}{h_\rho} \right] - \eta_4 \frac{h_\phi}{h_\theta} \frac{\partial}{\partial \theta} \left[\frac{V_\theta}{h_\phi} \right] \right)$
$\Pi_{\theta,\theta}$	$\frac{1}{2}\eta_0 A_0$	$-\eta_1 \frac{h_\rho}{h_\theta} \frac{\partial}{\partial \theta} \left[\frac{V_\theta}{h_\rho} \right]$ $+f_p (\eta_1 - 2\eta_2) \frac{h_\phi}{h_\theta} \frac{\partial}{\partial \theta} \left[\frac{V_\phi}{h_\phi} \right]$	$\eta_3 \frac{h_\theta}{h_\rho} \frac{\partial}{\partial \rho} \left[\frac{V_\theta}{h_\theta} \right]$ $+f_p (\eta_4 - \eta_3) \frac{h_\phi}{h_\rho} \frac{\partial}{\partial \rho} \left[\frac{V_\phi}{h_\phi} \right]$
$\Pi_{\theta,\phi} = \Pi_{\phi,\theta}$	$-\frac{3}{2}f_p \eta_0 A_0$	$-\eta_2 \frac{h_\phi}{h_\theta} \frac{\partial}{\partial \theta} \left[\frac{V_\phi}{h_\phi} \right]$ $+f_p \left(\eta_1 \frac{h_\rho}{h_\theta} \frac{\partial}{\partial \theta} \left[\frac{V_\theta}{h_\rho} \right] - 2\eta_2 \frac{h_\phi}{h_\theta} \frac{\partial}{\partial \theta} \left[\frac{V_\theta}{h_\phi} \right] \right)$	$\frac{\eta_4}{2} \frac{h_\theta}{h_\rho} \frac{\partial}{\partial \rho} \left[\frac{V_\phi}{h_\phi} \right]$ $+f_p \left(\frac{\eta_4}{2} - \eta_3 \right) \frac{h_\theta}{h_\rho} \frac{\partial}{\partial \rho} \left[\frac{V_\theta}{h_\theta} \right]$
$\Pi_{\phi,\phi}$	$-\eta_0 A_0$	$2f_p \eta_2 \frac{h_\phi}{h_\theta} \frac{\partial}{\partial \theta} \left[\frac{V_\phi}{h_\phi} \right]$	$-f_p \eta_4 \frac{h_\theta}{h_\rho} \frac{\partial}{\partial \rho} \left[\frac{V_\phi}{h_\phi} \right]$

A.4 Expansion of Momentum and Torque Viscous Terms in OFA Geometry

Poloidal Momentum Balance:

$$\left(\hat{e}_\theta \cdot \nabla \cdot \ddot{\Pi} \right) = \frac{1}{\mathcal{J}} \left(\frac{1}{h_\theta} \frac{\partial [\Pi_{r,\theta} h_\theta^2 h_\phi]}{\partial \rho} + \frac{\partial [\Pi_{\theta,\theta} h_\rho h_\phi]}{\partial \theta} \right) - \left(\frac{\Pi_{r,r}}{h_\theta h_\rho} \frac{\partial h_\rho}{\partial \theta} + \frac{\Pi_{\phi,\phi}}{h_\theta h_\phi} \frac{\partial h_\phi}{\partial \theta} \right) \quad (\text{A.9})$$

Toroidal Angular Momentum Balance:

$$(R\hat{e}_\phi) \times (\hat{e}_\phi \cdot \nabla \cdot \ddot{\Pi}) = \frac{1}{\mathcal{J}} \left(\frac{\partial \llbracket h_\phi^2 h_\rho \Pi_{\theta, \phi} \rrbracket}{\partial \theta} + \frac{\partial \llbracket h_\phi^2 h_\theta \Pi_{r, \phi} \rrbracket}{\partial \rho} \right) \quad (\text{A.10})$$

APPENDIX B SIMPLIFICATION OF THE PFIRSCH-SCHLUTER VISCOSITY INTERPOLATION FUNCTION FOR LOW COLLISIONALITY PLASMA

In order to represent the poloidal dependence in the parallel viscosity coefficient, the poloidal dependence in the Pfirsch-Schluter – banana plateau viscosity interpolation formula must be isolated. Applying Eqs. (5.14) and (5.10) to expand the poloidal dependence of the drag frequency in Eq. (2.11) in terms of \bar{n}_i , and assuming that ε and q are flux-surface dependent values, the viscosity interpolation function can be rearranged to the form

$$f_i = \frac{\varepsilon^{-3/2} v_{i,i}^{*2}}{(1 + \varepsilon^{-3/2} v_{i,i}^*)(1 + v_{i,i}^*)} = \frac{\varepsilon^{-3/2} \hat{v}_{i,i}^2 (1 + \varepsilon \bar{n}_i)^2}{\left(1 + \varepsilon^{-3/2} \hat{v}_{i,i} (1 + \varepsilon \bar{n}_i)\right) \left(1 + \hat{v}_{i,i} (1 + \varepsilon \bar{n}_i)\right)} \quad (\text{B.1})$$

which, after dividing through top and bottom by $(\varepsilon^{-3/2} \hat{v}_{i,i}^2)$, becomes

$$f_i = \frac{(1 + \varepsilon \bar{n}_i)^2}{\left(1 + \frac{\varepsilon^{3/2}}{\hat{v}_{i,i}} + \varepsilon \bar{n}_i\right) \left(1 + \frac{1}{\hat{v}_{i,i}} + \varepsilon \bar{n}_i\right)} \quad (\text{B.2})$$

The poloidal dependence of Eq. (B.2) is isolated to the \bar{n}_i terms. With some rearranging, the poloidal dependence can be separated from the radially-dependent portion and written as a product of series expansions, using an inverse binomial expansion.

$$f_i = \bar{f}_i (1 + \varepsilon \bar{n}_i)^2 \left(1 - \varepsilon \bar{g}_{i,3/2} + \varepsilon^2 \bar{g}_{i,3/2}^2 - \dots\right) \left(1 - \varepsilon \bar{g}_{i,1} + \varepsilon^2 \bar{g}_{i,1}^2 - \dots\right) \quad (\text{B.3})$$

where

$$\bar{g}_{i,1} = \bar{n}_i \left(1 + \frac{1}{\hat{v}_{i,i}}\right)^{-1}, \quad \bar{g}_{i,3/2} = \bar{n}_i \left(1 + \frac{\varepsilon^{3/2}}{\hat{v}_{i,i}}\right)^{-1} \quad (\text{B.4})$$

and \bar{f} is defined in Eq. (5.17). This form is valid for regimes where $\hat{v}_{i,i} \lesssim 1$.

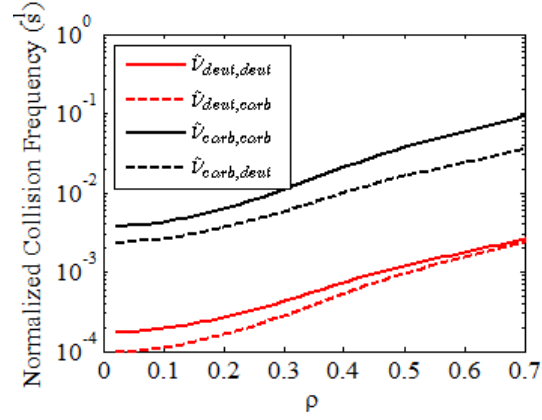


Figure 37: Normalized collision frequencies ($\hat{\nu}$) for Shot# 149468 at 1905 ms.

The plasma considered in this analysis is predominantly in a “collisionless” regime, where, $\hat{v}_{i,i} \ll 1$ [Figure 37]. Consequently, $\check{g}_{i,1} \rightarrow \check{g}_{i,3/2} \rightarrow 0$, and the poloidal dependence of the parallel viscosity reduces to the square of the density variations.

$$f_i = \bar{f}_i \tilde{n}_i^2 \quad (\text{B.5})$$

APPENDIX C FIGURES

C.1 Curvilinear Model Basis Vector Orientations

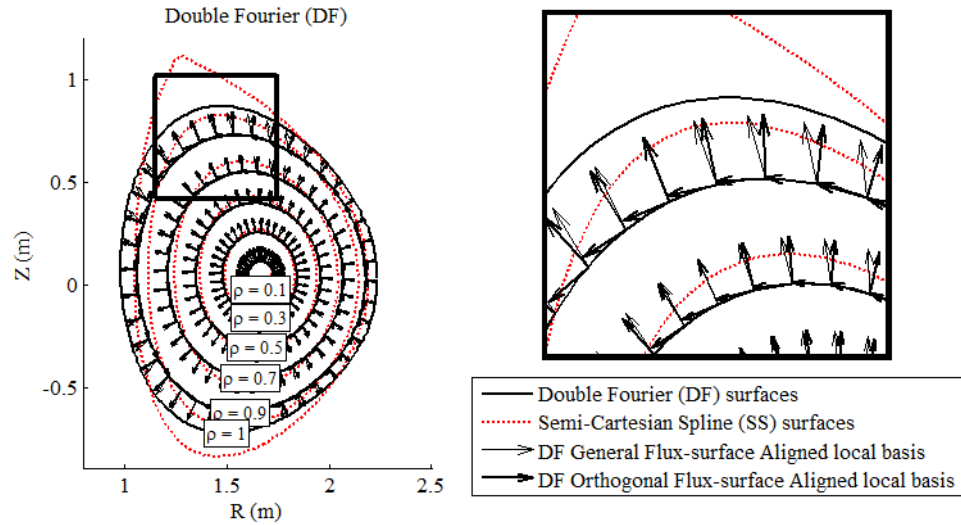


Figure 38: Basis vectors determined by analytic expressions for gradients of a position vector with poloidal variations in both major radius (R) and vertical displacement (Z) represented using 2nd order Fourier expansions. Requires nine coefficients to be fitted from the Semi-Cartesian ψ distribution

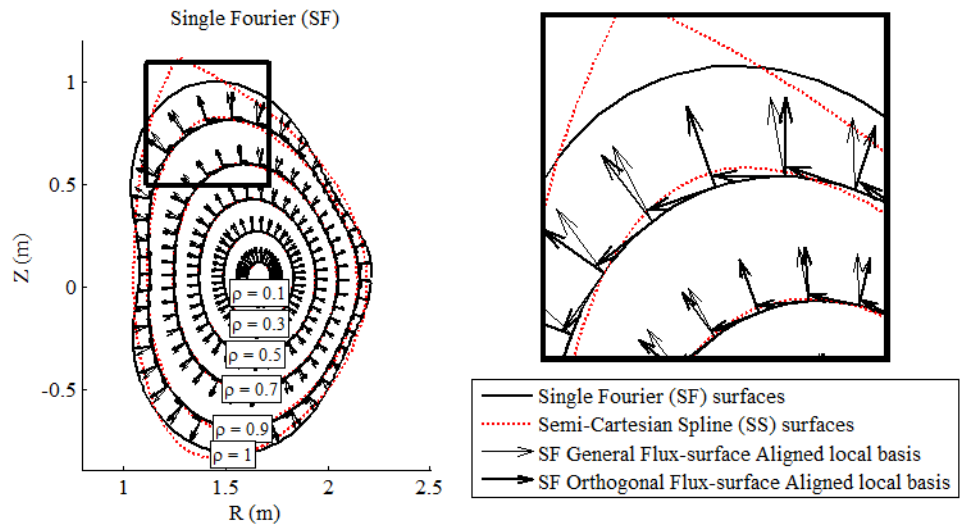


Figure 39: Basis vectors determined by analytic expressions for gradients of a position vector with poloidal variations in minor radius (r) represented using a 4th order Fourier expansion. Requires ten coefficients to be fitted from the Semi-Cartesian ψ distribution

C.2 Effects of Asymmetries on Radial Velocities and Electric Potential Calculations

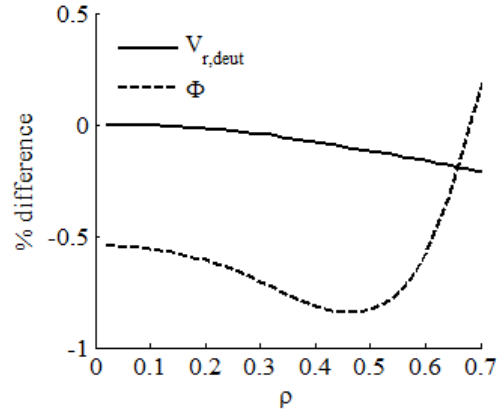


Figure 40: Percent difference in Φ and V_r profiles calculated while neglecting asymmetries in Eq.(5.19) and Eq.(5.21), as compared to calculations which include asymmetries.

C.3 Calculations of 2D distributions of plasma properties, using the Orthogonalized Asymmetric Miller geometry model

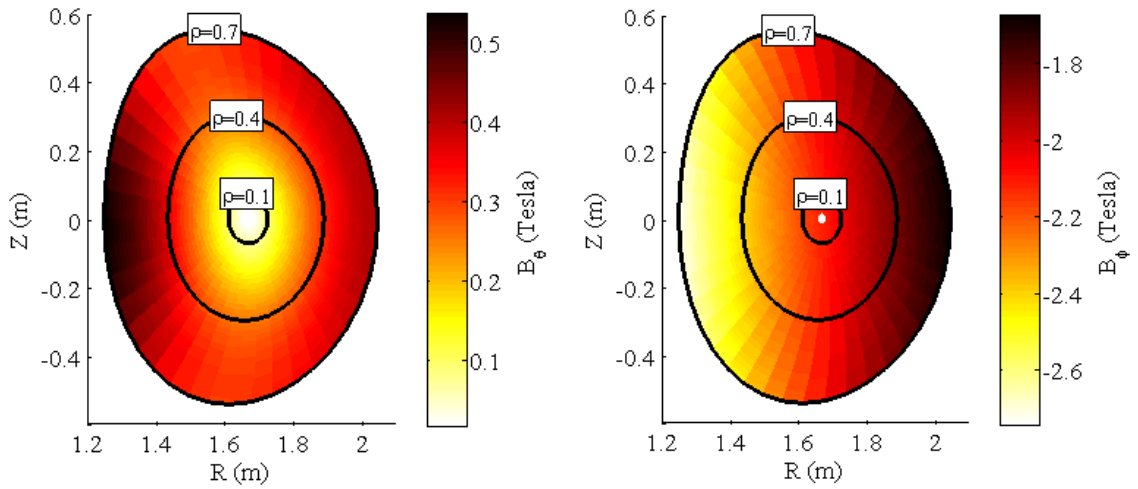


Figure 41: Poloidal (left) and Toroidal (right) Components of the Magnetic Field

$$\vec{B} = B_\theta \hat{e}_\theta + B_\phi \hat{e}_\phi$$

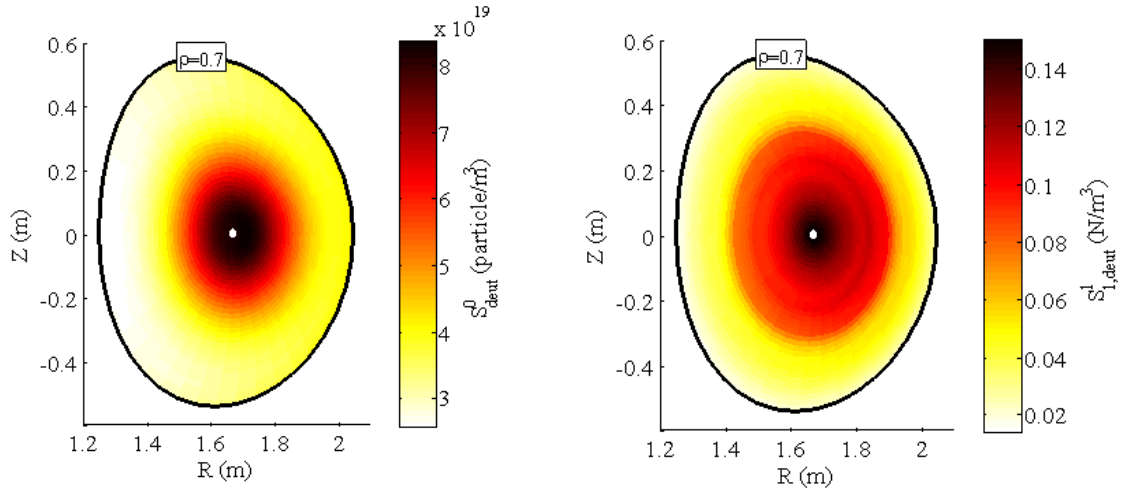


Figure 42: Sources of Deuterium particles (left) and toroidal momentum (right), from neutral beam injection.

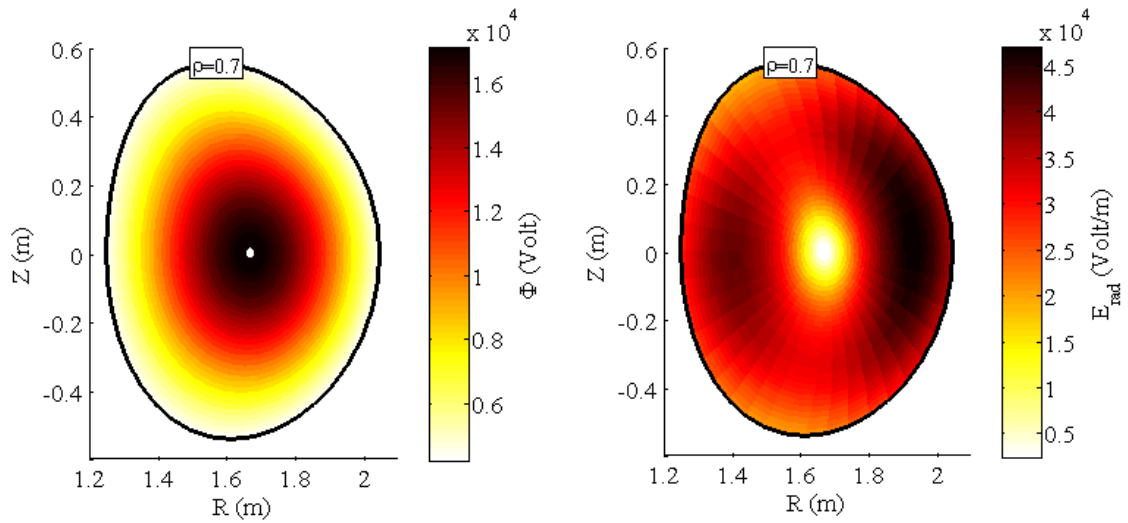


Figure 43: Distributions for Electric Potential (Φ) (left) and radial component of the Electric Field

$$\left(E_r = \frac{1}{h_\rho} \frac{\partial \Phi}{\partial \rho} \right) \text{ (right)}$$

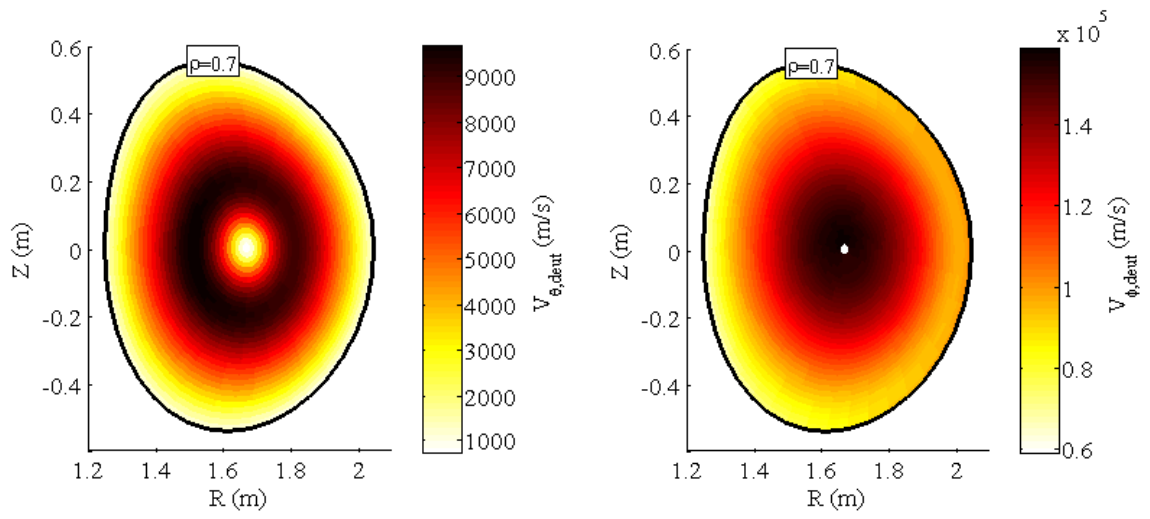


Figure 44: Poloidal (left) and toroidal (right) components of the Deuterium velocity vector

$$\vec{V} = V_r \hat{e}_r + V_\theta \hat{e}_\theta + V_\phi \hat{e}_\phi$$

REFERENCES

- [1] R. L. Miller, M. S. Chu, J. M. Greene, Y. R. Lin-Lin and R. E. Waltz, "Noncircular, finite aspect ratio, local equilibrium model," *Physics of Plasmas*, vol. 5, no. 973, pp. 973-978, 1998.
- [2] W. M. Stacey, R. W. Johnson and J. Mandrekas, "A neoclassical calculation of toroidal rotation profiles and comparison with DIII-D measurements," *Physics of Plasmas*, vol. 13, no. 062508, 2006.
- [3] C. Bae, W. M. Stacey and W. M. Solomon, "Extension of neoclassical rotation theory for tokamaks to realistically account for the geometry of magnetic flux surfaces," *Nuclear Fusion*, vol. 53, no. 043011, 2013.
- [4] W. Stacey, "Plasma Equilibria," in *Fusion Plasma Physics*, 1 ed., Weinheim, Germany, WILEY-VCH, 2005, pp. 103-128.
- [5] W. M. Stacey, "Fluid Theory," 1 ed., Weinheim, Germany, WILEY-VCH, 2005, pp. 85-98.
- [6] S. I. Braginskii, "Transport Processes in a Plasma," in *Reviews of Plasma Physics*, vol. 1, New York, Consultants Bureau, 1965, pp. 205-311.
- [7] W. M. Stacey, "Basic Physics," in *Fusion Plasma Physics*, Weinham, WILEY-VCH, 2005, pp. 1-15.
- [8] W. M. Stacey and D. J. Sigmar, "Viscous effects in a collisional tokamak plasma with strong rotation," *Physics of Fluids*, vol. 28, no. 9, 1985.
- [9] J. D. Callen, A. J. Cole and C. C. Hegna, "Toroidal flow and radial particle flux in tokamak plasmas," *Physics of Plasmas*, vol. 16, no. 082504, 2009.

- [10] W. M. Stacey, A. W. Bailey, D. J. Sigmar and K. C. Shaing, "Rotation and impurity transport in a tokamak plasma with directed neutral-beam injection," *Nuclear Fusion*, vol. 25, no. 4, pp. 463-477, 1985.
- [11] J. Candy, "A unified method for operator evaluation in local Grad-Shafranov plasma equilibrium," *Plasma Phys. Control. Fusion*, vol. 51, no. 105009, 2009.
- [12] J. P. Freidberg, *Ideal Magneto Hydro-Dynamics*, New York: Plenum Press, 1987.
- [13] L. L. Lao, H. S. John, R. D. Stambaugh, A. G. Kellman and W. Pfeiffer, "Reconstruction of current profile parameters and plasma shapes in tokamaks," *Nuclear Fusion*, vol. 25, no. 11, pp. 1611-1622, 1985.
- [14] W. M. Stacey, "Applications of the Miller equilibrium to extend tokamak computational models," *Physics of Plasmas*, vol. 15, no. 122505, 2008.
- [15] V. D. Shafranov, "Equilibrium of a Toroidal Pinch in a Magnetic Field," *Atomnaya Energiya*, vol. 13, no. 6, pp. 521-529, 1962.
- [16] W. M. Stacey and B. A. Grierson, "Interpretation of rotation and momentum transport in the DIII-D edge plasma and comparison with neoclassical theory," *Nuclear Fusion*, vol. 54, no. 073021, 2014.
- [17] L. W. Owen, J. M. Canik, R. J. Groebner, J. D. Callen, X. Bonnin and T. H. Osborne, "Comparing 1.5D ONETWO and 2D SOLPS analyses of inter-ELM H-mode plasma in DIII-D," *Nuclear Fusion*, vol. 50, no. 064017, 2010.
- [18] *MATLAB R2012a [software]*, Natick, MA: The MathWorks Inc., 2012.
- [19] *Mathematica, Version 10.2 [software]*, Champaign, IL: Wolfram Research, Inc., 2015.
- [20] *Python 2.7.8 [software]*, Python Software Foundation. Available at <http://www.python.org>, 2014.

- [21] *NAG Fortran Compiler, v. 6.0*, Oxford, UK: The Numerical Algorithms Group Ltd, 2015.
- [22] C. Bae, W. M. Stacey, S. G. Lee and L. Terzolo, "Predictions of the poloidal asymmetries and transport frequencies in KSTAR," *Physics of Plasmas*, vol. 21, no. 012504, 2014.
- [23] R. M. Churchill, "Impurity Asymmetries in the Pedestal Region of the Alcator C-Mod Tokamak [doctoral dissertation]," MIT Library Archives, Cambridge, 2014.